



Patrick Eckert

Advanced Silicon-Photomultiplier Characterization
for Calorimetric Applications

Diploma Thesis

HD-KIP-10-11

Faculty of Physics and Astronomy

University of Heidelberg

Diploma thesis

in Physics

submitted by

Patrick Eckert

born in Heidelberg

2010

Advanced Silicon-Photomultiplier Characterization for Calorimetric Applications

This diploma thesis has been carried out by Patrick Eckert at the
Kirchhoff Institute for Physics
under the supervision of
Prof. Dr. Hans-Christian Schultz-Coulon

Abstract

Silicon photomultipliers (SiPMs) are a novel type of semiconductor-based photodetectors suitable for a large variety of applications. In particular they are used for the readout of the scintillator tiles of a highly granular hadronic calorimeter prototype developed in preparation for the future *International Linear Collider* (ILC) experiment. Furthermore, SiPMs are a promising device for the *Positron Emission Tomography* (PET) imaging technique.

A test stand has been developed to study the characteristic properties of SiPMs and compare sensors from different manufacturers which is important in order to find the device best suited for future prototypes and the final detector design. In the context of this thesis the test stand was largely extended in order to allow a more complete characterization of the sensors. Besides the measurement of the breakdown voltage, gain, photon detection efficiency and dark-rate, the new setup allows to determine the cross-talk and after-pulse probability and the temperature dependence of different properties. The results of the individual measurements can be combined to determine the photon-counting resolution of the SiPM which is an important parameter for the calorimeter application. In addition, the spatial uniformity of the response can be studied by scanning the sensor with a small light spot. The measurement process and data analysis were fully automatized in order to achieve a simplified and faster characterization procedure which is essential for the characterization of a large number of devices.

Zusammenfassung

Silizium Photomultiplier (SiPMs) sind neuartige halbleiterbasierte Photodetektoren die für eine Vielzahl von Anwendungen geeignet sind. Insbesondere werden sie für die Auslese der Szintillator-Kacheln eines hoch granularen hadronischen Kalorimeter-Prototyps verwendet das im Rahmen der Vorbereitungen für den *International Linear Collider* (ILC) entwickelt wurde. Des Weiteren sind SiPMs sind vielversprechende Sensoren für das bildgebende Verfahren der *Positronen Emissions Tomographie* (PET).

Ein Testsystem wurde entwickelt um die charakteristischen Eigenschaften der SiPMs zu messen und Sensoren verschiedener Hersteller zu vergleichen. Dies ist wichtig um den am besten geeignetsten Sensor für zukünftige Prototypen und den endgültigen Detektorentwurf zu finden. In dieser Arbeit wurde das Testsystem wesentlich erweitert um eine umfassendere Charakterisierung der Sensoren zu ermöglichen. Neben der "Breakdown"-Spannung, Verstärkung, Photon-Detektions-Effizienz und Dunkelrate ermöglicht der neue Aufbau die "Cross-talk" und "After-pulse" Wahrscheinlichkeit und die Temperaturabhängigkeit verschiedener Parameter zu messen. Mit den Ergebnisse der einzelnen Messungen kann das Auflösungsvermögen bezüglich der Anzahl detektierter Photonen bestimmt werden was ein wichtiger Parameter der SiPMs für die Anwendung in Kalorimetern ist. Der Teststand ermöglicht ebenfalls den Sensor mit einem kleinen Lichtpunkt abzufahren und so die Stabilität des Ansprechverhaltens örtlich aufzulösen. Die Messungen und die Datenanalyse wurden vollständig automatisiert um eine einfachere und schnellere Charakterisierung zu ermöglichen. Dies ist grundlegend für die Charakterisierung einer großen Anzahl von Sensoren.

Contents

1	Introduction	1
1.1	The International Linear Collider	3
1.1.1	Calorimetry at the ILC	6
1.2	Positron Emission Tomography	9
2	Silicon Photomultipliers	13
2.1	Solid State Photodetectors	13
2.1.1	Photodiodes	15
2.1.2	Avalanche Photodiodes	18
2.2	The Silicon Photomultiplier	22
3	The SiPM Test Stand	31
3.1	Overview	32
3.2	Charge Spectrum	33
3.3	Dark Count Measurements	35
3.4	Temperature Measurements	37
3.5	Photo Detection Efficiency	39
3.6	Sensor Scans	42
4	SiPM Characterization	45
4.1	Gain Measurements	45
4.2	Dark-Rate Measurement	52
4.3	Crosstalk Measurements	53
4.4	After-pulse Measurement	58
4.5	Measurement of the Temperature Dependence	65
4.6	PDE Measurement	67
4.7	Uniformity Measurements	73
4.8	Photon-counting Resolution	76
5	Summary and Outlook	81

Chapter 1

Introduction

In the past decades experiments in the field of high energy physics offered new insights into the fundamental structure of the universe. The experimental results gave rise to the Standard Model (SM) of particle physics which describes the elementary particles and their fundamental interactions. This theory has been verified by experiments at the *Large Electron-Positron Collider* (LEP) and other particle accelerators with great accuracy.

The SM is a quantized gauge theory with the symmetry group $U(1) \times SU(2) \times SU(3)$. The quanta of the gauge fields mediate the interaction between the particles and for this reason are called force carriers or gauge bosons. There are twelve gauge bosons in the SM: the photon and the massive Z^0 , W^+ and W^- boson which mediate the electromagnetic and weak force and eight gluons which are the gauge bosons of the strong force.

Besides the gauge bosons which have an integer spin the SM includes 12 elementary particles of spin-1/2 (fermions) and their corresponding antiparticles which are the constituents of all matter known today. The quarks and leptons can be grouped into three particle generations according to their mass and can also be classified according to their interaction (see figure 1.1). There are six quarks (up, down, strange, charm, top, bottom) which can interact via the strong, electromagnetic and weak force and six leptons (electron, muon, tau and their corresponding neutrinos) which do not take part in the strong interaction. The neutrinos carry no electrical charge and therefore can only interact via the weak force, whereas the three charged leptons can also interact electromagnetically.

Gauge theories in general require massless gauge bosons which contradicts the experimental observations since the Z^0 and W^\pm are massive particles. This problem is solved by introducing the Higgs mechanism into the SM which requires a Higgs field with a non-zero vacuum expectation value. The interaction with this background field gives mass to the particles. The Higgs field also leads to the existence of a massive neutral Higgs boson. Although there is strong theoretical support for the Higgs mechanism, the Higgs boson was not observed yet. Previous experiments at the *Stanford Linear Collider* (SLC), Tevatron and LEP give a lower limit for the Higgs mass of $114 \text{ GeV}/c^2$ and an upper limit of $185 \text{ GeV}/c^2$ at 95% confidence level. Also the range from $160 \text{ GeV}/c^2$ to $170 \text{ GeV}/c^2$ was recently excluded by experiments at the Tevatron [1].

One of the main tasks of the *Large Hadron Collider* (LHC) at CERN¹ which successfully started operation recently is to find the Higgs particle. It will collide protons with a center-of-mass energy of up to 14 TeV which allows to produce particles in the energy range of the predicted Higgs mass. Although the Standard Model describes the experimental data with great precision, there are several phenomena that cannot be explained by this theory. Besides the search of the Higgs particle, the major objective of the LHC therefore is to search for physics beyond the Standard Model (e.g. supersymmetry).

¹Conseil Européen pour la Recherche Nucléaire

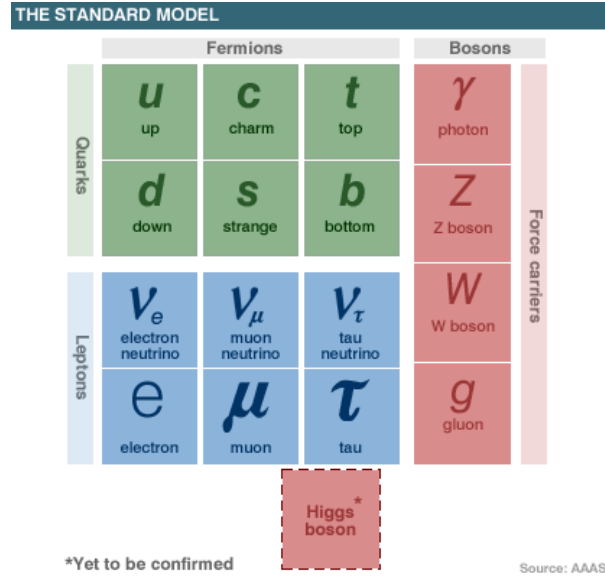


Figure 1.1: Standard Model of particle physics. The particles can be grouped into quarks, leptons and force carriers. The Higgs particle is yet to be discovered [2].

For many measurements at the LHC the achievable precision is limited due to the high QCD² background in the collisions of the strongly interacting protons. For precision measurements of the physics discovered at the LHC a lepton collider like the proposed *International Linear Collider* (ILC) is needed. The ILC is designed as a superconducting electron positron collider with a center-of-mass energy from 500 GeV up to 1000 GeV. The final scale for the center-of-mass energy will be set by the results and discoveries of the LHC. The physics which will be investigated at the ILC places challenging demands on the detector performance, e.g. an unprecedented jet energy resolution, tracker momentum resolution, and vertex impact parameter resolution has to be achieved [3]. The separation of W and Z bosons is crucial for many interesting physics processes at the ILC which appear in multi-jet final states. This requires a hadronic jet energy resolution of $\approx 30\%/\sqrt{E_{jet}}$ which is about a factor of two better than the resolution achieved at LEP. It appears to be possible to reach such jet energy resolutions with a highly granular calorimeter in combination with an excellent tracking system utilizing a new reconstruction method, the so-called *Particle Flow Approach* (PFA) [4]. In order to use this concept new developments in the field of calorimetry are needed. Different concepts for electromagnetic and hadronic calorimeters are developed and studied in the context of the CALICE³ collaboration. One of the proposed hadronic calorimeters is the *Analog Hadronic Calorimeter* (AHCAL) which is a sampling sandwich calorimeter consisting of alternating layers of steel absorber and plastic scintillator with fine transverse and longitudinal segmentation. A first prototype of this calorimeter has been built in order to study the applicability of this concept [5]. The active scintillator layers are segmented into small $3 \times 3 \times 0.5 \text{ cm}^3$ tiles which are read out by Silicon Photomultipliers (SiPMs) directly attached to them. SiPMs are a novel type of solid state photodetectors with exceptional properties like high gain, insensitivity to magnetic fields and compactness. This makes the SiPM a promising device not only for the

²Quantum Chromodynamics

³Calorimeter for the Linear Collider [3]

calorimeter read-out but for various fields of applications with the need of photosensors (e.g. Positron Emission Tomography).

In the context of this thesis methods for the characterization of the different properties of SiPMs have been developed. This is important for the comparison of sensors from different manufacturers allowing to find the device best suited for a particular application. Another important goal is to determine which parameters limit the photon-counting resolution and to find the optimal operation conditions for a device.

1.1 The International Linear Collider

The International Linear Collider (ILC) [3] is a proposed particle accelerator which will be able to make a more complete and precise experimental analysis of the Terascale physics compared to the LHC. The center-of-mass energy at the ILC is planned to range from 200 GeV to 500 GeV, upgradeable to 1 TeV. In addition, the operation at 91 GeV with reduced luminosity will be possible for calibration purposes. Unlike the LHC, the ILC will collide electrons and positrons. The main advantage of an e^+e^- collider is that the interacting leptons are elementary particles yielding a well defined initial state in contrast to compound particles like protons. The energy of the interacting particles is therefore known precisely and also the polarization of the beam can be prepared which allows for spin and parity measurements of the produced particles. The limiting factor for the center-of-mass energy of a circular e^+e^- collider is the energy loss due to synchrotron radiation which scales with $\propto E^4/(m_0 \cdot r^2)$ where r is the radius of the accelerator ring, E is the energy and m_0 is the mass of the particles. At the LHC this effect is negligible due to the large mass of the proton. However, for an e^+e^- collider with a center-of-mass energy of 500 GeV synchrotron losses would be enormous and therefore a linear accelerator structure is required. Figure 1.2 shows the schematic layout of the ILC for a center-of-mass energy of 500 GeV.

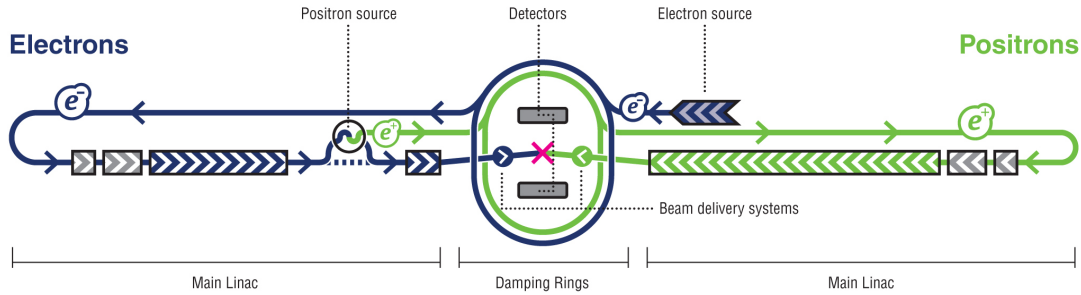


Figure 1.2: Schematic layout of the International Linear Collider. The total length is ≈ 31 km [3].

The electrons are produced by a photocathode DC gun and injected into the damping ring after being accelerated to 5 GeV. The positrons are produced by a helical undulator driven by the 150 GeV main electron beam. The electrons traversing the undulator generate high energetic photons which convert to e^+e^- pairs. The positrons are separated from the electrons and remaining photons and injected into the damping ring. In the damping rings the emittance of the electron and positron bunches is reduced before they are accelerated in the main linear accelerators (linac). The electrons and positrons are accelerated up to 250 GeV by 13 GHz superconducting radio frequency cavities with a gradient of 31.5 MV/m (see table 1.1). Finally a beam delivery system brings the two beams to collision with a crossing angle of 14 mrad. The

Parameter	Value	Unit
Center-of-mass energy	500	GeV
Peak luminosity	$2 \cdot 10^{34}$	$\text{cm}^{-2}\text{s}^{-1}$
Availability	70	%
Repetition rate	5	Hz
Duty cycle	0.5	%
<i>Main Linacs</i>		
Average accelerating gradient in cavity	31.5	MV/m
Length of each Main Linac	11	km
Beam pulse length	1	ms
Average beam current in pulse	9.0	mA
RMS horizontal beam size at interaction point	640	nm
RMS vertical beam size at interaction point	5.7	nm
<i>Damping rings</i>		
Beam energy	5	GeV
Circumference	6.7	km
Length of Beam Delivery section (2 beams)	4.5	km
Total site length	31	km
Total site power consumption	230	MW
Total installed power	≈ 300	MW

Table 1.1: Global Accelerator Parameters for a center-of-mass energy of 500 GeV [3].

interaction point is planned to be shared by two individual detectors operated by independent collaborations.

The ILC is planned to be operated with a pulse rate of 5 Hz. A pulse consists of 2635 bunches each containing $2 \cdot 10^{10}$ particles. The bunches have a spacial separation of 110 m which corresponds to a bunch interval of ≈ 370 ns at the interaction point [3]. The moderate overall number of bunch crossings due to the low pulse rate allows to read out all events without the need for a trigger in contrast to the experiments at the LHC.

Detector Concepts

The detectors at the ILC will need to achieve unprecedented precision to reach the performance required by the physics goals. At the moment three different concepts are studied utilizing different detector technologies:

- The International Large Detector (ILD) [6]
- The Silicon Detector (SiD) [7]
- Fourth Concept (“4th”) Detector [8]

where the ILD emerged from the prior LDC (Large Detector Concept) and GLD (Global Large Detector) concepts. The basic concept of the three detectors is similar. All have an inner vertex detector, a tracking system (Time Projection Chamber or silicon tracker), a calorimeter for energy measurements and an outer muon detector. In the following the ILD which is shown in figure 1.3 is discussed in detail.

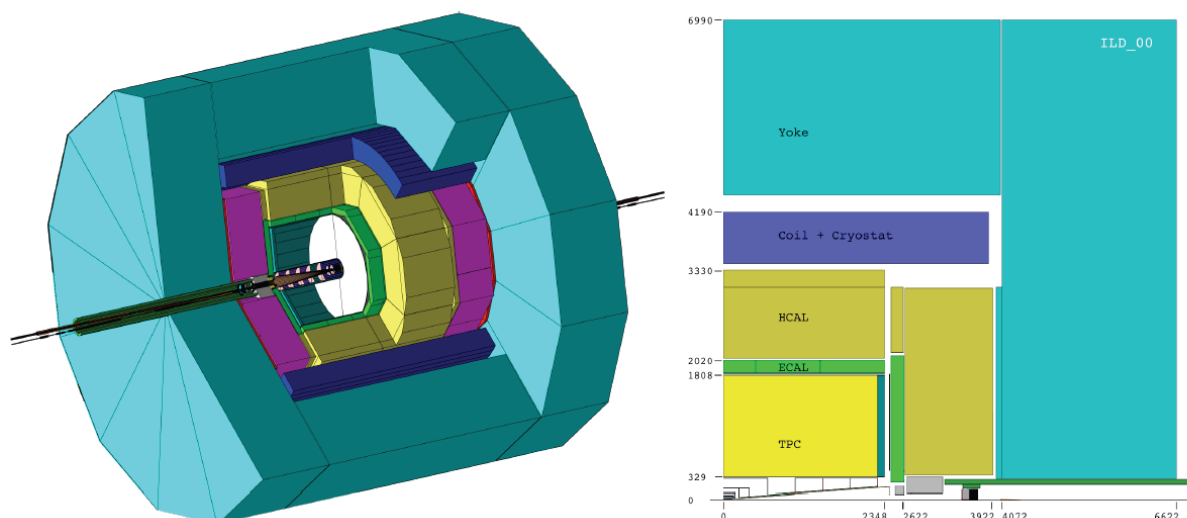


Figure 1.3: left: Schematics of the International Large Detector. right: Cut through the ILD; one quarter of the detector is shown [6].

The ILD concept is designed as a multi-purpose detector providing excellent precision in spatial and energy measurement. Combining the information of all subdetectors, particles can be identified and distinguished with high accuracy. Neutrinos and several particles predicted in supersymmetry theory cannot be measured directly in the detector due to their small interaction cross section, but can only be identified by missing energy. In order to measure missing energy with high precision the detectors at the ILC have to be as hermetic as possible. The tracking system of the ILD consists of an inner pixel vertex detector and the main tracker which is a combination of a Time Projection Chamber (TPC) and silicon trackers. The vertex detector plays an important role in the track reconstruction, especially for low momentum particles which don't reach the main tracker. The TPC measures three dimensional tracks of the traversing charged particles. The tracks are bend due to the magnetic field of $\approx 4\text{ T}$ generated by a superconducting coil which allows to determine the momentum of the particles. The tracking system is surrounded by the electromagnetic calorimeter (ECAL), which is optimized to measure the energy of electrons, positrons and photons, and the hadronic calorimeter (HCAL). Both are highly granular sampling calorimeters with tungsten as absorber material for the ECAL and steel for the HCAL. The small radiation length of tungsten ($X_0 = 3.5\text{ mm}$) allows for a compact design with a depth of roughly $24 X_0$ within 20 cm. Hadronic showers are not contained in the ECAL due to their much longer shower profile. Therefore the HCAL, which has a depth of 5.5 hadronic interaction lengths, is located right behind the ECAL. Both calorimeters are located inside the magnet coil in order to avoid dead material in front. The individual layers of scintillating material are segmented into small tiles with a size of $\approx 3 \times 3\text{ cm}^2$ which are individually read out with silicon photomultipliers. A small-sized photosensor like the SiPM is crucial for the calorimeter design in order to achieve the high granularity needed for the particle flow approach (see below). The outermost part of the detector is an instrumented iron return yoke which also serves as a muon detector. In addition to its muon tagging ability the system can be used as a tail catcher for hadronic showers leaking out of the calorimeter.

1.1.1 Calorimetry at the ILC

The ILC is designed to investigate the Higgs mechanism in detail and to search and study new physics at energies up to 1TeV. This places challenging demands on the detectors in terms of energy and tracking resolution. One of the most important parameters of the ILC detectors is the jet-energy resolution since many of the interesting physics channels appear in multi-jet final states. Hence, it is essential to separate hadronically decaying W and Z bosons which can be achieved with a jet-energy resolution of $\sigma_{E_{jet}}/E_{jet} = 30\%/\sqrt{E_{jet}}$ [3]. This is more than two times better compared to the best jet-energy resolution achieved at LEP. Figure 1.4 shows the separation of the W^\pm and Z^0 energy spectra for $\sigma_{E_{jet}} = 60\%\sqrt{E_{jet}}$ and $\sigma_{E_{jet}} = 30\%\sqrt{E_{jet}}$.

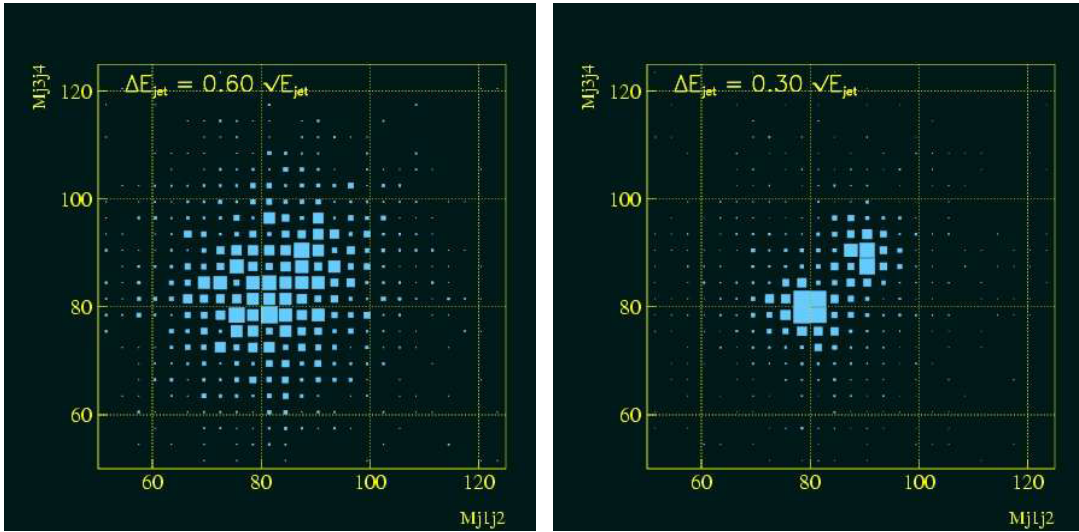


Figure 1.4: Separation of hadronically decaying WW/ZZ pairs for $\sigma_{E_{jet}} = 60\%\sqrt{E_{jet}}$ (left) and $\sigma_{E_{jet}} = 30\%\sqrt{E_{jet}}$ (right). The masses of the dijet pairs (in GeV) are denoted on the x and y axes. [9].

It can be seen that an energy resolution of $30\%\sqrt{E_{jet}}$ allows to clearly distinguish W and Z bosons. This excellent jet-energy resolution could be reached with the so-called particle flow concept which requires a highly granular calorimeter with very fine transverse and longitudinal segmentation and an excellent tracking system.

Particle Flow Concept

Considering an average jet, 65% of the jet-energy comes from charged particles, 26% from photons and about 9% from neutrons and neutral hadrons. The momentum measurement of the charged particles with the tracking system is usually much more precise than the energy measurement. Only for very high energies calorimeters yield a better resolution than particle trackers. The *Particle Flow Approach* (PFA) is to reconstruct charged particles in the tracker while the calorimetric system is dedicated to measure only neutral particles. The energy of the charged particles can be determined from the momentum measurement in combination with the particle ID. The PFA requires to disentangle the contribution from neutral and charged particles in the calorimeter to avoid double counting. Hence, the particles in a jet have to be reconstructed individually, i.e. the energy deposition of the individual particles has to be resolved. This can be challenging if the particle showers are too close to each other since parts

of a shower can be allocated to the wrong particle degrading the energy resolution. To minimize this confusion a highly granular calorimeter (“imaging calorimeter”) and very efficient clustering algorithms are required. In this case the particle flow concept can significantly improve the jet-energy resolution. Figure 1.5 shows the particle reconstruction in a simulated jet using a particle flow algorithm. Individual tracks are visible in the calorimeter and hence can be assigned to charged particles in the shower.

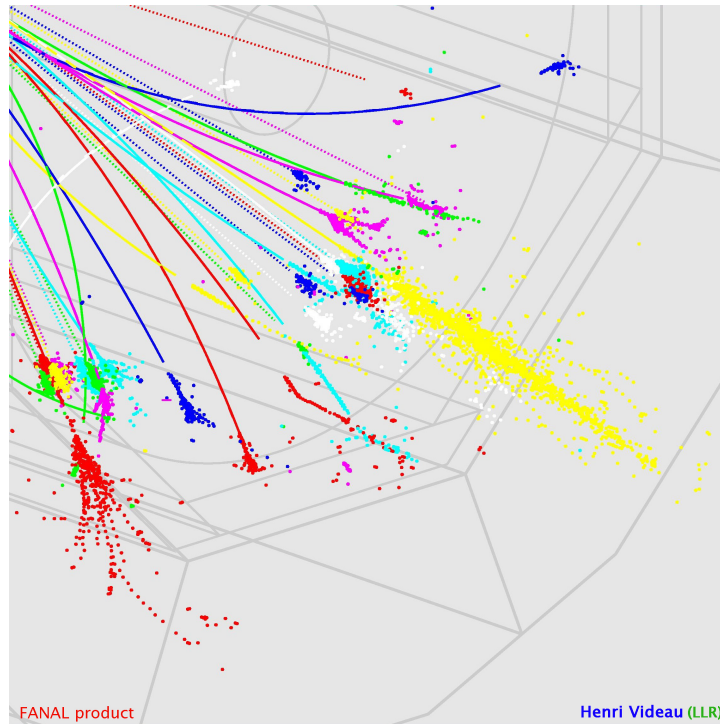


Figure 1.5: Simulated jet in an imaging calorimeter. The particles are reconstructed using a particle flow algorithm [10].

The Calorimeter Prototype

The CALICE (Calorimeter for the Linear Collider) collaboration studies several different calorimeter designs and technologies. Two different concepts for a hadronic calorimeter are proposed: a digital (DHCAL) and an analog calorimeter (AHCAL). The DHCAL is segmented into small cells with a size of $1 \times 1 \text{ cm}^2$ which provide only digital information, i.e. if a particle traversed a cell or not. The energy is reconstructed from information provided by the particle shower such as cell multiplicity and shower width. The AHCAL is a more classical approach with a bigger cell size compared to the DHCAL and information about the energy deposited in the calorimeter cell. In both cases the high granularity allows for particle flow analysis which is the key to achieve the desired jet-energy resolution.

A prototype of the analog hadronic calorimeter has been built at DESY to study the concept and physics performance of such a calorimeter. It consists of 38 alternating layers of steel absorber plates with a thickness of 1.6 cm and scintillator tiles with a thickness of 0.5 cm. This corresponds to a nuclear interaction length of $4.5 \lambda_{\text{int}}$. The size of the tiles range from $3 \times 3 \text{ cm}^2$ in the center to $12 \times 12 \text{ cm}^2$ at the outer part. This allows to study the performance of the PFA

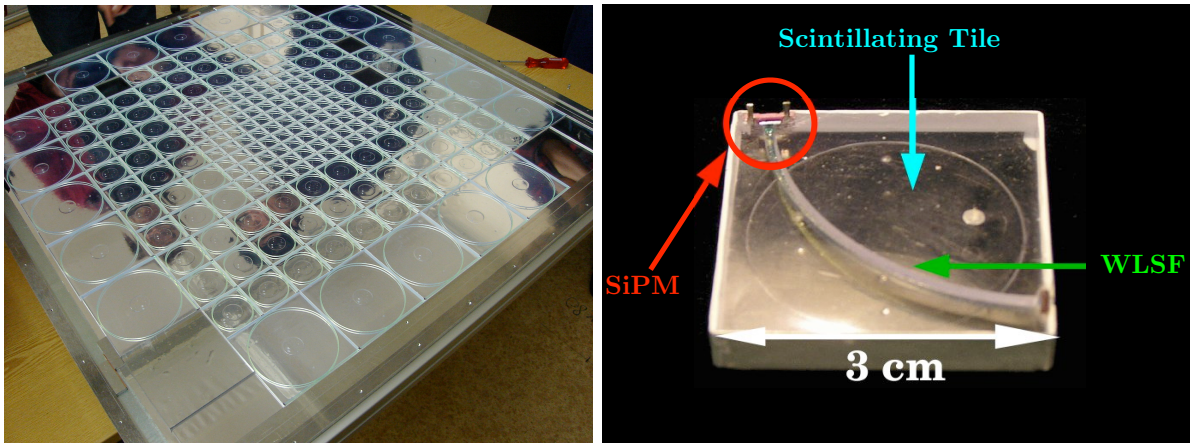


Figure 1.6: left: One layer of scintillating tiles of the analog HCAL prototype. The size of the tiles varies from $3 \times 3 \text{ cm}^2$ in the center to $12 \times 12 \text{ cm}^2$ at the border. **right:** Scintillating tile ($3 \times 3 \text{ cm}^2$) with wavelength-shifting fibre and attached SiPM for the light readout [11].

depending on the tile size. Figure 1.6 (left) shows a photograph of one layer of scintillating tiles. A particle traversing a scintillator tile produces a certain amount of blue scintillation light depending on the energy loss in the tile. The sides of each tile are matted in order to provide diffuse reflection and suppress optical cross-talk between neighboring tiles. The top and bottom sides are covered with a highly reflective foil to minimize the loss of scintillation light. A wavelength-shifting fibre (WLSF) with a diameter of 1 mm is inserted into a 2 mm deep groove on the tile in order to collect the scintillation light. It converts the blue scintillation light into green light and guides it to a silicon photomultiplier coupled to one end of the fibre. The other end of the fibre is covered with a mirror to increase the light yield. The WLSF is necessary since the used SiPM is not sensitive to the blue scintillation light. It also improves the spatial homogeneity in the response of the tile since the amount of light guided to the SiPM by the WLSF has only a small dependence on the position of the particle passage.

Silicon photomultipliers are well suited for the tile readout due to the high gain, good photon detection efficiency and insensitivity to magnetic fields. The latter is especially important for the final design since the calorimeter will be located inside the strong magnetic field of the coil. Furthermore SiPMs are very small in size allowing to attach them directly to the tiles which is essential in order to achieve a high granularity. Also the low operation voltage ($< 100 \text{ V}$) and the small power consumption ($\approx 50 \mu\text{W}$) are important features for the design of a system with a large number of SiPMs. The SiPMs used in the AHCAL prototype are developed by the Moscow Engineering Physics Institute (MEPhI). Nowadays there are several manufacturers producing similar sensors. One device tested as a possible candidate for future prototypes is the so-called *Multi-Pixel Photon Counter* (MPPC) from the company HAMAMATSU. This device shows a better optical sensitivity in the blue spectral region, making it possible to read out the scintillation light without a WLSF [12]. This would reduce the production costs and simplify the SiPM positioning since the sensor would not have to be carefully coupled to the fibre.

The growing variety of available sensors requires the possibility to characterize the devices in order to find the sensor best suited for the calorimeter readout. For this reason a test stand has been developed [13]. Besides a high dynamic range, the calorimetric application requires a good photon-counting resolution which is influenced by the photon detection efficiency and other

effects introducing noise. In this thesis the test stand has been advanced in order to determine the different contributions limiting the photon-counting resolution. The data acquisition and analysis has been fully automatized in order to enable the characterization of a large number of sensors in a short time.

1.2 Positron Emission Tomography

The applications for silicon photomultipliers are not limited to the field of high energy physics. The SiPM is also a promising device for *Positron Emission Tomography* (PET) detectors. Positron emission tomography is a nuclear medicine imaging technique which is used for the monitoring of active regions in organisms. It produces a three-dimensional image of the patient indicating regions of high metabolism which makes PET a powerful tool in modern clinical diagnostics. The working principle is as follows: A positron-emitting radionuclide (radiotracer) incorporated in a biologically active molecule (e.g. glucose or another substance involved in the metabolism) is injected into the patient. In the case of glucose the radiotracer will concentrate in regions with increased metabolic activity (e.g. cancer cells). The emitted positrons annihilate with electrons of the surrounding tissue generating two 511 keV back to back photons. These photons are detected by photodetectors coupled to scintillating crystals arranged in a ring-like geometry (see figure 1.7). The scintillating crystals convert the gamma rays into visible light which can be detected by photodetectors like Photomultiplier Tubes (PMTs) or Avalanche Photodiodes (APDs). If two 511 keV photons are detected within a coincidence window of typically ≈ 2 ns, it can be assumed that their source is located along the line joining the two detector elements which is referred to as *Line of Response* (LOR). A reconstruction algorithm uses the information provided by the LORs to produce an image of the radiotracer concentration.

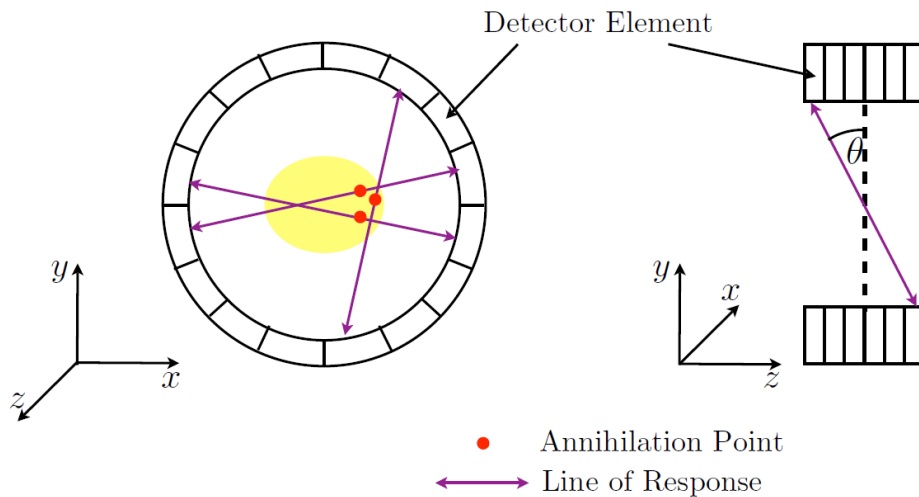


Figure 1.7: Schematics of a PET detector. The region where many lines of response cross indicates a region of increased metabolism [13].

The spatial resolution of a PET detector (typically 4 – 6 mm) is intrinsically limited by the positron range and the momentum of the annihilating electron and positron which causes a non-collinearity of the annihilation photons. Another limiting factor is the performance of

the gamma detectors. Besides a high granularity, a good energy and timing resolution is required in order to reduce background events. An annihilation photon can be diverted from its original track due to Compton scattering losing a fraction of its initial energy. In this case the LOR does not indicate the origin of the annihilation. However, this "scattered coincidences" can be discriminated by measuring the energy and only selecting the 511 keV photons. This requires good energy resolution in order to separate the Compton events from the photopeak. Another source of background noise are random coincidences which can occur if one of the two annihilation photons is absorbed in the patient's tissue. In this case only single photons will be detected which therefore are referred to as "singles". The random coincidence rate R for a given LOR joining the detector elements i and j is described by:

$$R = 2\tau R_i R_j$$

where τ is the coincidence time interval and $R_{i,j}$ is the single rate for the detector element i and j respectively. The random coincidences can be reduced with a smaller coincidence window which requires a good time resolution. An excellent time resolution is also required for the so-called *Time-of-Flight* (TOF) PET. Unlike in conventional PET, in time-of-flight PET the time interval between the two annihilation photons is measured which allows the determination of the position of the annihilation along the LOR (see figure 1.8). With a typical timing resolution of 500 ps a spatial resolution of ≈ 7 cm can be achieved. This is no match to the spatial resolution of ≈ 5 mm which can be achieved with conventional methods. However, the TOF information can be used to reduce the noise [14] and therefore improve the sensitivity of the detector. This allows to minimize the radiotracer concentration without degrading image quality.

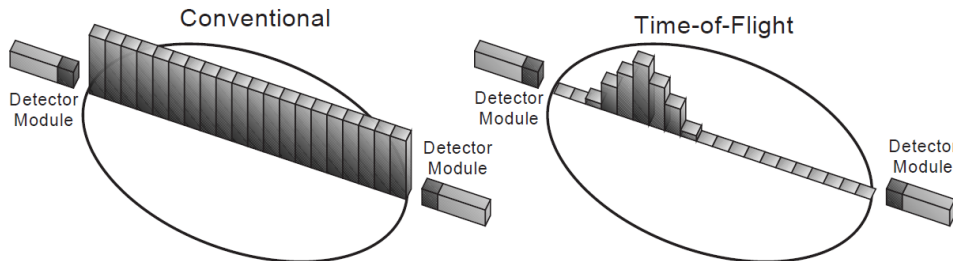


Figure 1.8: Time-of-Flight Reconstruction. With conventional reconstruction, every point on the LOR is incremented by the same probability. With time-of-flight reconstruction, each point is incremented by the probability that the source is located at that position, as determined by the time-of-flight measurement [14].

Most of today's PET detectors use PMTs for the detection of the scintillation light. A drawback of PMTs is the bulky shape which limits the granularity and thus the spatial resolution of the detector. Furthermore PMTs cannot be operated in magnetic fields which prohibits a combination with *Magnetic Resonance Imaging* (MRI) tomography. There are also concepts to use APDs for the scintillator readout since they are compact devices and insensitive to magnetic fields. However, this requires sophisticated readout electronics due to the relatively small gain of the APD. The silicon photomultiplier is a promising device for future PET systems since it provides a high gain and sensitivity comparable to a PMT, and is compact and insensitive to magnetic fields like an APD. In addition TOF PET benefits from the good timing resolution of the SiPM.

A PET prototype was built in the KIP⁴ workshop to study the performance of a PET detector using SiPM readout with the goal to reach a timing resolution of less than 300 ps. The prototype consists of two detector arms each with a matrix of 4×4 SiPMs attached to $3 \times 3 \times 15 \text{ mm}^3$ LSO crystals (see figure 1.9). The angle between the two arms is adjustable in the range from 70° to -70° . The distance of the matrices to the center can be adjusted for each arm individually. A motor is used to rotate the prototype in order to simulate a full 360° detector. The characterization and study of the SiPMs is an important step to achieve the desired performance of the prototype.

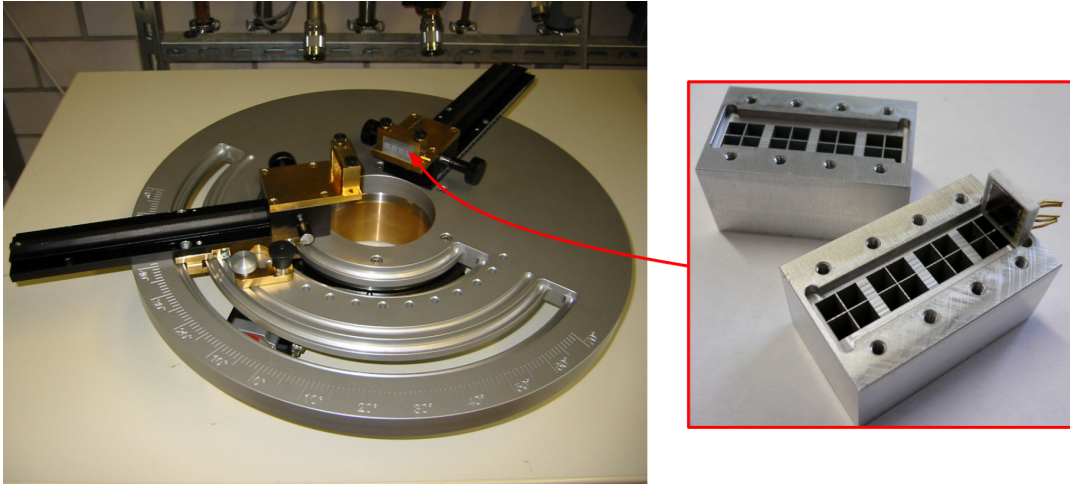


Figure 1.9: Left: Picture of the PET prototype. A positron emitting source can be placed in the center of the detector. The angle between the detector arms can be adjusted and the whole device can be rotated in order to simulate a full 360° detector. **Right:** Picture of the mounting for the scintillating crystals and SiPM matrices each mounting consists of 4×4 cells. One 2×2 channel SiPM array is shown.

⁴Kirchhoff-Institute for Physics

Chapter 2

Silicon Photomultipliers

There are many different types of radiation detectors due to the special requirements that arise with a certain field of application. A novel type of solid state photodetector is the *Silicon Photomultiplier* (SiPM)¹ or *Multi Pixel Geiger Mode Avalanche Photodiode* (MPGAPD) which is a promising device for a large variety of applications. The following chapter gives an overview of the basic concepts of solid state photodetectors. In the first section the fundamentals of semiconductors and their application to basic photodetectors like the *Photodiode* and the *Avalanche Photodiode* (APD) are presented and in section 2.2 the concept of the SiPM is discussed in detail.

2.1 Solid State Photodetectors

Solid state photodetectors are based on semiconducting materials. Compared to isolators, semiconductors have only a small energy gap between the conduction band and the valence band of typically 1 – 2 eV (e.g. 0.66 eV for germanium and 1.22 eV for silicon). For very low temperatures there are no free charge carriers since the electrons are in the ground state and bound in the valence band. For higher temperatures the thermal energy exceeds the band gap energy and electrons can be excited into the conduction band. This results in an unoccupied state in the valence band referred to as “hole”, which, like the electron in the conduction band, is a free charge carrier. The occupation probability of the energy states is described by the Fermi-Dirac distribution [15]:

$$F(E) = \frac{1}{\exp\left(\frac{E-E_F}{kT}\right) + 1}$$

where E_F is the Fermi energy, k is Boltzmann’s constant and T is the absolute temperature. The density of states is given by:

$$N(E) = 4\pi\left(\frac{2m}{h^2}\right)^{\frac{3}{2}}\sqrt{E}$$

where m is the effective mass and h is Plank’s constant. The density of free electrons can be calculated by a convolution integral of the occupation probability and the density of states above the lower edge of the conduction band:

$$n = \int_{E_{cond. band}} F(E) N(E) dE = N_C e^{-\frac{E_C-E_F}{kT}}$$

¹There are many different names for similar devices, e.g. Multi Pixel Photon Counter (MPPC) from HAMAMATSU, Silicon Photomultiplier (SPM) from SensL, Multi-pixel Avalanche Photodiode (MAPD) from Voxel, Solid State Photomultiplier (SSPM) from Photonique. In this thesis the abbreviation SiPM is used as a general name whenever the producing company is not emphasized explicitly.

where E_C is the lowest energy of the conduction band. The density of holes in the valence band can be determined similarly:

$$p = N_V e^{-\frac{E_F - E_V}{kT}}$$

where E_V is the upper energy of the valence band. N_C and N_V represent effective densities of states for the conduction and valence band respectively and depend on the effective mass and temperature.

Intrinsic Semiconductors

Semiconductors with high purity are called “intrinsic”. For intrinsic material, free charge carriers can be created by thermal or optical excitation, or ionization by charged particles. A photon with sufficient energy can excite an electron from the valence band via photoelectric absorption or Compton scattering and lift it into the conduction band. Since for every excited electron a hole remains in the valence band the number density of electrons in the conduction band n_i and holes in the valence band p_i is the same. If the photon energy is larger than the gap energy, the excited electron will subsequently lose energy by non-radiative lattice interactions (intraband transitions) until it reaches the lower edge of the conduction band. After a finite time the electron recombines under emission of photons. The recombination process and therefore the lifetime of the excited electron depends on the specific type (see figure 2.1) and size of the energy gap.

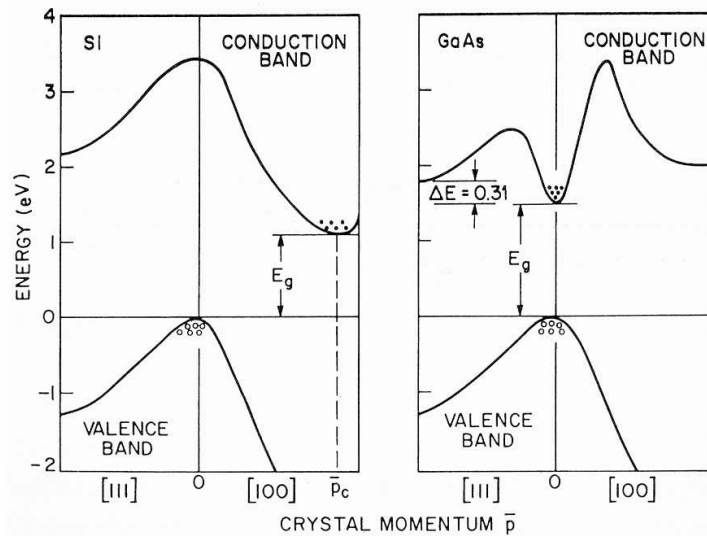


Figure 2.1: Energy bands of a semiconductor with an indirect (left) and direct (right) band gap. The x-axis represents the momentum in a direction of the crystal described by the Miller indices [15].

In some materials recombination can occur without changing the momentum of the electron (direct band gap). In other materials (e.g. silicon) the holes in the valence band have a different momentum than the electrons in the conduction band (indirect band gap). In this case the recombination must also involve the emission or absorption of a phonon in order to fulfill momentum conservation. The involvement of the phonon makes this process much less likely to occur than the direct transition in the case of a direct band gap. In indirect band gap materials recombination is favored to happen at impurities in the silicon crystal which introduce

intermediate energy states between the valence and conduction band. These intermediate states can also be occupied by electrons with an energy lower than the band gap.

Doped Semiconductors

In the production of the semiconductor crystal a small level of impurities is unavoidable. Impurities can also be implanted on purpose in a process called “doping” in order to achieve certain properties of the semiconducting material. When an atom with five possible covalent bonds (e.g. arsenic) is added to a lattice of atoms with four bonds (e.g. silicon), the fifth electron is only weakly bound and can easily be excited into the conduction band. In other words, these so-called “donator” atoms introduce an energy state close to the conduction band (see figure 2.2). Such a material is referred to as n-doped. Substituting a silicon atom by a trivalent atom (e.g. boron) energy states close to the valence band are produced. One of the four covalent bonds is only occupied by one electron instead of two. These “acceptor” states can trap an electron which generates a free hole. This is called p-type doping.

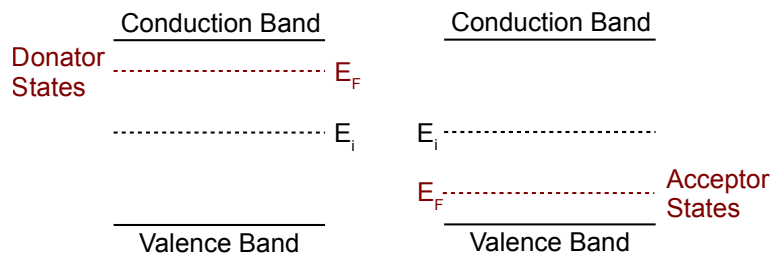


Figure 2.2: Schematic view of the energy bands of doped semiconductors. In n-doped material the energy gap between the donor states and the conduction band is small (≈ 0.05 eV). At room temperature the thermal energy of the electrons exceeds this gap energy and the donor states will therefore be completely depopulated yielding free electrons in the conduction band. In p-doped material electrons from the valence band can easily be excited to the acceptor states leaving free holes in the valence band.

If the density of electrons in the conduction band is increased by n-doping, the hole density in the valence band is significantly reduced due to recombination. The conductivity of a doped semiconductor is therefore determined by the carriers introduced by the doping.

2.1.1 Photodiodes

The photodiode is the most basic solid state photodetector. It is based on a junction of p-doped and n-doped material. At the boundary there is a strong gradient of the charge carrier concentration which causes the electrons to diffuse to the p-side and holes to the n-side where they recombine. As a consequence, a layer with almost no free charge carriers called “depletion region” is formed at the interface (see figure 2.3a). The remaining space charge from the doped atoms generates an electric field which forces a current opposite to the diffusion current. An equilibrium is reached when the two currents compensate.

If an electron-hole pair is produced by photon absorption in the depletion region the electric field from the space charge causes the electron and the hole to rapidly drift towards the cathode and anode, respectively (see figure 2.3b). As a consequence, a current proportional to the photon

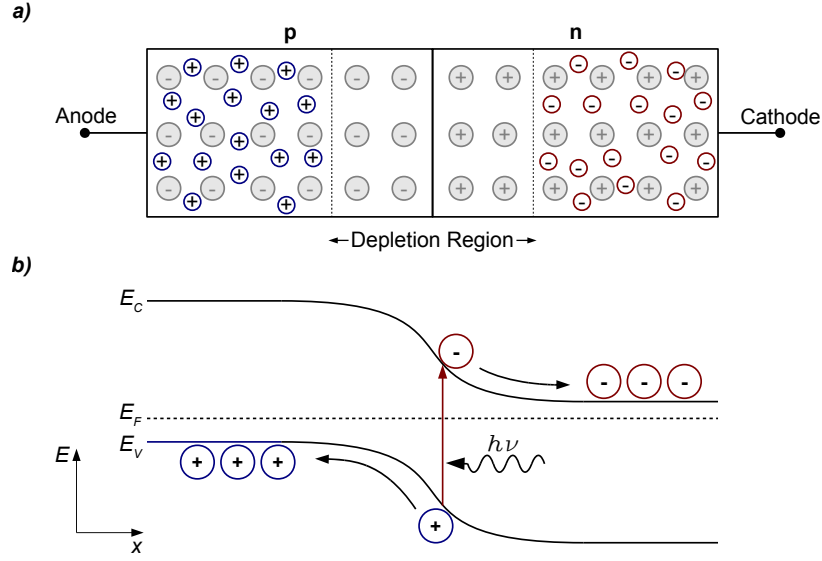


Figure 2.3: *a)* Schematic view of a p-n-junction. Electrons (red) near the interface can diffuse from the n region to the p region and recombine with holes (blue) and vice versa. This process generates a depletion region around the interface with no free charge carriers. The remaining space charge generates an electric field which opposes the diffusion process. *b)* Band structure of the p-n-junction. Electron-hole pairs can be produced by photon absorption. Charge carriers produced in the depletion region will drift to the n- and p-side respectively. Considering an incident photon flux this process will generate an photocurrent.

flux is generated. In addition to this photocurrent a small dark current is generated by diffusion processes.

Electron-hole pairs which are generated outside the depletion region are much more likely to recombine before one constituent can reach the high field region which reduces the efficiency to detect them. The depletion width can be increased by applying a reverse bias voltage $V_{bias} < 0$ to the p-n diode which is described by the following equation [15]:

$$d = \sqrt{\frac{2\epsilon\epsilon_0(N_A + N_D)}{q_e N_A N_D} (V_{bi} - V_{bias})}$$

where q_e is the elementary charge and ϵ and ϵ_0 are the permittivity and vacuum permittivity. The electric field caused by the different doping concentrations N_A and N_D in the p- and n-layer generates the so-called “built in voltage” V_{bi} . A large depletion width not only increases the photon detection efficiency but also reduces the capacitance of the sensor:

$$C_D = \frac{\epsilon\epsilon_0 A}{d} \quad (2.1)$$

A small capacitance results in a fast response of the sensor. The response speed is determined by the cutoff frequency which is defined as the frequency at which the output for a sine-modulated light signal decreases by 3 dB compared to the output at 100 kHz [16, 17]. It can be described according to the following equation:

$$f_c = \frac{1}{2\pi \cdot C_D \cdot R_L} \quad (2.2)$$

where R_L is the load resistance. However, if the depletion width gets too large, the signal speed is limited by the transit time of the charge carriers in the depletion region.

The depletion region can increase until it reaches the back of the semiconductor material which is the case at the so-called “reach-through” voltage. The width of the depletion region also determines the spectral sensitivity of a photodiode since the absorption depth of photons depend on their wavelength. The probability that the fraction dn of n photons of wavelength λ are absorbed after traveling a distance dx in the material can be assumed constant throughout the material. Therefore the number of photons at a depth x is described by the following equation:

$$n(x) = n_0 \cdot (1 - R) \cdot e^{-\mu(\lambda)x} \quad (2.3)$$

where n_0 is the initial number of photons and $\mu(\lambda)$ is the absorption coefficient and R describes the reflection probability on the surface. In order to reduce reflection loss most photo-sensors are coated with an isolator with a refractive index smaller than the refractive index of the semiconductor material. This intermediate layer increases the transmission probability of the incident light. The isolator also protects the photodiode from diffusion of impurities into the depletion layer which would increase the dark current of the sensor.

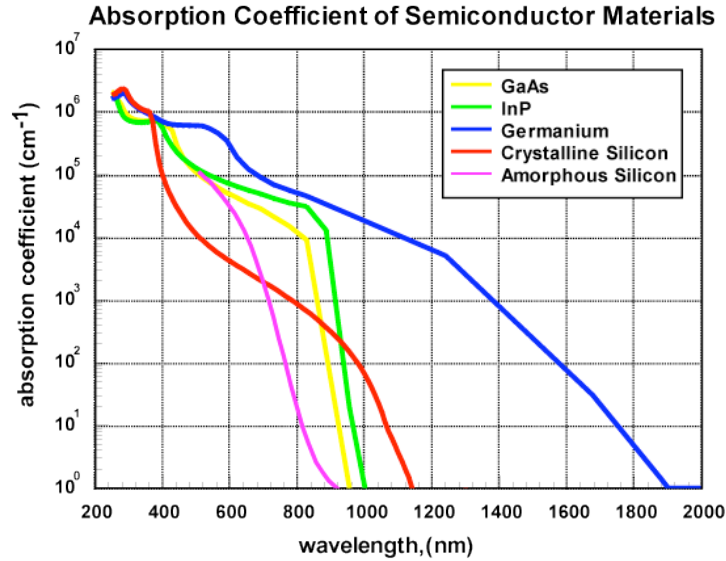


Figure 2.4: Optical absorption coefficients μ for different semiconductor materials as a function of the wavelength [18].

Figure 2.4 shows the absorption coefficient for different semiconductors as a function of the wavelength. The absorption length for silicon varies from 10 nm for ultraviolet light to 0.1 mm for infrared light. In order to achieve a good detection efficiency for blue and ultraviolet light the photons should not have to travel more than one absorption length before reaching the depletion layer. For the detection of short wavelength photons the covering layers therefore have to be very thin. On the other hand a high efficiency in the infrared spectral region requires the depletion width to be at least of the order of one absorption length.

PIN-Photodiodes

By adding an intrinsic layer between the p- and n-layer the detection efficiency can be increased especially for longer wavelengths. Such a device is called PIN-Photodiode. Often the intrinsic layer is produced by bringing a p-type semiconductor in contact with a lithium bath. The lithium ions diffuse into the semiconductor and by applying an external electric field the ions can drift far into the crystal and compensate the acceptor ions locally. With this method a layer of several millimeters with intrinsic conductivity can be produced.

If a moderate reverse bias voltage is applied to the sensor the depletion region extends over the complete intrinsic layer. Besides the higher efficiency also the diode capacitance is reduced which results in a higher signal speed (see equation 2.2). Since the width of the depletion layer is basically determined by the width of the intrinsic layer the detection efficiency is stable under fluctuations of the bias voltage once the intrinsic layer is depleted completely. Since PIN- and pn-photodiodes have no intrinsic charge amplification the response of these detectors is also stable under temperature fluctuations. For this reasons they are excellent devices for monitoring and calibration purposes. However, photodiodes cannot be used to detect single photons due to the missing gain.

2.1.2 Avalanche Photodiodes

Avalanche Photodiodes (APDs) have a similar structure to photodiodes since they basically consist of a p-n-junction (see figure 2.5). Besides the slightly different doping profile, the main

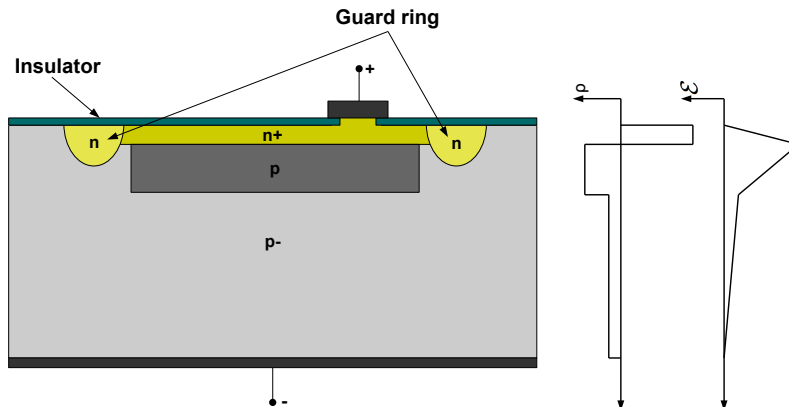


Figure 2.5: Schematic view of an avalanche photodiode with an n-on-p doping structure. The distribution of the space charge density ρ and the resulting electrical field \mathcal{E} are shown on the right.

difference compared to photodiodes is that the APD is operated at a high reverse bias voltage of typically 10^2 V to 10^3 V. This results in a large depletion region and a high electric field at the n^+ -p junction (n^+ refers to highly n-doped material). In this so-called “multiplication region” electrons and holes can produce secondary electron-hole pairs by a process called impact ionization. Due to the high electric field the charge carriers can gain enough energy between two collisions to create an electron-hole pair which results in an avalanche process also referred to as “avalanche breakdown”. In order to avoid local avalanche breakdown the electric field in the multiplication region has to be homogeneous and in particular the leakage field at the n^+ -p $^-$ junction (p $^-$ refers to slightly p-doped material) should be as small as possible. This is

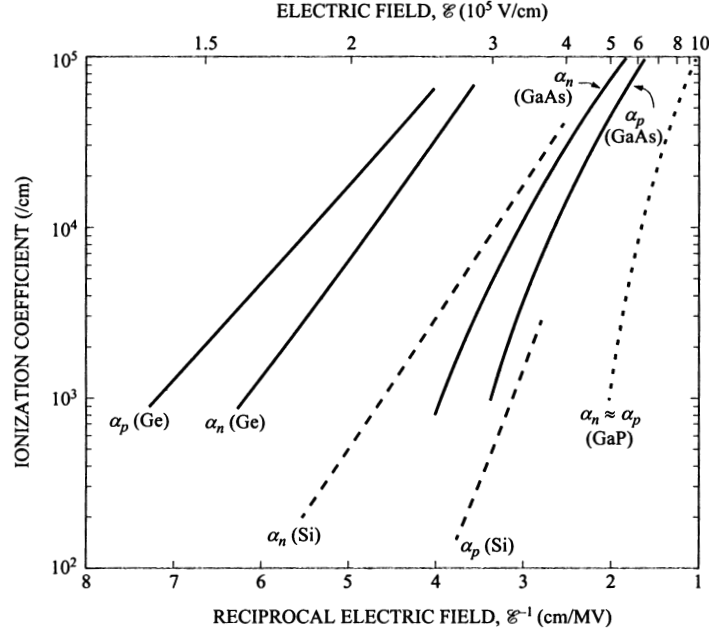


Figure 2.6: Impact ionization coefficient α for electrons and holes for different semiconductors as a function of the electrical field [19]

achieved with a n-doped guard-ring around the n^+ layer which reduces the doping gradient at the edges.

The impact ionization coefficient α which is given in units of inverse length describes the number of secondary charge carriers produced by a electron or hole while traveling one unit length. Figure 2.6 shows the impact ionization coefficient for several semiconductors as a function of the electric field. This parameter is in general different for electrons and holes resulting in two different operation modes depending on the applied reverse bias voltage which determines the electrical field in the multiplication region.

Linear Mode

In case of silicon, electrons dominate the charge multiplication process for moderate bias voltages due to the larger impact ionization coefficient. If an electron-hole pair is produced in the p-doped region the electron drifts towards the cathode (positive polarity). In the high field region around the n^+ -p junction the electron gains enough energy to create secondary electron-hole pairs and thus trigger an electron avalanche. In this way a charge multiplication factor of $10^2 - 10^3$ can be reached. The produced holes drift to the anode (negative polarity) without causing further ionization in the multiplication region because of the small impact ionization coefficient. The avalanche consequently propagates only in the direction of the electrons and the charge amplification ends once all electrons have left the multiplication region. The avalanche multiplication process is illustrated in figure 2.7. This mode of operation is called "linear mode" since the measured current is proportional to the number of incident photons:

$$I_{APD} = G \cdot I_{\gamma}$$

where I_{γ} is the incident photon current and G is the gain of the device.

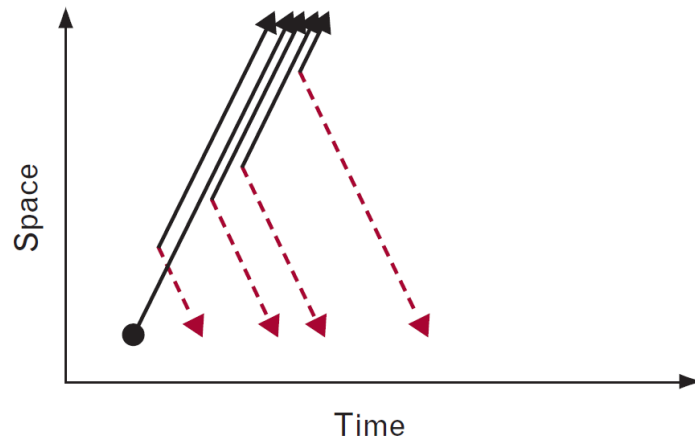


Figure 2.7: Avalanche multiplication process for the linear operation mode illustrated in a space time diagram. A primary electron (black) can create secondary electron-hole pairs in the multiplication layer. For moderate bias voltages the ionization coefficient for holes (red) is too low to produce further electron-hole pairs. Hence, the avalanche only propagates in one direction and is limited by the length of the high field region [20].

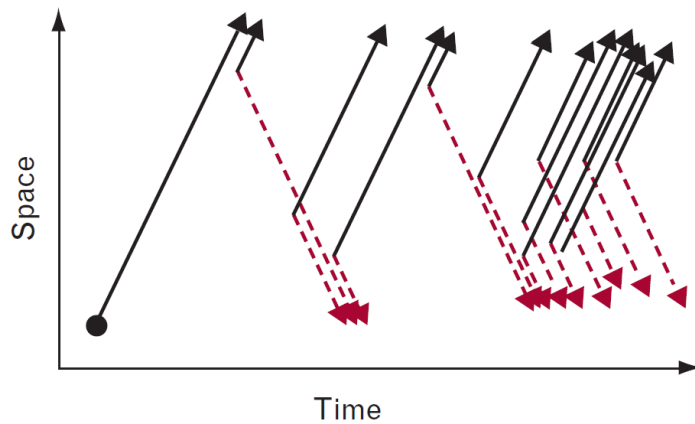


Figure 2.8: Avalanche process for Geiger mode operation. If the bias voltage exceeds the breakdown voltage both electrons and holes contribute to the avalanche process. In this case the avalanche extends to the whole high field region, leading to an exponentially growing current which has to be quenched [20].

If an electron-hole pair is created in the n^+ -layer only a small avalanche can develop due to the low impact ionization of the holes. The APD type shown in figure 2.5 (n-on-p doping structure) therefore is most sensitive to photons which have a large enough absorption length to reach the p-layer (red and green light). If the doping profile is inverted (p-on-n doping structure) the APD is mainly sensitive to blue light.

Geiger Mode

The second possible operation mode is realized if the bias voltage exceeds the so-called “breakdown voltage” V_{break} . In this case the electric field is high enough that also holes contribute to the charge multiplication. If an avalanche is triggered it propagates in both directions and extends to the whole high field region since also holes can create secondary electron-hole pairs. This so-called “Geiger breakdown” of the APD is illustrated in figure 2.8. In this mode of operation the avalanche breakdown yields a growing current I through the device which will cause a voltage drop at the p-n-junction due to the internal resistance R_{int} of the sensor which is caused by the resistance of the metal-silicon contacts and metal leads:

$$V_{junction} = V_{bias} - R_{int} \cdot I$$

where V_{bias} is the applied reverse bias voltage. The decreasing voltage $V_{junction}$ has a negative feedback on the breakdown current. This feedback mechanism compensates fluctuations in the breakdown current and results in a finite steady state. During the avalanche breakdown the APD is not sensitive to subsequent photons. Therefore a mechanism has to be implemented to stop the avalanche process which is referred to as “quenching”. There are two common quenching techniques. In the case of “active quenching” an analog circuit is used to actively shut down the bias voltage if an avalanche breakdown is detected by measuring a rising current. Another convenient way to quench the breakdown is to connect a sufficiently large quenching resistor $R_q \approx 10^5 - 10^7 \Omega \gg R_{int}$ in series with the p-n-junction (see figure 2.9) which is referred to as “passive quenching”. If no photon is detected there is no current flowing and the full bias

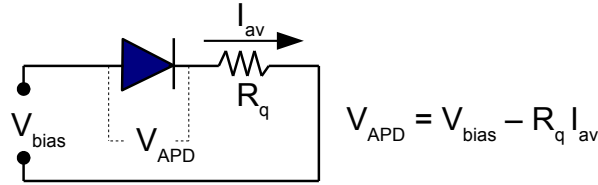


Figure 2.9: Passive quenching circuit diagram. In case of an avalanche breakdown the generated current flowing through the quenching resistance causes the voltage at the APD to drop below the breakdown voltage.

voltage ($V_{bias} > V_{break}$) is applied to the APD. During an avalanche breakdown the APD capacitance C_D discharges and the current I_{av} flowing through the quenching resistor causes the voltage at the APD to drop below the breakdown voltage which stops the avalanche process. After the discharge the diode is slowly recharged with the time scale $R_q C_D$. This recovery time limits the dynamic range of a Geiger-mode APD since photons reaching the sensor during this time will not be detected. The operation of the device above the breakdown voltage is referred to as “Geiger mode” since a single photon can cause an avalanche breakdown. The Geiger discharge yields a high gain of typically 10^5 to 10^6 .

2.2 The Silicon Photomultiplier

A recent development in the field of solid-state photodetectors is the *Silicon Photomultiplier* (SiPM) [21] [22]. A SiPM basically consists of an array of APDs joint together on a common silicon substrate. Figure 2.10 shows a picture of a SiPM produced by MEPHI²-PULSAR³ as it is used in the analogue hadronic calorimeter prototype. It consists of $34 \times 34 = 1156$ APDs or “pixels” on a surface area of $1 \times 1 \text{ mm}^2$. Each pixel is operated above breakdown voltage (Geiger

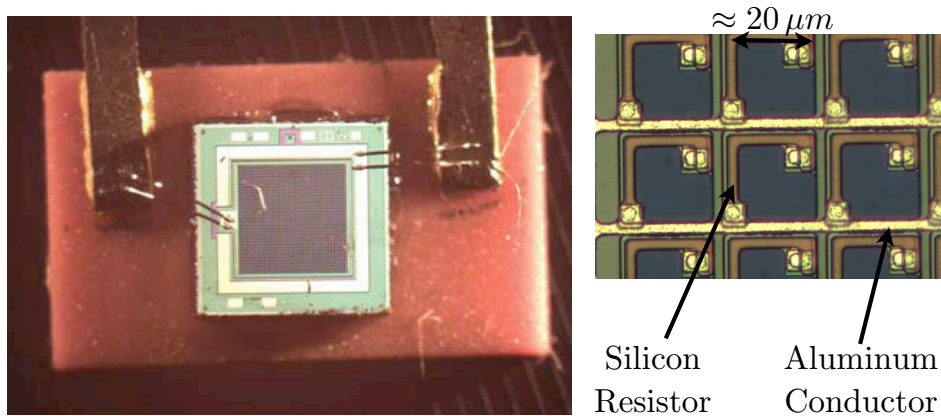


Figure 2.10: Left: Picture of a SiPM produced by MEPHI-PULSAR with an active surface of $1 \times 1 \text{ mm}^2$. **Right:** Microscopic picture of single pixels also showing the silicon resistors and the aluminum conductors which connect all the pixels [23].

mode) so each electron-hole pair generated by photon absorption or thermal excitation gives rise to a Geiger discharge. A passive quenching mechanism is implemented to stop the discharge by connecting each pixel to a silicon resistor (see figure 2.10 and 2.11). Each pixel operates as a binary device since the output signal of a Geiger-mode APD (GAPD) does not depend on the number of photons which triggered the avalanche breakdown. The dynamic range of a single GAPD is limited due to the time which is needed to recharge the GAPD after an avalanche breakdown (recovery time). By putting many GAPDs to a small surface the dynamic range is increased. All SiPM pixels are connected to a common load, so the output signal is a sum of the signals from all pixels. This allows to determine the intensity of the incident light which is connected to the number of pixels fired.

Figure 2.11 shows a schematic view of the SiPM topology. The individual pixels have a typical size between $20 \times 20 \mu\text{m}^2$ and $100 \times 100 \mu\text{m}^2$ depending on the particular device. The layout of the individual pixels is similar to the layout of the APD discussed in section 2.1 (see figure 2.5). A drift region is formed by an epitaxy layer with a width of a few micron on low resistive p substrate. If an electron-hole pair is generated in this region the electron will drift into the high-field (typically $(3 - 5) \cdot 10^5 \text{ V/cm}$) region where it can trigger an avalanche breakdown. A key feature of the SiPM is the high intrinsic gain of 10^5 to 10^6 which allows the detection of single photons with a good signal to noise ratio. Depending on the pixel size a photon detection efficiency (PDE) of up to 50% can be reached. The traditional Photomultiplier tube (PMT) provides a gain and PDE of similar order. However, the SiPM has several advantages compared to a PMT or APD:

²Moscow Engineering and Physics Institute

³Pulsar Enterprise, Moscow

- SiPMs are robust and very small in size compared to the bulky and fragile PMTs.
- Unlike PMTs, SiPMs are insensitive to magnetic fields.
- The bias voltage applied to the SiPM is usually below 100 V compared to the PMT operation voltage of typically 2 kV.
- The limited number of pixels limit the output power of a SiPM and thus protect the sensor from excessive photocurrents at high light intensities.
- Very small nuclear counter effect (small sensitivity to charged particles traversing the device) due to Geiger mode operation.
- Low excess noise (see below) which allows to clearly separate the single photon signal from the noise.
- The production costs for SiPMs can be expected to be low for future mass production.

These features make the SiPM a promising device for many applications. However, there are several drawbacks like the high dark-rate of typically 0.5 MHz, optical cross-talk and after-pulses and a limited dynamic range. The different features of the SiPM are discussed in detail in the following sections.

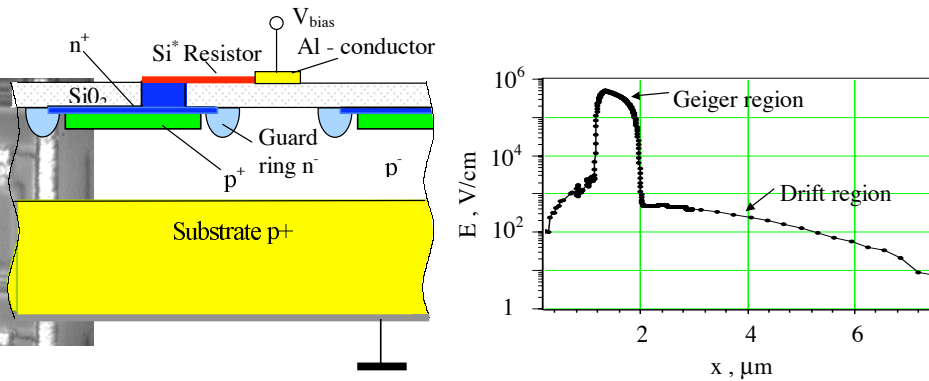


Figure 2.11: Left: Schematic view of a SiPM pixel. Each pixel is an APD operated in Geiger mode. Right: Profile of the electric field in a pixel [24].

Pulse Shape and Gain

The behavior of a SiPM pixel can be explained by a simple circuit model which is shown in figure 2.12. Each pixel can be in two different states which have to be treated separately. Figure 2.12 a) represents the situation when no electron-hole pair is generated. In this “detection mode” the full bias voltage ($V_{\text{bias}} > V_{\text{break}}$) is applied to the p-n-junction since no current is flowing. Figure 2.12 b) shows the equivalent circuit in the case of an avalanche breakdown [20]. The pixel can be described by a voltage source in series with a resistor R_{int} which corresponds to the resistance of the aluminum lead and aluminum-silicon contact. C_{pixel} represents the capacitance of the p-n-junction (see equation 2.1). The quenching resistor R_q causes a virtually

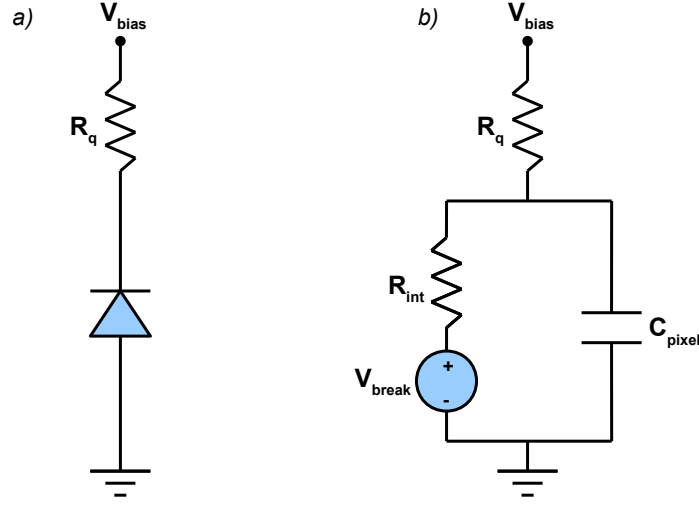


Figure 2.12: Passive quenching circuits. **a)** In detection mode the pixel is charged up to some bias voltage $V_{bias} > V_{break}$. **b)** During an avalanche breakdown the pixel behaves according to a simple circuit mode. The quenching resistor $R_q \gg R_{int}$ functions as a virtual open circuit on the time scale of the discharge $\tau = RC_{pixel}$ and then recharges the pixel with a slow time constant $\tau_{recovery} = R_q C_{pixel}$ [20].

open circuit ($R_q \gg R_{int}$) on the short time scale of the discharge. The charge Q flowing out of the capacitor during discharge is described by the following formula:

$$Q(t) = C_{pixel} \cdot (V_{bias} - V_{break}) \cdot (1 - e^{-\frac{t}{R_{int}C_{pixel}}}) \quad (2.4)$$

Figure 2.13 shows a typical SiPM output signal for one firing pixel. The trailing edge of the signal is associated with the current $dQ(t)/dt$. The width of the pulse therefore is determined by the time constant $R_{int}C_{pixel}$. The total integrated charge of a pulse corresponds to the gain G of the pixel which is proportional to the over-voltage $V_{over} = V_{bias} - V_{break}$ and the pixel capacitance:

$$Q = C_{pixel} \cdot (V_{bias} - V_{break}) = G \cdot q_e \quad (2.5)$$

where q_e is the elementary charge.

Once the avalanche has been quenched with the help of the quenching resistor R_q the pixel is slowly recharged with time constant $\tau_{recovery} = R_q C_{pixel}$ which corresponds to the recovery time of the pixel. During recovery the gain of the pixel is lower due to the reduced over-voltage. This is described by the following equation [25]:

$$G(t) = G_0 \cdot (1 - e^{-\Delta t / \tau_{recovery}}) \quad (2.6)$$

where G_0 is the gain of the fully recovered pixel and Δt is the time after the preceding pulse. For high photon fluxes this effect limits the dynamic range of the sensor.

Dynamic Range

The SiPM is operated in Geiger mode which means that a pixel always produces the same amount of charge no matter how many photons hit the pixel at the same time. In order to

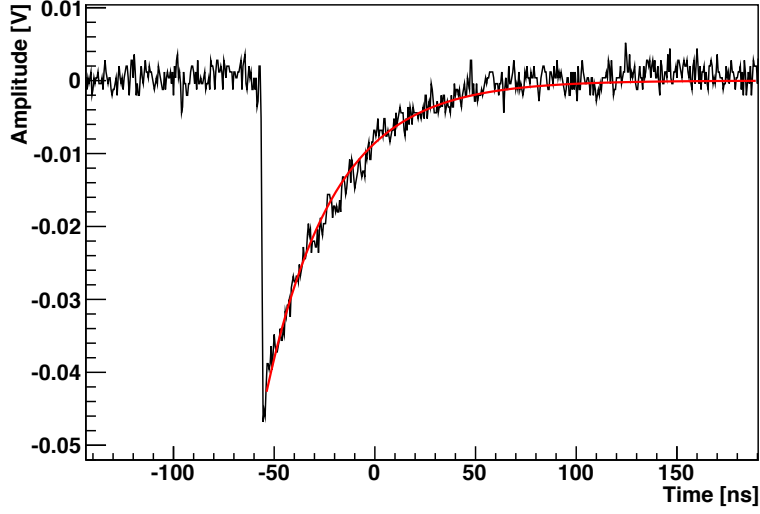


Figure 2.13: Typical SiPM signal with only one firing pixel (recorded with a HAMAMATSU S10362-11-100C amplified by a factor 50). The trailing edge can be described by equation 2.4 (red curve)

detect several photons simultaneously the SiPM consists of an array of typically 100 to 1600 pixels per square millimeter. The pixels are connected to a common load so that the resulting output signal Q_{Signal} is the sum of the individual pixel signals Q_{pixel} :

$$Q_{Signal} = N_{fire} \cdot Q_{pixel}$$

where N_{fire} is the number of fired pixels.

For low photon fluxes the probability that a pixel is hit by more than one photon at the same time is small. In this case the response of the sensor is in good approximation linear. If the number of photons is of the order of the number of pixels, the response of the SiPM saturates due to the recovery time of the pixels. The dynamic range of a SiPM hence is limited by the number of pixels. Considering the probability for a fixed number of incident photons N_γ to hit a certain number of pixels, the response N_{fire} (number of pixels fired) can be described by the following formula [26]:

$$N_{fire} = N_{total} \cdot \left(1 - e^{-\frac{PDE \cdot N_\gamma}{N_{total}}}\right) \quad (2.7)$$

where N_{total} is the total number of pixels and PDE denotes to the photon detection efficiency. The relation is illustrated in figure 2.14.

Photon Detection Efficiency

The photon detection efficiency (PDE) is usually defined as the probability to detect a photon hitting the sensor and is a measure of the sensitivity of the device. In the case of the SiPM it depends on several parameters and can be expressed by the following equation:

$$PDE = QE \cdot \epsilon_{geo} \cdot \epsilon_{avalanche} \cdot (1 - R) \quad (2.8)$$

A certain fraction of the incident photons are reflected at the surface of the sensor and hence cannot be detected. The factor $(1 - R)$ describes the probability for a photon to permeate the

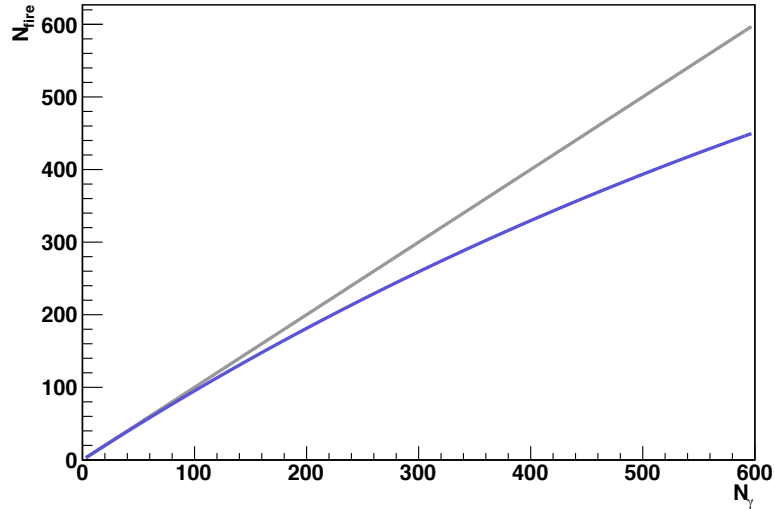


Figure 2.14: Simulated response of a SiPM with 1000 pixels and a PDE of 100% (blue) and as a function of the number of incoming photons N_γ . For high photon fluxes there is a strong deviation from linearity (grey) caused by saturation effects due to the limited number of pixels.

covering layer. The silicon resistors and aluminum conductors which connect all pixels are not photon-sensitive and therefore reduce the active area of the sensor. This is taken into account by the so-called “geometrical efficiency” ϵ_{geo} which is defined as the fraction of the active surface to the total surface of the device $\epsilon_{geo} = A_{active}/A_{total}$. This fraction depends primarily on the pixel size. SiPMs with a large pixel size have a larger geometrical acceptance which results in a larger PDE.

The quantum efficiency QE is defined as the percentage of photons hitting the active surface that will produce an electron-hole pair. This value is closely related to the absorption coefficient introduced in equation 2.3 and therefore strongly dependent on the wavelength of the photons. The sensitivity for photons with short wavelength is limited by the thickness of the covering layer due to their very short absorption length. For low energetic photons there is a cut-off in the sensitivity at the point where the photon energy is smaller the energy of the band gap.

When an electron-hole pair is created the probability to trigger an avalanche breakdown is given by the factor $\epsilon_{avalanche}$. This factor increases with the applied bias voltage and depends on the position at which the charge carriers are produced since the probability to initiate a Geiger discharge is smaller for an electron created close to the p-n-junction than for an electron produced in the center of the p-layer.

Excess-Noise

The pixels of a SiPM underlie variations in the quenching resistance and the doping concentration due to the manufacturing process which lead to variations in the breakdown voltage and pixel capacitance. As a consequence the charge generated in an avalanche breakdown varies for every pixel which leads to fluctuations in the response of the sensor. This effect is known as *Excess Noise*. In addition there is a contribution from the electronic noise which arises from the readout electronics. The variation of the n-pixel signal can be described according to the

following equation:

$$\sigma_n = \sqrt{\sigma_0^2 + n \cdot (\sigma_1^2 - \sigma_0^2)} \quad (2.9)$$

where σ_0 is the electronic noise and σ_1 is the fluctuation in the single photon signal. In the literature this effect is often characterized by the *Excess Noise Factor* (ENF):

$$ENF = 1 + \frac{\sigma_1^2 - \sigma_0^2}{G^2}$$

where G is the gain of the device.

Dark Counts and After-pulses

Electron-hole pairs are not only created by photon absorption but they can also be produced when no light hits the sensor. The signals from this “dark counts” cannot be distinguished from real photon-induced events. Typically the dark count rate (dark-rate) for a SiPM is of the order of $500 - 1000 \frac{\text{kHz}}{\text{mm}^2}$. Although the mean dark-rate can be determined and subtracted from the measured signal, the variance of this value remains as a source of noise and degrades the signal resolution. There are three main processes which contribute to the dark-rate.

Thermal Pulses

At room temperature the charge carriers in the semiconductor have a thermal energy of $E_{th} = k_b T = 0.0259 \text{ eV}$. Electrons can be directly lifted into the conduction band if the thermal energy is larger than the band gap energy of the material. In case of silicon ($E_{gap} \approx 1.14 \text{ eV}$) direct transitions are suppressed, however, thermal excitation can also occur by a two-step transition involving intermediate states within the forbidden energy range. These intermediate states are introduced by impurities and crystal defects. The thermal rate therefore depends on the impurity density and the temperature.

Tunnel Excitation

Another process which contributes to the dark-rate is the so-called “tunnel excitation”. The process is based on the quantum-mechanical phenomena that allows particles to “tunnel” through a potential barrier with a certain probability. Figure 2.15 shows the energy bands as a function of position in the presence of an electric field. The potential barrier between the p- and n-layer is approximately triangular in shape. The height of the barrier is equivalent to the band gap energy E_G and the width is given by:

$$L = \frac{E_G}{q_e \mathcal{E}}$$

where q_e is the electron charge and \mathcal{E} is the electrical field. Electrons in the p-layer can tunnel through the band gap into a state with the same energy in the conduction band of the n-layer. This process leaves a hole in the valence band of the p-layer. The probability for an electron to tunnel through a triangular shaped potential barrier can be calculated with the *Wentzel-Kramer-Brillouin* approximation [15]:

$$P_{tunnel} \approx \exp \left(-2 \int_0^L \sqrt{\frac{2mE(x)}{\hbar^2}} dx \right) = \exp \left(\frac{-4\sqrt{2m}E_G^{3/2}}{3q_e \hbar \mathcal{E}} \right) \quad (2.10)$$

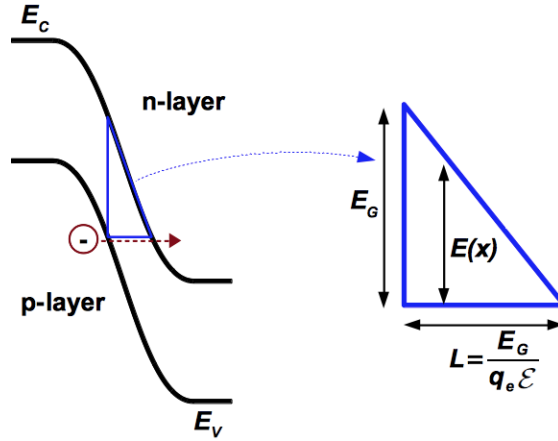


Figure 2.15: Schematic view of tunnel excitation. **Left:** Energy bands in the presence of an electric field. An electron can tunnel through the forbidden band from the p-layer to the n-layer resulting in a free electron-hole pair. **Right:** The potential barrier between the valence band of the p-layer and the conduction band of the n-layer can be approximated by a triangular shape.

The tunneling probability increases with the electrical field since the width of the potential barrier decreases. For this reason, tunneling processes play an important role for the dark-rate due to the high electric field in the multiplication region of the SiPM. Unlike thermal pulses, this effect cannot be reduced by cooling of the device.

After-pulses

Charge carriers produced in an avalanche breakdown can be captured by lattice defects in the depletion layer (trapping centers) forming meta-stable states. After a certain time the charge carrier is released and may initiate an additional avalanche breakdown. This results in a fake photon signal (after-pulse) succeeding the initial pulse. If the trapped charge carrier is released within the recovery time of the pixel, the signal of the associated after-pulse will be reduced. This effect enlarges the fluctuations in the charge contributed by after-pulses. The noise introduced by after-pulses can practically be reduced by increase the quenching resistance in order to increase the recovery time of the pixels (see equation 2.6). However, a large recovery time reduces the dynamic range of the sensor and limits the timing resolution.

Thermal Noise Time Distribution

Thermal pulses and after-pulses cannot be distinguished on a single event basis but it is possible to separate them statistically by their different characteristic time constants. Considering only the thermal rate, the observed number of pulses n within a given time interval Δt follows a Poissonian distribution:

$$P_{\lambda\Delta t}(n) = \frac{(\lambda\Delta t)^n}{n!} e^{-\lambda\Delta t}$$

where $\lambda\Delta t$ is the expectation value of the Poisson distribution and λ is the thermal pulse rate. The probability for a pulse to occur at a time t is given by the probability density function $p_{tp}(t)$ which can be derived in the following way [26]:

The probability to measure no pulse within Δt must be equal to the probability to detect the pulse after Δt which leads to the following relation:

$$P_{\lambda\Delta t}(0) = e^{-\lambda\Delta t} \stackrel{!}{=} 1 - \int_{\Delta t}^{\infty} p_{tp}(t)dt$$

From this equation the probability density can be derived as:

$$p_{tp}(t) = \frac{1}{\tau_{tp}} \cdot e^{-\frac{t}{\tau_{tp}}} \quad (2.11)$$

where $\tau_{tp} = \frac{1}{\lambda}$ is the time constant for the thermal pulses.

The time distribution for the after-pulses can be derived in the same way. In practical devices there can be several different kinds of trapping centers for electrons and holes with different trapping times. Considering all after-pulse components and thermal pulses the time distribution can be expressed by the sum of all contributions:

$$p(t) = \sum_i \frac{1}{\tau_i} \cdot e^{-\frac{t}{\tau_i}} \quad (2.12)$$

Cross-talk

During an avalanche breakdown photons are produced due to recombination of charge carriers, bremsstrahlung and intraband transitions. The generated photons can enter neighboring pixels and trigger an additional avalanche if the photon energy is sufficiently high. This process is called “optical cross-talk”. The statistical fluctuations in number of cross-talk events degrade the resolution of the SiPM signal.

Photon signals faked by cross-talk occur simultaneously to the original signal which allows to distinguish them from after-pulse events. The probability per charge carrier to generate a photon with an energy larger than the energy of the band gap is of the order of 10^{-5} [27]. For a typical gain of $G = 10^6$ this results in approximately 10 photons per avalanche. However, the probability for a photon to reach a neighboring pixels is low due to the short absorption length of a few micrometers compared to the typical distance between pixels of $\approx 15 \mu\text{m}$. This results in a typical cross-talk probability of P_{CT} in the order of 10%. The cross-talk probability can be reduced by isolating the individual pixels with trenches which serve as optical boundaries (see figure 2.16).

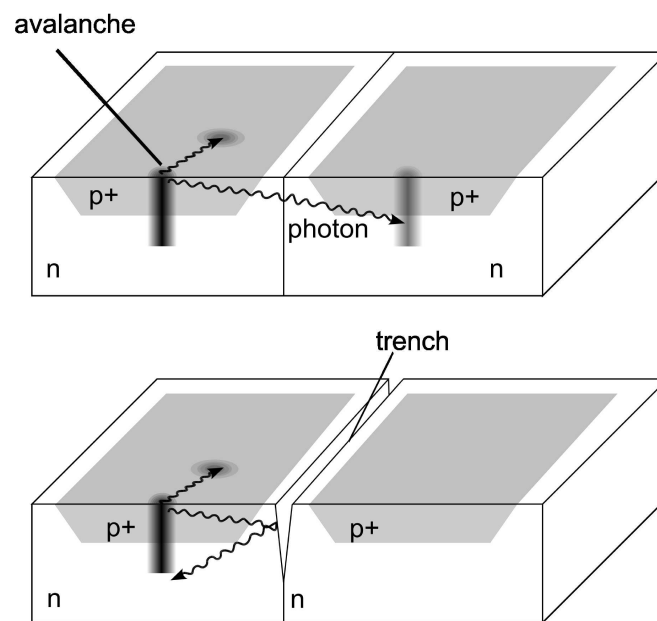


Figure 2.16: A schematic of optical cross-talk between two neighboring pixels. Photons generated in an avalanche breakdown can travel to nearby pixels and trigger an additional avalanche (top). This process can be prevented by trenches between the individual pixels (bottom) [28].

Chapter 3

The SiPM Test Stand

There are several types of SiPMs from different manufacturers on the market, all with different characteristics. A test stand has been developed [13] to compare and characterize the different sensors in order to find the device best suited for a particular application like calorimetry in high energy physics or positron emission tomography in medical imaging. This test stand allows to determine the gain, dark-rate and relative spectral sensitivity as a function of the over-voltage. In the context of this thesis, the test stand was largely enhanced in order to measure the cross-talk and after-pulse probability and the PDE (without the effects of dark-rate, cross-talk and after-pulses). Furthermore, the new setup allows to determine the temperature dependence of different parameters and provides a setup allowing to study the spatial uniformity in the response of the sensor. Besides this new features of the test stand, a central task of this thesis was to automate the different measurements and data analysis in order to achieve a simpler and faster characterization procedure.

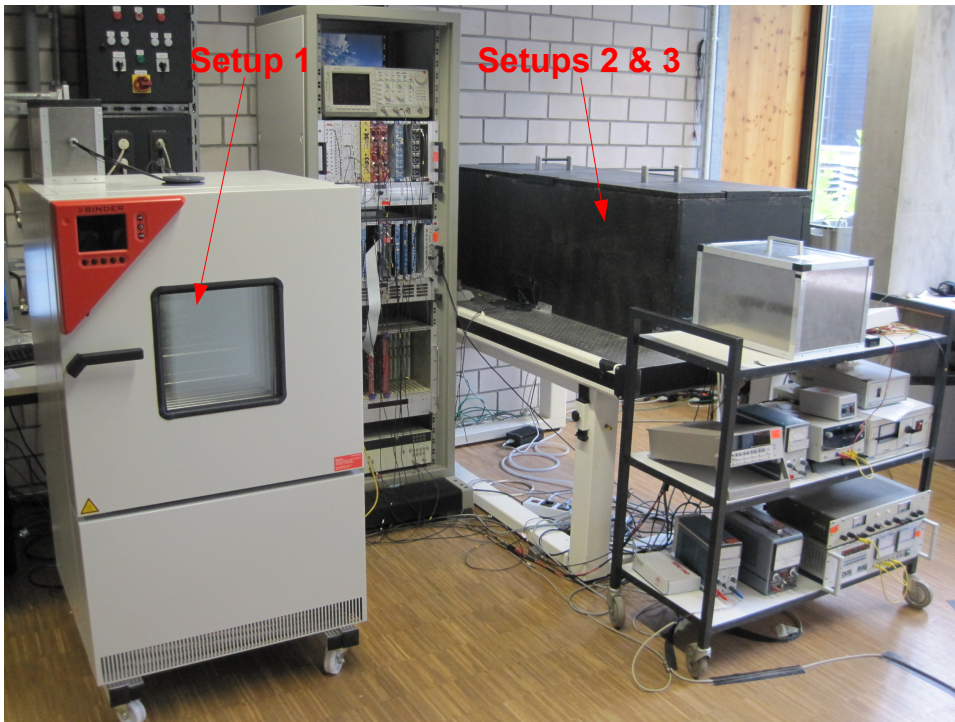


Figure 3.1: Picture of the SiPM test stand. The setup for the gain, dark-rate, cross-talk and after-pulse measurement is contained in a temperature chamber (setup 1). The setups for the PDE measurement and the sensor scans are located in a large lightproof box (setups 2&3).

3.1 Overview

Figure 3.1 shows a picture of the SiPM test stand which consists of three major experimental setups. Before discussing the different setups in detail a brief overview of the measurements is presented.

Setup 1

In this setup the SiPM is located in a small lightproof metal box which is placed inside a temperature chamber. A laser diode is placed in a separate lightproof box which is connected to the SiPM box with an optical fiber bundle to guide the light from the laser diode to the sensor. The following measurements can be done with this setup:

- **Gain Measurement:** The sensor is illuminated with a pulsed laser diode and the charge spectrum is measured using a *Charge-to-Digital Converter* (QDC). The integrated charge of the signal corresponding to one detected photon is associated with the gain of the SiPM. The break-down voltage of the sensor can be determined from the over-voltage dependence of the gain.
- **Dark-Rate and Cross-talk Measurement:** If the sensor is not illuminated, there still are signal pulses due to the dark-rate which can be measured by counting the pulses with a scaler module. The input signals for the scaler are produced by a discriminator which only generates an output pulse if the SiPM signal exceeds a certain discrimination threshold. With this setup the dark-rate can be measured as a function of the discrimination threshold and the bias voltage. This measurement also provides information about the cross-talk. Since the two pixel signals are predominantly caused by cross-talk events, the cross-talk probability can be determined by comparing the rates of events with one and two pixels fired.
- **After-pulse Measurement:** A *Time to Digital Converter* (TDC) is used to measure the time intervals between dark-rate pulses. The resulting time distribution allows to determine the time constants for thermal pulses and after-pulses and the after-pulse probability.
- **Temperature Measurement:** The temperature chamber can be used to execute the measurements listed above at different temperatures. In this way the temperature dependency of the gain, dark-rate, cross-talk and after-pulse probability can be determined.

Setup 2: Photon Detection Efficiency

The setup for the PDE measurement is placed in a big lightproof box on an optical table since it is too large to fit in the temperature chamber. The key component of the setup is an integrating sphere which is used to uniformly distribute the incident light to the SiPM and a calibrated sensor referencing the light intensity. The sensitivity of the sensor can be measured over a wide spectral range from 300 nm to 1000 nm using a Xenon lamp in combination with a monochromator, which selects a small wavelength interval from the spectrum of the lamp. The measured sensitivity is influenced by dark-rate, cross-talk and after-pulses since the continuous light source requires the SiPM to be read out with an amperemeter. If a pulsed laser diode is used as a light source the SiPM can be read out with a QDC. Applying a statistical analysis

on the measured charge spectrum the PDE can be determined without the effects of cross-talk and after-pulses. Although this measurement is confined to the fixed wavelength of the laser diode, the PDE can be determined for the spectral range from 300 nm to 1000 nm by combining the two methods.

Setup 3: Sensor Scans

The second setup in the big lightproof box allows to study the response of single pixels of a sensor. For this purpose the SiPM is mounted on a micrometer positioning stage and scanned with a focused light spot with a few micrometer in diameter which is produced by a pulsed laser diode. In this way the response of single pixels can be studied which allows to determine the spatial uniformity in the sensitivity, gain and cross-talk of the sensor.

3.2 Charge Spectrum

The measured charge spectrum of the SiPM provides a large variety of information, e.g. the gain and the number of detected photons. In addition one can observe the effects of dark-rate, cross-talk and after-pulses. This makes the charge spectrum a powerful indicator for the characterization of SiPMs. Figure 3.2 shows the setup used to measure the charge spectrum.

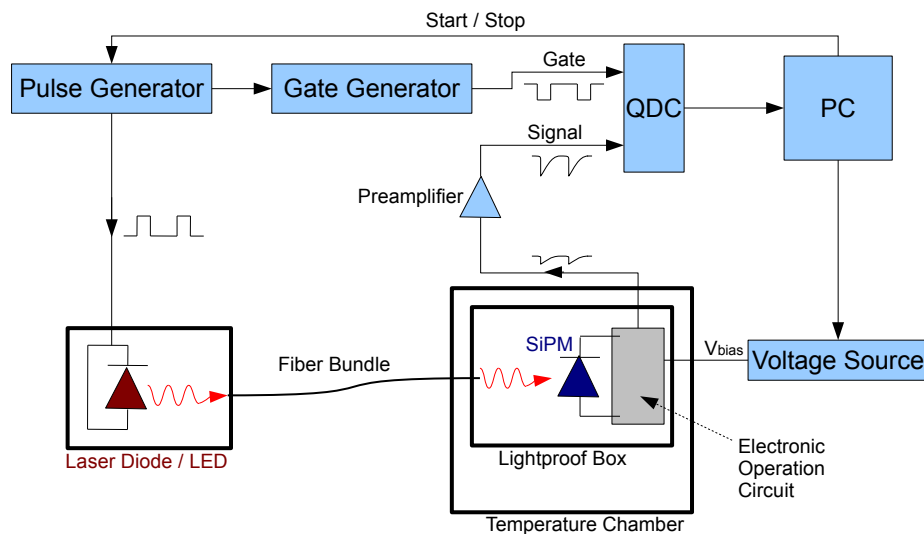


Figure 3.2: Schematic view of the setup used to measure the charge spectrum. The integrated charge of the output signal of the SiPM is measured using a QDC.

The basic principle of the measurement is to illuminate the SiPM with a pulsed light source and measure the integrated charge of the output signal using a 10-bit *Charge-to-Digital Converter* (QDC)¹. Before the charge integration the signal from the SiPM is amplified by a factor 50 using a fast preamplifier². The integration time of ≈ 100 ns (depending on the pulse shape of

¹LeCroy Model 2249A, 12-Channel Charge Integrating ADC

²Phillips Scientific Model 774, Bandwidth: 100kHz-1,5 GHz (3dB)

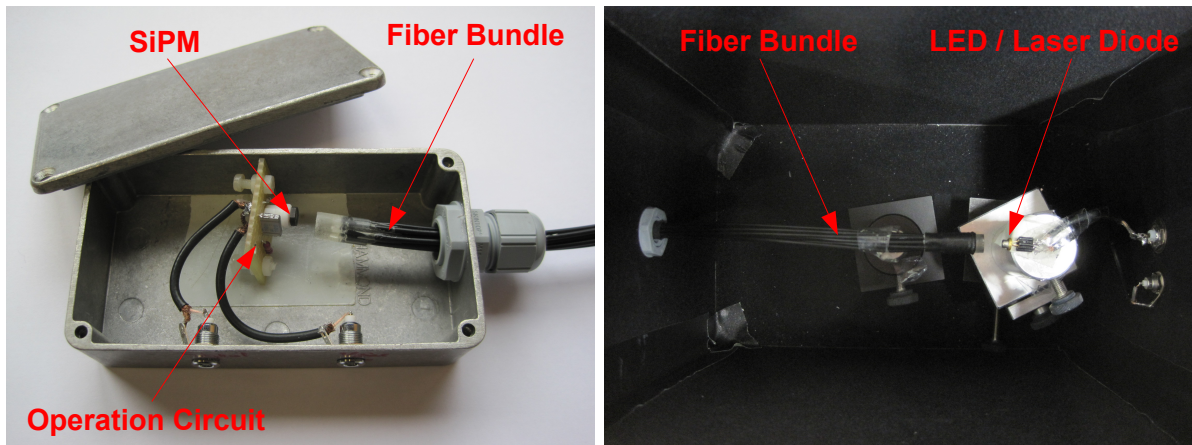


Figure 3.3: **Left:** Lightproof box containing the SiPM, the biasing circuit and two LEMO connectors for the output signal and the bias voltage. The fibre bundle is coupled to the surface of the SiPM using a plastic fixture (not shown in the picture). **Right:** Inside view of the lightproof box containing the LED / laser diode. The light is guided to the SiPM via an optical fibre bundle.

the sensor) is set by a gate generator³ which is triggered independently from the SiPM signal by a pulse generator⁴ used to drive the light source.

The SiPM is placed in a lightproof $11 \times 6 \times 3 \text{ cm}^3$ metal box (see figure 3.3) in order to shield the sensor from ambient light and electronic noise. Two LEMO connectors for the output signal and the bias voltage were mounted on the box. The SiPM is operated utilizing the electrical circuit shown in figure 3.4 [29]. The box is placed in a temperature chamber⁵ (see section 3.4) which is essential in order to ensure stable and reproducible measurement conditions. All the following measurements were done at a constant temperature of $25.0 \pm 0.1 \text{ }^\circ\text{C}$.

The SiPM is illuminated using different LEDs and laser diodes which are driven by a pulse generator. In this way light pulses with a length of a few nanoseconds and a period of $40 \mu\text{s}$ are produced. The utilized LED or laser diode is placed in a separate lightproof metal box (see figure 3.3) outside the temperature chamber to avoid pick-up noise on the SiPM readout circuit. An optical fiber bundle connecting the two boxes is used to guide the light to the SiPM.

The data acquisition is based on the CAMAC standard and controlled by a Wiener CC-USB CAMAC crate controller which is connected to the lab computer. The measurement speed was significantly increased with respect to the original setup by utilizing the internal data stack of the CC-USB CAMAC controller. This stack provides a 4096 words buffer where QDC values can be stored and which can be read out at once, instead of transferring every data point individually to the computer. This increases the measurement speed by a factor ≈ 100 . Since the measurement of the charge spectrum is a basic component of many other measurement setups, this is an important step for characterizing and comparing many sensors in a short time.

A LabVIEW⁶ program was designed to automatically record charge spectra in a predefined range for the bias voltage and calculate the gain and the number of detected photons for each

³CAEN Dual Timer Mod. N93B

⁴Hewlett-Packard P 8130A 300MHz Pulse Generator

⁵Binder MK 53

⁶National Instruments LabVIEW 8

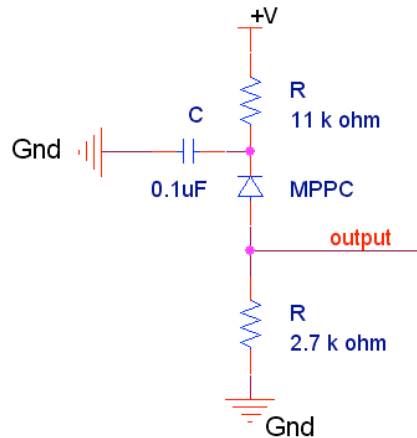


Figure 3.4: Basic connection diagram for the SiPM [13].

spectrum. The break-down voltage and pixel capacitance can be extracted from the measured bias voltage dependence of the gain (see equation 2.5). The analysis of the charge spectra will be discussed in detail in chapter 4.1.

3.3 Dark Count Measurements

Besides photon absorption, a SiPM pulse can also be triggered by tunneling and thermal excitation of electrons in the sensitive layer of the SiPM (see chapter 2.2). These dark counts degrade the resolution of the SiPM signal and therefore are an important characteristic of a sensor. In the following the setup used to measure the rate and time distribution of the dark counts is presented. A schematic view of the setups is shown in figure 3.5.

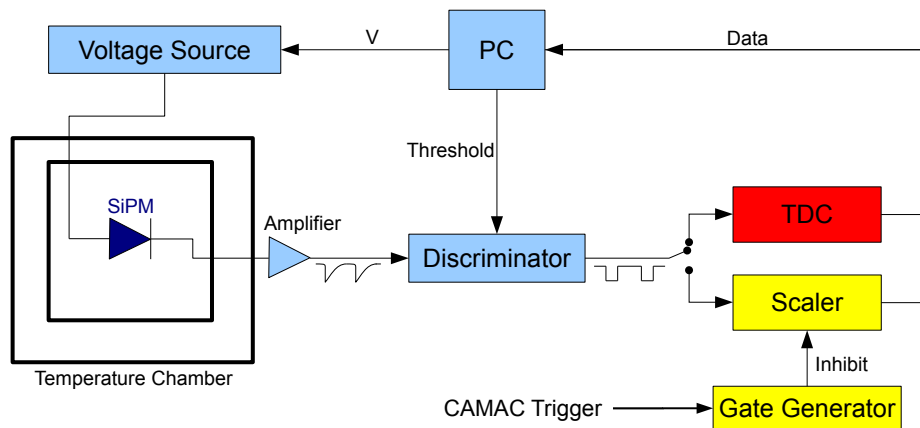


Figure 3.5: Setup for the dark-rate measurement. A Scaler (yellow) is used to count the SiPM pulses in order to measure the dark-rate at the given discriminator threshold. A TDC (red) is used to measure the time distribution of the dark-rate pulses.

Rate Measurement

The basic concept of the measurement is to count all dark-rate pulses within a certain time interval. For this purpose a discriminator⁷ generates a logical output pulse if the amplitude of the SiPM signal exceeds a certain threshold which can be adjusted by the lab computer. The output pulses of the discriminator are counted by a scaler module⁸ as long as no signal is present on the inhibit input. The inhibit signal is set by a gate generator⁹ and is interrupted for a time interval of $t = 1$ s if the gate generator receives a trigger signal from the CAMAC crate controller. The counted number of pulses therefore reflects the dark-rate (corresponding to the applied discriminator threshold) in Hz.

The measurement was automated by means of a LabVIEW program which records the dark-rate in a certain range for the discrimination threshold with a typical step size of a few mV. This measurement is done for a sequence of the bias voltages. The acquired data can be automatically analyzed with a ROOT¹⁰ program which determines the dark-rate as a function of the bias voltage. Besides the dark-rate also the crosstalk probability is determined from the ratio of the rates of events with one and two pixels fired. This analysis will be discussed in chapter 4.3 in detail.

Time Distribution of Dark-Rate Pulses

The measurement of the time spectrum of dark-rate events is a completely new feature of the test stand which allows to determine the after-pulse probability and corresponding trapping time constants.

If the SiPM is read out with an integrating amplifier collecting the charge on a capacitor as implemented in the CALICE HCAL prototype, after-pulses which occur during the integration time will degrade the resolution of the output signal by faking a photon signals. This effect is even worse considering after-pulses from pixels which are not fully recovered. These after-pulses only contribute a reduced amount of charge which results in a broadening of the measured charge spectrum. Another problem are late after-pulses which occur after the primary integration window and thus can fake signals in subsequent bunch crossings. These effects complicate the calibration of the calorimeter cells and are a limiting factor for the energy resolution. For this reasons a sensor with a low after-pulse probability is desired.

The total dark-rate consists of the thermal pulse rate and the after-pulse rate. A thermally generated pulse cannot be separated from an after-pulse by its pulse shape, however, it is possible to separate them statistically by their characteristic time constants τ_{ap} and τ_{tp} since the pulses are generated by different mechanisms. For the measurement of the time distribution the setup for the rate measurement described above is slightly modified by replacing the scaler module with a *Time-to-Digital Converter*¹¹ (TDC). The time intervals Δt between the discriminator pulses are measured by the TDC with a precision of 25 ps by generating a random start signal and measuring the time stamp for every output signal from the discriminator (see figure 3.6) which generates a logical output pulse if the input signal amplitude exceeds a certain threshold. The after-pulse probability, thermal- and after-pulse rate can be determined from the resulting histogram of the measured time intervals which corresponds to the time distribution of

⁷LeCroy 4416

⁸LeCroy 2550B, 100MHz Scaler

⁹CAEN Model V93B

¹⁰www.root.cern.ch

¹¹CAEN V1290A

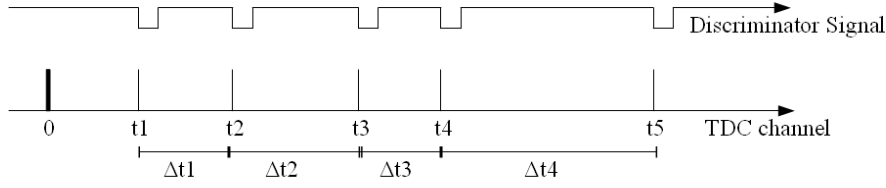


Figure 3.6: Measurement of the dark-rate timing distribution. A discriminator generates an output pulse if a dark-rate pulse exceeds a certain discrimination threshold. The time intervals between the discriminator pulses are measured with a TDC.

consecutive dark-rate pulses (see chapter 4.4).

The time spectra are automatically recorded within a certain range of the bias voltage specified in the LabVIEW program which controls the measurement. The measurement time for a spectrum with 10^7 samples is in the order of 10 s. The analysis of the recorded time spectra is done by a ROOT program which determines the after-pulse probability and the time constants for the thermal- and after-pulses as a function of the bias voltage.

3.4 Temperature Measurements

In the setups described in the previous sections the temperature chamber was used to assure a constant measurement temperature which is essential for the comparability of results. However, the temperature chamber can also be used to determine the temperature dependence of the SiPM properties measured with the different setups (i.e. gain, break-down voltage, dark-rate, crosstalk- and after-pulse probability). It can be operated from -40°C up to 180°C with a precision of $\approx 0.1^\circ\text{C}$ and a stability of $< 0.1^\circ\text{C}$.

Figure 3.7 shows the schematic of the setup and a picture of the temperature chamber used for the measurements. The LabVIEW programs controlling the different measurements discussed in the previous sections were modified in order to automatically perform the measurements within a certain range for the temperature. The measurements presented in chapter 4.5 were done in a temperature range from -10°C to 30°C with 4°C steps. For every measurement temperature a waiting period of ≈ 30 minutes is necessary in order to reach a stable temperature with a precision of $\approx 0.1^\circ\text{C}$. This results in a typical measurement time of ≈ 5 hours for the specified temperature range.

The break-down voltage of a SiPM is temperature dependent which implies the need for an adjustment of the bias voltage for every temperature step in order to measure the different characterizing parameters at the same over-voltage. Executing the gain measurement described in section 3.2 for different temperatures, the temperature dependence of the break-down voltage can be determined. This can be used to adjust the bias-voltage so that the rate and timing measurements described in section 3.3 are executed at a fixed over-voltage for the different temperatures.

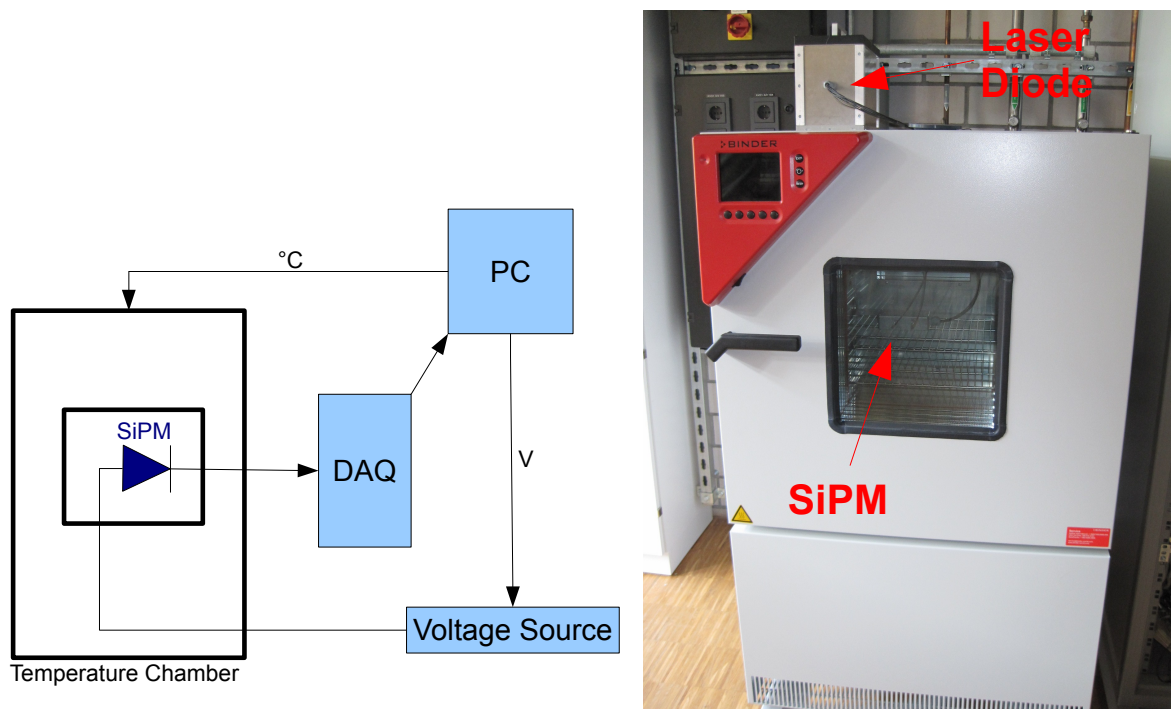


Figure 3.7: Left: Schematic view of the temperature measurement setup. The measurements were done for a temperature range from -10°C to 30°C with 4°C steps. **Right:** Picture of the temperature chamber containing the lightproof box with the SiPM. The box containing the LED / laser diode is placed on top of the chamber.

3.5 Photo Detection Efficiency

The photon detection efficiency (PDE) is a central property of a photodetector and for this reason crucial for a complete characterization of a SiPM. The original setup for the PDE measurement [13] was upgraded in order to allow a more accurate study of the PDE. The new setup is based on a different measurement concept which allows to determine the PDE without the effects of cross-talk and after-pulses. The basic principle of the measurement is to determine the response of the SiPM to a well known amount of light. The measurement cannot be done inside the temperature chamber due to the dimensions of the setup and hence is located inside a big lightproof box on an optical table. Figure 3.8 shows the schematics of the experimental setup.

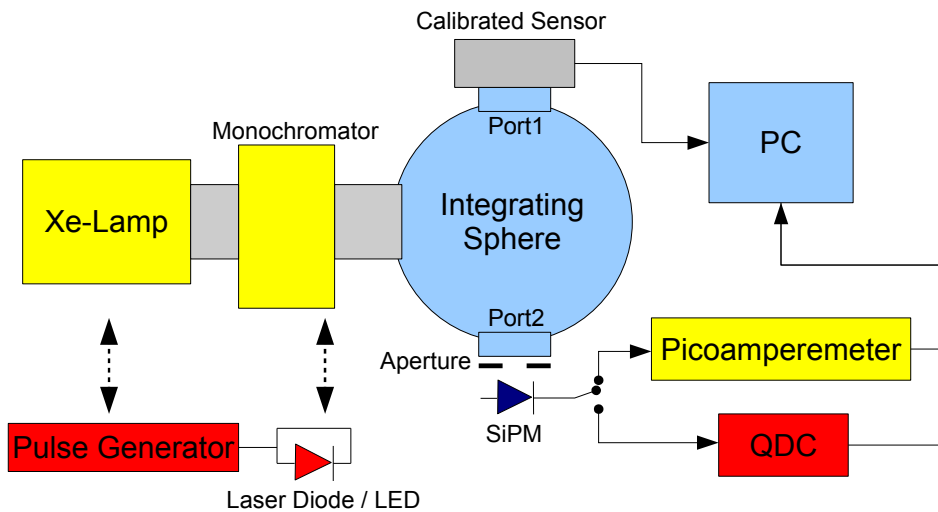


Figure 3.8: Schematic view of the setup for the measurement of the photon detection efficiency. The Xenon lamp is used as a light source for the measurement of the relative spectral sensitivity (yellow modules). For this measurement the SiPM is read out with a picoamperemeter. For the measurement of the PDE (red modules) without the effects of dark-rate, cross-talk and after-pulses a laser diode (or LED) driven by a pulse generator serves as a light source allowing to read out the sensor with a QDC.

In the following, the different components of the setup are discussed in detail.

Integrating Sphere

The central component of the setup is an integrating sphere¹² which is an optical device consisting of a hollow spherical cavity with one entrance and two exit ports. The interior of the cavity is coated with a highly reflective material so that the incident light is homogeneously distributed over the sphere due to multiple scattering. In this way, the output characteristics (light power and angular distribution) of the sphere do not depend critically on the direction of the incoming beam of light. The integrating sphere can be operated for wavelength from 300 nm to 1000 nm which is important in order to determine the PDE in a wide spectral range. The advantage of the integrating sphere with respect to the original setup is that the sensors

¹²Newport Integrating Sphere

can be attached directly to the sphere and no additional optical instruments are necessary to focus the light onto the sensor.

Figure 3.9 shows a picture of the integrating sphere. A NIST¹³ certified calibrated photodiode is mounted on the upper exit port providing a reference measurement for the light intensity. The SiPM is placed at the second exit port behind a brass aperture with a diameter of either 0.6 mm or 0.8 mm to make sure that only the active area of the sensor is illuminated. The aperture is attached to a custom built fixture mounted on the front port of the integrating sphere (see figure 3.9). The geometry and dimensions of the inner part of the fixture are designed in such a way that also the calibrated photodiode can be mounted on the front port which is important for calibration purposes. The amount of light reaching the SiPM behind the aperture is much smaller than the amount of light reaching the calibrated sensor. For this reason the power ratio between the two ports was measured as a function of the wavelength by covering both ports with a calibrated sensor. Considering this ratio, the number of photons hitting the SiPM behind the aperture can be determined from the light power measured at the upper port with the calibrated photodiode.

Sensor Positioning

The SiPM is placed in a $11 \times 6 \times 3 \text{ cm}^3$ metal box (see figure 3.10), similar to the one described in section 3.2. It has a 6 mm and a 8 mm hole on the top where two sensors with different packages can be placed. The distance from the the sensor to the surface of the top cover can be adjusted with four screws which allow to move the circuit board the sensor is mounted on (see right side of figure 3.10). In this way the SiPM can be moved just above the surface of the top cover. The box is mounted on a positioning stage which is used to align the sensor in front of the aperture. It can be moved in z-direction along an optical bench until the SiPM touches the aperture. The positioning stage now can be used to align the SiPM in front of the aperture in the x-y-plane. The positioning procedure is described in detail in chapter 4.6.

Sensitivity Measurement

A Xenon lamp which provides a highly stable irradiance in the wavelength region from 300 nm up to 1400 nm is used as a light source to measure the spectral sensitivity of the SiPM in a wide spectral range. A monochromator is used to select a small wavelength interval with a width of $\approx 2 \text{ nm}$ out of the continuous spectrum of the Xenon lamp in order to measure the sensitivity as a function of wavelength. The monochromator basically consists of a grating which spatially separates the incident light according to its wavelength. The diffractive pattern is projected onto an exit slit allowing only the first grating order $m = 1$ of a wavelength λ_1 to exit. However, the grating equation for constructive interference is also satisfied for wavelength λ_m in higher grating order ($\lambda_m = \lambda_1/m$, m being integer). In order to eliminate the higher order wavelength, additional optical filters with a cutoff wavelength of 305 nm, 400 nm, 530 nm, and 645 nm are placed on a filter wheel behind the monochromator. The optical filters are connected to the integrating sphere and the monochromator with two custom built adapters (see figure 3.9). The inner diameter of 14 mm of the adapters matches the diameter of the optical filters.

A picoamperemeter¹⁴ is used to measure the photocurrent of the SiPM which is associated to the number of detected photons. The ratio between the SiPM photocurrent and the optical

¹³National Institute of Standards and Technology

¹⁴Keithley Model 6487

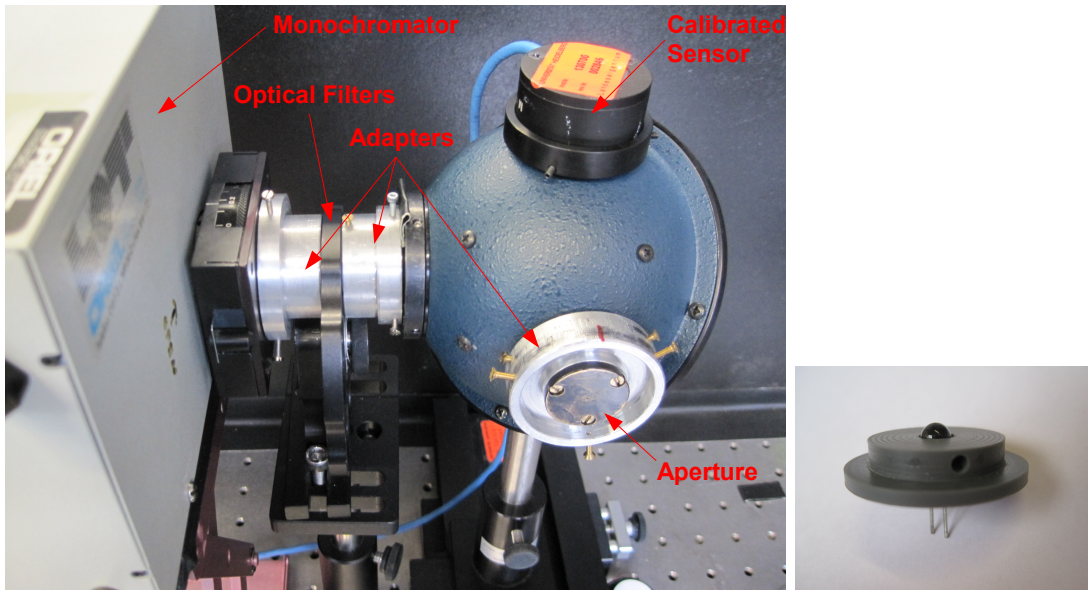


Figure 3.9: **Left:** Picture of the integrating sphere with the calibrated photodiode on the upper port. Two custom built adapters connect the sphere to an optical filter wheel and a monochromator. The SiPM is placed in front of the aperture attached to the front port of the sphere. **Right:** Custom built adapter used to mount LEDs and laser diodes on the entrance port of the integrating sphere.

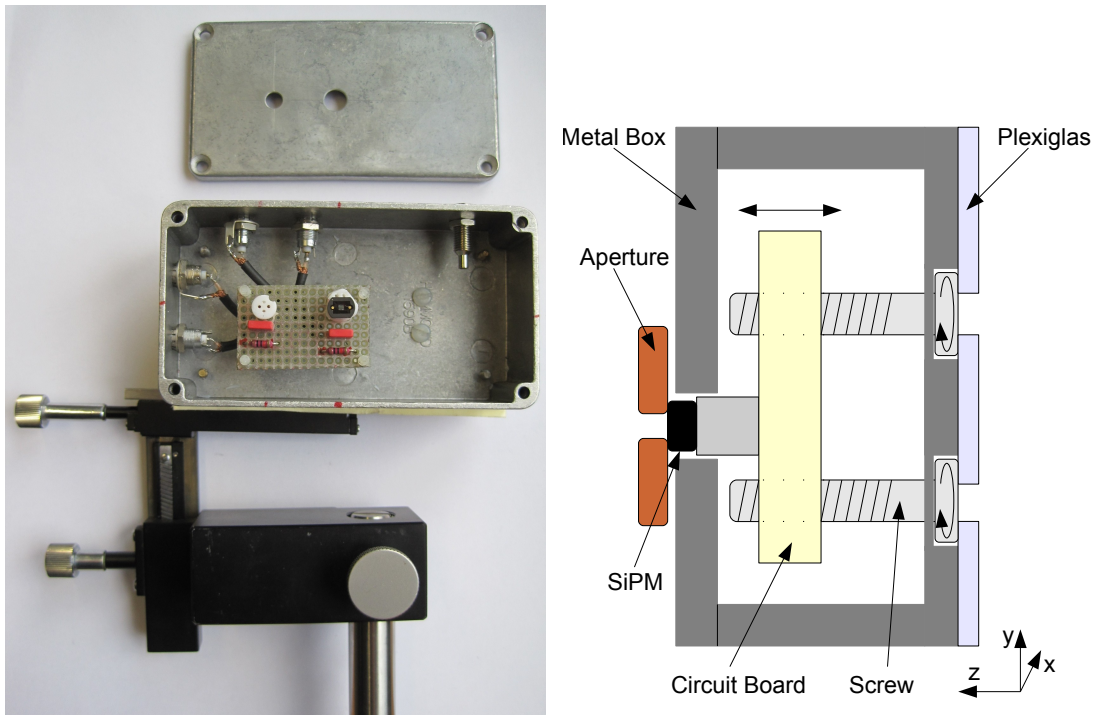


Figure 3.10: **Left:** Picture of the metal box containing two operation circuits with different sensor fixtures allowing to mount SiPM with different sensor packages. The box is mounted on a positioning stage which can be used to align the SiPM in front of the aperture in the x-y plane. **Right:** Schematic view of the metal box. The circuit board is mounted on four plastic screws allowing to adjust the sensor position in z-direction. In this way the sensor can be moved directly to the surface of the aperture.

power measured with the calibrated sensor on the other port is therefore associated with the sensitivity of the sensor. However, the photocurrent contains contributions from dark-rate, cross-talk and after-pulse events, and hence the number of fired pixels which is associated with the relative sensitivity of the sensor is larger than the actual number of detected photons associated with the PDE.

PDE Measurement

The measurement of the PDE without the effects of dark-rate, cross-talk and after-pulses is a new feature of the test stand. For this measurement the Xenon lamp and the monochromator are replaced by a laser diode which is driven by a pulse generator (see figure 3.8). The laser diode is attached directly to the entrance port of the integrating sphere with a custom built adapter shown in figure 3.9. The pulsed illumination allows readout the SiPM with a QDC as discussed in chapter 3.2. The resulting charge spectrum provides information about the number of detected photons without cross-talk and after-pulses and can also be corrected for dark-rate events. This analysis is discussed in detail in chapter 4.1. Unlike the measurement with the Xenon lamp which can be done over a wide spectral range, the pulsed measurement can only be executed for the wavelengths of the available laser diodes. However, the two methods can be combined by normalizing the values for the spectral sensitivity to the PDE values at the corresponding wavelength. In this way the PDE can be determined for the whole spectral range from 300 nm to 1000 nm.

3.6 Sensor Scans

The setup presented in this section can be used to determine the response of individual pixels of a sensor. This allows to study the uniformity of the device in terms of spatial variations of the sensitivity, gain and cross-talk which contribute to the excess noise of a sensor. Figures 3.11 and 3.12 show a picture and a schematic view of the experimental setup which allows to measure the sensitivity, gain and cross-talk probability of the individual pixels. The principle of this measurement is to scan the sensor with a small light spot. For this purpose a metal box containing the SiPM and the circuit board is mounted on a micrometer positioning stage. The SiPM is located directly behind a 2 mm opening in the front side of the box. A laser diode driven by a pulse generator is used to generate light pulses with a length of a few nanoseconds. A beam splitter equally distributes the light to a photodiode used to monitor the light intensity and a spatial filter. The spatial filter is a combination of two microscope objectives and a $\varnothing 5\mu\text{m}$ pinhole which produces a light spot with a Gaussian intensity profile. The light spot is focused on the sensor with a third microscope objective. The positioning stage is controlled with the computer allowing to automatically scan the sensor in the x-y plane. The SiPM is read out with a QDC (see chapter 3.2) allowing to determine the gain, cross-talk and the number of detected photons for every position of the light spot. In this way, the response of the individual pixels can be studied and compared.

The measurement is controlled by a LabVIEW program which automatically scans the sensor in a predefined area with a certain step width (typically a few micron). A charge spectrum with 10^4 entries is recorded for every geometrical position in the x-y plane. The data is analyzed with a ROOT program, which calculates the sensitivity, gain and cross-talk probability for every position of the light spot and creates a 2D map of the properties by combining all measurement

points. These maps can be used to characterize the uniformity of the device and to determine the geometrical fill factor of the sensor.

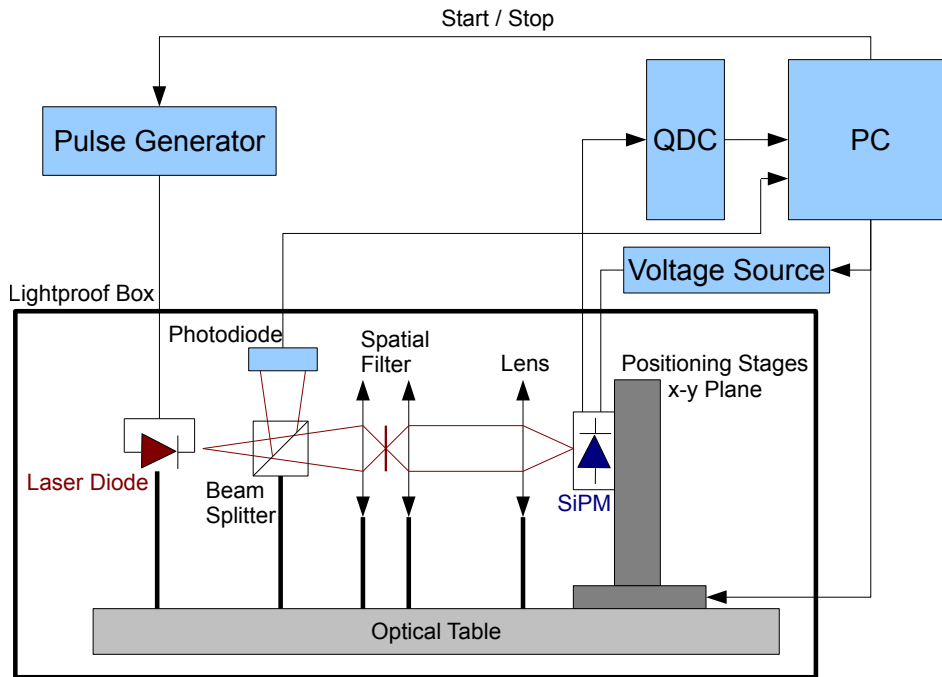


Figure 3.11: Schematic view of the experimental setup used for the uniformity measurements. The SiPM is scanned with a small light spot.

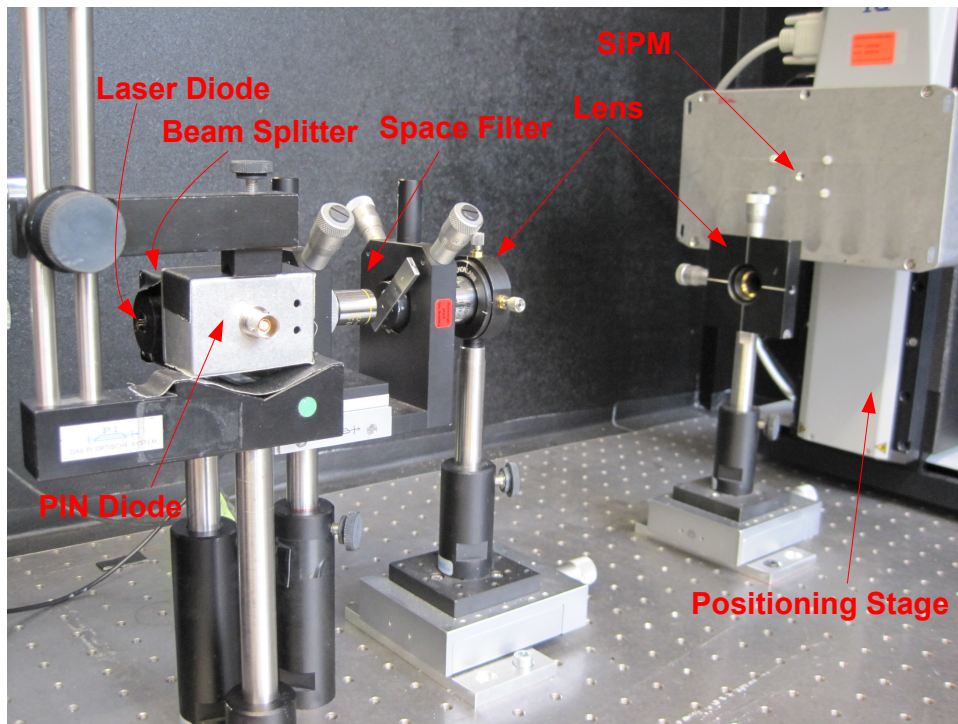


Figure 3.12: Picture of the sensor scan setup. The SiPM is placed inside a metal box behind a 2 mm opening.

Chapter 4

SiPM Characterization

In this thesis several HAMAMATSU MPPCs and SensL SiPMs have been characterized and compared. Table 4.1 shows the basic parameters of the tested sensors. In the following sections the results of the gain, dark-rate, cross-talk, after-pulse, PDE and uniformity measurements are presented.

Parameter	HAMAMATSU S10362-11			SensL SPMMicro 1020X13	Unit
	-25C	-50C	-100C		
Active area	1×1				mm ²
Number of pixels	1600	400	100	848	-
Pixel size	25 × 25	50 × 50	100 × 100	≈ 30 × 30	μm ²
Fill factor	30.8	61.5	78.5	33.9	%
Operating voltage	Typ. 70			Typ. 30	V
Spectral response range	320 to 900			400 to 1100	nm
Doping structure	p-on-n			n-on-p	-

Table 4.1: Basic parameters of the tested sensors [29] [30].

4.1 Gain Measurements

Single Photoelectron Spectrum

Figure 4.1 shows a typical integrated charge spectrum measured with the setup described in chapter 3.2. Each peak in the spectrum corresponds to a certain number of photoelectrons (p.e.). The first peak (0 p.e.) contains all the events where no photon was detected and is referred to as “pedestal” peak. The second peak (1 p.e.) corresponds to the signal of one detected photon, and so forth. The clear separation of the individual peaks shows the excellent single photon resolution which can be achieved due to a very low excess noise factor resulting from the Geiger mode operation and a high uniformity in the response of the individual pixels. This is not the case for a PMT or an APD where the linear amplification process leads to large statistical fluctuations. The peaks are in good approximation Gaussian shaped. For a larger number of firing pixels the peak width increases since the statistical fluctuations in the avalanche process of the individual pixels add up (see equation 2.9). After-pulses which occur at the end of the integration period are only partially integrated and therefore only a fraction of their charge is measured. This effect is more important for sensors with a long signal decay time and results in a small asymmetric tail of the Gaussian shape to the left side of the peak.

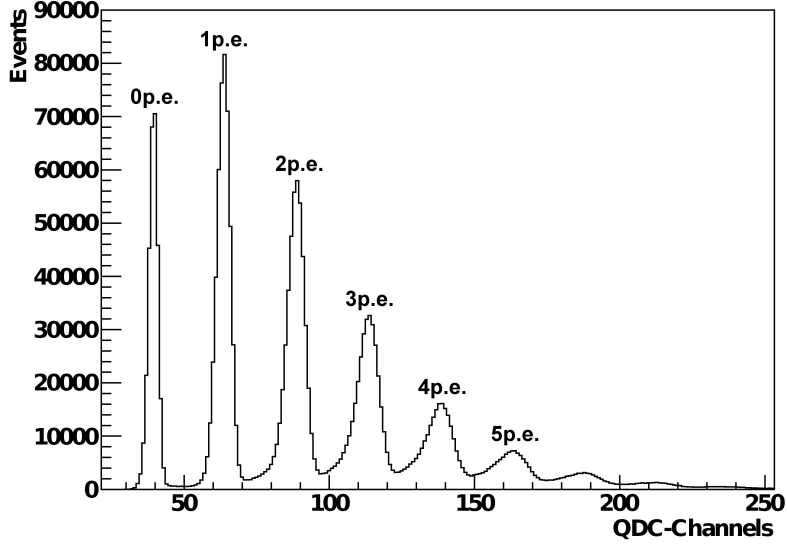


Figure 4.1: Typical integrated charge spectrum for a fixed bias voltage recorded with a MPPC S10362-11-050C. Every peak corresponds to a certain number of pixels fired; e.g. 0 p.e.: 0 pixels fired (pedestal), 1 p.e.: 1 pixel fired, etc.

The distance between two neighboring peaks corresponds to the gain of the SiPM since it indicates the amount of charge produced in an avalanche breakdown of one individual pixel. The gain measurements are discussed in detail in the next section. For low photon fluxes the number of photons arriving at the sensor is Poisson distributed. For this reason the number of detected photons is expected also to be Poisson distributed. The probability to detect a certain number of photons n therefore is given by:

$$P(n, \lambda) = \frac{\lambda^n}{n!} \cdot e^{-\lambda}$$

with λ being the mean value of the Poisson distribution. This probability can be determined from the number of events in the n -th peak of the charge spectrum divided by the total number of events. However, there are three effects which cause a deviation from the ideal Poisson distribution:

- **Cross-talk & after-pulses:** If a pixel fires, there is a certain probability to have a second pulse due to cross-talk or after-pulsing. For this reason one, detected photon can cause two or even more pulses. This effect causes events which correspond to a certain number of detected photons to occur in the next higher peak in the charge spectrum which causes a deviation from the Poisson distribution. However, the number of events in the pedestal is not influenced by this effect since there is no pixel which fired and consequently could trigger a cross-talk or after-pulses event. It should be noted that cross-talk and after-pulse events have the same effect on the charge spectrum and therefore cannot be distinguished with this method.
- **Thermal noise:** Thermal pulses also contribute to the charge spectrum and cause a deviation from the Poisson distribution. Considering a typical dark-rate of 500 kHz and a

typical integration gate of 100 ns, the probability to record a dark-rate event is $500 \text{ kHz} \cdot 100 \text{ ns} = 5\%$. Like cross-talk and after-pulse events, a thermal pulse causes an event to appear in the next higher peak in the charge spectrum with respect to the actual number of detected photons. This effect also influences the number of events in the pedestal in contrast to cross-talk and after-pulsing.

Number of Detected Photons

The parameter λ of the Poisson distribution refers to the expectation value of the distribution and hence corresponds to the mean number of detected photons $\langle N_{p.e.} \rangle$. The parameter λ can be determined by measuring the probability for detecting no photons:

$$P(0, \lambda) = \frac{0^\lambda}{\lambda!} \cdot e^{-\lambda} = e^{-\lambda}$$

This probability $P(0, \lambda)$ is given by the number of events $N_{0p.e.}$ contained in the pedestal peak divided by the total number of recorded events N . The mean number of detected photons therefore is given by:

$$\lambda = -\ln\left(\frac{N_{0p.e.}}{N}\right)$$

Only the number of pedestal events and the total number of events enter the calculation and since both numbers are not influenced by cross-talk and after-pulses, λ reflects the mean value of detected photons without the effects of cross-talk and after-pulsing. However, thermal pulses influence the number of events in the pedestal which hence has to be corrected for this effect. This correction can be determined by recording a dark-rate charge spectrum which is shown in figure 4.2.

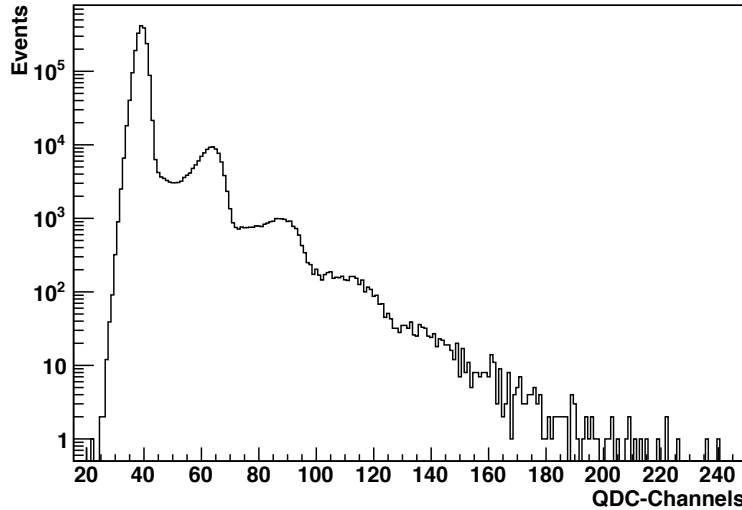


Figure 4.2: Typical dark-rate spectrum recorded with a MPPC S10362-11-050C. All peaks besides the pedestal are caused by dark-rate events.

In a typical dark-rate charge spectrum the majority of events are contained in the pedestal peak since the probability to detect a dark-rate event within the integration gate is small ($\approx 5\%$).

All events with a charge value above the pedestal value can be identified as dark-rate events. A correction factor α is introduced to rescale the number of events in the pedestal $N_{0p.e.}^{dr}$. The corrected number of pedestal events $N_{0p.e.,c}^{dr}$ in the dark-rate spectrum equals the total number of events N^{dr} :

$$\alpha \cdot N_{0p.e.}^{dr} = N_{0p.e.,c}^{dr} \stackrel{!}{=} N^{dr} \Rightarrow \alpha = \frac{N^{dr}}{N_{0p.e.}^{dr}} \quad (4.1)$$

The factor $\alpha - 1$ corresponds to the probability for a dark-noise event to occur during the charge integration. Applying the correction factor to the pedestal of the spectrum of the illuminated measurement, the mean number of detected photons without cross-talk, after-pulse and dark-rate effects can be determined:

$$\langle N_{p.e.} \rangle = \lambda_c = -\ln\left(\frac{\alpha \cdot N_{0p.e.}}{N}\right) \quad (4.2)$$

The mean value of the charge spectrum Q_{mean} is associated with the mean value of fired pixels $\langle N_{pix} \rangle$ and contains cross-talk, after-pulse and dark-rate events. $\langle N_{pix} \rangle$ is defined by the following equation:

$$\langle N_{pix} \rangle = (Q_{mean} - Q_{pedestal})/G \quad (4.3)$$

with G representing the gain and $Q_{pedestal}$ the charge value of the pedestal.

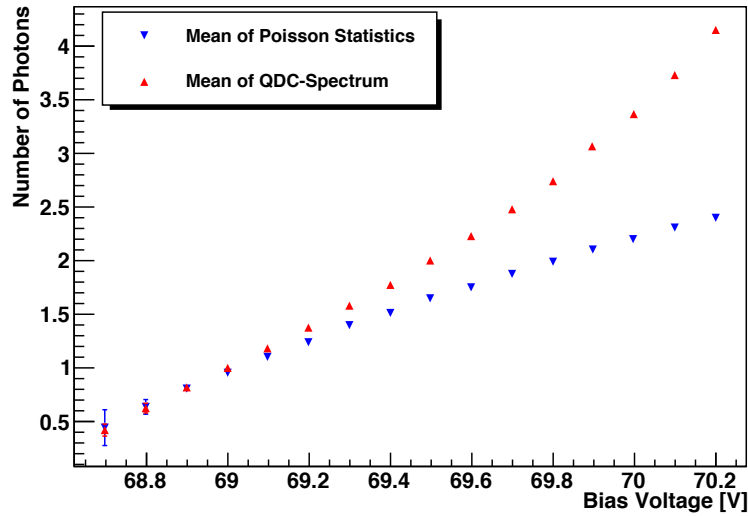


Figure 4.3: Number of detected photons with ($\langle N_{pix} \rangle$, red) and without ($\langle N_{p.e.} \rangle$, blue) cross-talk & after-pulses (MPPC10362-11-050C). In this figure $\langle N_{pix} \rangle$ is not corrected for the dark-noise to illustrate the effect of cross-talk and after-pulses only.

Figure 4.3 shows the values $\langle N_{p.e.} \rangle$ and $\langle N_{pix} \rangle$ for the MPPC S10362-11-050C at different bias voltages. For low bias voltages, the effects of cross-talk, after-pulse and dark-rate are small and therefore the values for $\langle N_{p.e.} \rangle$ and $\langle N_{pix} \rangle$ are nearly identical. For higher bias voltages, the number of cross-talk, after-pulse and dark-rate events is significantly larger. These effects are discussed in detail in the following sections.

Gain

The gain of a sensor corresponds to the charge difference between two neighboring peaks in the charge spectrum. A convenient way to determine this difference is to calculate the frequency spectrum of the charge spectrum (see figure 4.4) by applying a *Fast Fourier Transformation* (FFT).

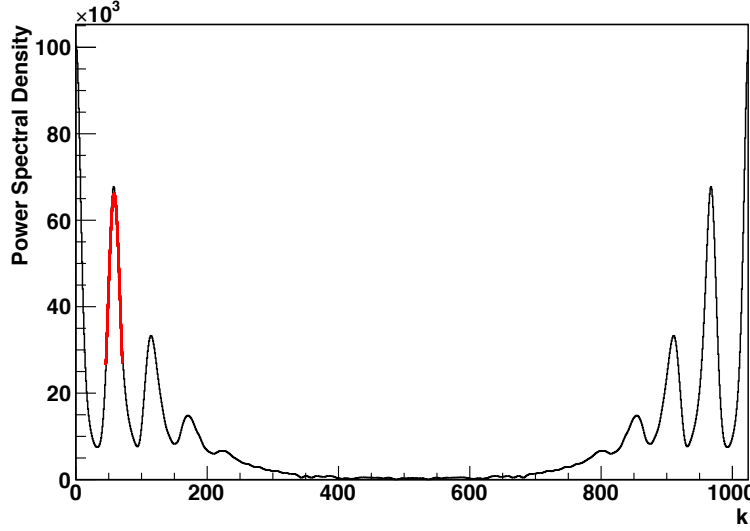


Figure 4.4: Power spectral density of a typical charge spectrum obtained by applying a Fast Fourier Transformation. A Gaussian function (red curve) is fitted to the first peak whose position is connected to the gain.

The FFT is a discrete Fourier transformation which transforms a sequence of N (in general complex) numbers x_0, \dots, x_{N-1} into a sequence of N complex numbers X_0, \dots, X_{N-1} according to the following formula:

$$X_k = \sum_{n=0}^{N-1} x_n e^{-\frac{2\pi i}{N} kn} \quad k = 0, \dots, N-1 \quad (4.4)$$

If the FFT is applied to the charge spectrum, x_0, \dots, x_{N-1} represent the bin values in the spectrum and $N = 1024$ is the maximum QDC value. Evaluating the expression in 4.4 for all integers k instead of just for $k = 0, \dots, N-1$, this results in an infinite periodic sequence with period N : $X_k = X_{k+N}$. If the x_k are real numbers (which is the case for the charge spectrum) this leads to: $X_{N-k} = X_{-k} = X_k^*$. Consequently, for the real and imaginary part follows:

$$\text{Re}(X_k) = \text{Re}(X_{N-k}) \quad (4.5)$$

$$\text{Im}(X_k) = -\text{Im}(X_{N-k}) \quad (4.6)$$

The power spectral density (PSD) of a sequence of numbers is defined as $PSD(k) = X_k \cdot X_k^*$. For a real sequence of numbers x_k the PSD shows a left/right symmetry (see figure 4.4) which is explained by relation 4.5 and 4.6. Assuming a simplified charge spectrum with only two nonzero entries x_m and x_l , the PSD is given by:

$$PSD(k) = (x_m e^{-\frac{2\pi i}{1024} km} + x_l e^{-\frac{2\pi i}{1024} kl}) \cdot (x_m e^{\frac{2\pi i}{1024} km} + x_l e^{\frac{2\pi i}{1024} kl}) \quad (4.7)$$

Simplifying this term, it can be shown that the PSD is given by:

$$2x_m x_l \cdot \cos\left(\frac{x_l - x_m}{1024} 2\pi k\right) + x_m^2 + x_l^2 \quad (4.8)$$

The period of this PSD is given by $1024/(x_l - x_m)$ and therefore connected with the gain $G = x_l - x_m$.

Figure 4.4 shows the square root of the power spectral density of a recorded charge spectrum. It shows the same periodicity as the PSD in equation 4.7. The amplitude of the peaks changes due to the Gaussian shape of the peaks in the charge spectrum. However, this is not important for the gain analysis and will therefore not be discussed in detail. According to equation 4.8 the gain of the sensor is associated with the period of the PSD which is determined by the position k_{1peak} of the first peak:

$$G_{QDC-Channels} = 1024/k_{1peak} \quad (4.9)$$

The gain value is converted from the ‘‘QDC-Channel’’ unit to the unit of elementary charge q_e by multiplication with the following conversion factor:

$$\frac{G_{q_e}}{G_{QDC-Channels}} = \frac{0.25 \cdot 10^{-12} C}{50 \cdot q_e} = 31211$$

The 0.25 pC is the resolution of the QDC (i.e. the charge per channel) and the factor 50 takes into account the signal preamplification factor.

The setup described in chapter 3.2 was used to automatically record charge spectra with 10^5 samples in a predefined range for the bias voltage at a temperature of 25 ± 0.1 °C. An analysis program was designed in ROOT which applies a FFT to the spectra and fits the first peak of the PSDs. From this peak position the gain is calculated according to equation 4.9 and plotted as a function of the bias voltage. The breakdown voltage U_{break} and pixel capacitance C_{pixel} are determined by fitting the data to the formula 2.5:

$$G = \frac{C_{pixel}}{q_e} \cdot (U_{bias} - U_{break})$$

The results are shown in table 4.2. Figure 4.5 shows the results of the gain measurement for the different sensors as a function of the over-voltage. The results fit the expected linear dependence on the bias voltage described in equation 2.5. SiPMs with a larger pixel size have a higher gain which can be explained by the larger pixel capacitance. It can be seen that the variations in the gain between sensors of the same type, only differing in the production number, are small.

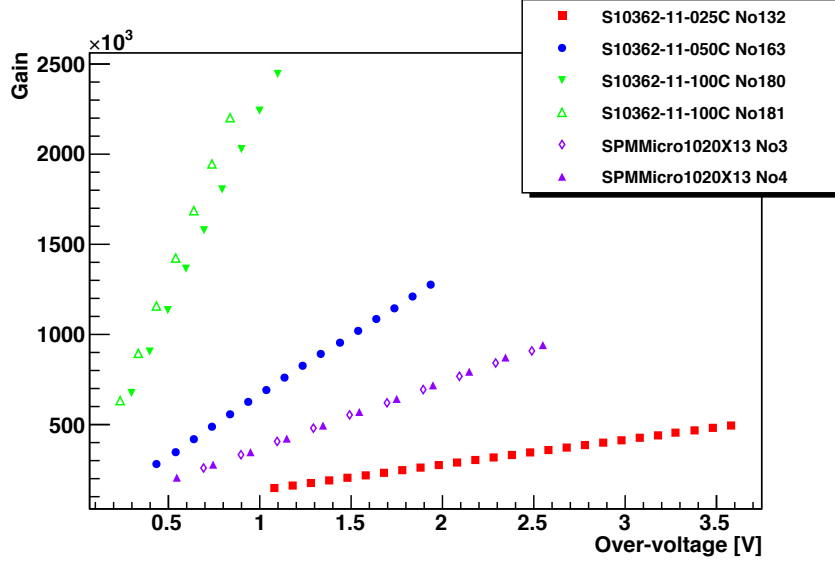


Figure 4.5: Gain of the different sensors as a function of the over-voltage. The number following the sensor type in the caption corresponds to the sample number of the device.

Device	U_{break} [V]	C_{pixel} [fF]
HAMAMATSU S10362-11-025C		
Sample 132	68.42 ± 0.19	22.202 ± 0.002
HAMAMATSU S10362-11-050C		
Sample 163	68.26 ± 0.16	105.70 ± 0.07
HAMAMATSU S10362-11-100C		
Sample 180	68.50 ± 0.13	360.8 ± 0.1
Sample 181	69.06 ± 0.13	423.6 ± 0.12
SensL SPMMicro1020X13		
Sample 3	27.70 ± 0.05	58.15 ± 0.02
Sample 4	27.85 ± 0.07	58.86 ± 0.05

Table 4.2: Breakdown voltage and pixel capacitance of the different detectors

4.2 Dark-Rate Measurement

The setup described in chapter 3.3 was used to measure the dark-rate for a sequence of increasing discrimination thresholds. Figure 4.6 shows a typical result of such a threshold scan for a fixed bias voltage. The curve shows the characteristic of a step function which demonstrates the

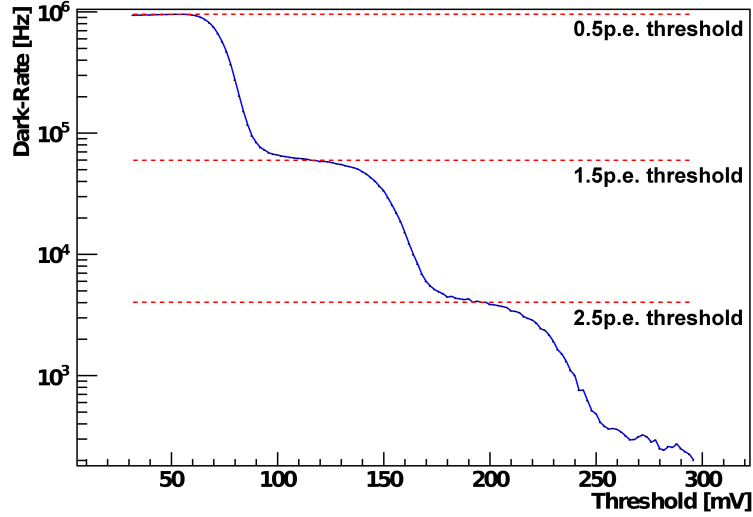


Figure 4.6: Typical results of a dark-rate measurement for a fixed bias voltage. The dotted red lines indicate the rates at 0.5 p.e., 1.5 p.e. and 2.5 p.e. threshold level.

high pulse height uniformity of the device. This leads to the excellent single photon separation which is also observed in the charge spectrum (see figure 4.1). For a threshold lower than the peak amplitude of the 1 p.e. signal, the rate is nearly constant. When the threshold exceeds the 1 p.e. level the rate drops significantly. Since the probability for two dark-rate pulses to occur in coincidence (i.e. within the typical signal width of ~ 10 ns) is negligible small ($< 1\%$) almost all 2 p.e. events are caused by cross-talk. This allows to determine the cross-talk probability which will be discussed in section 4.3.

In principle, the dark-rate can also be determined from the dark-rate charge spectrum (see figure 4.1). However, it is not possible to determine the cross-talk probability from the charge spectrum since cross-talk events cannot be distinguished from after-pulse events.

The dark-rate was measured as a function of the bias voltage. Figure 4.7 shows the results of the measurement for the different sensors at a temperature of 25 ± 0.1 °C. The dark-rate shown in the graph refers to the 0.5 p.e. threshold. The measured values are smaller than the actual values for the dark-rate due to the dead time of the scaler module of $\tau_{dead} = 10$ ns since pulses which occur within τ_{dead} after the preceding pulse are not detected. The measured rate can be corrected according to the following formula:

$$R_{real} = \frac{R}{1 - R \cdot \tau_{dead}}$$

where R is the measured dark-rate and R_{real} represents the real (corrected) value. However, this is a small correction ($\approx 0.5\%$) and can as well be neglected.

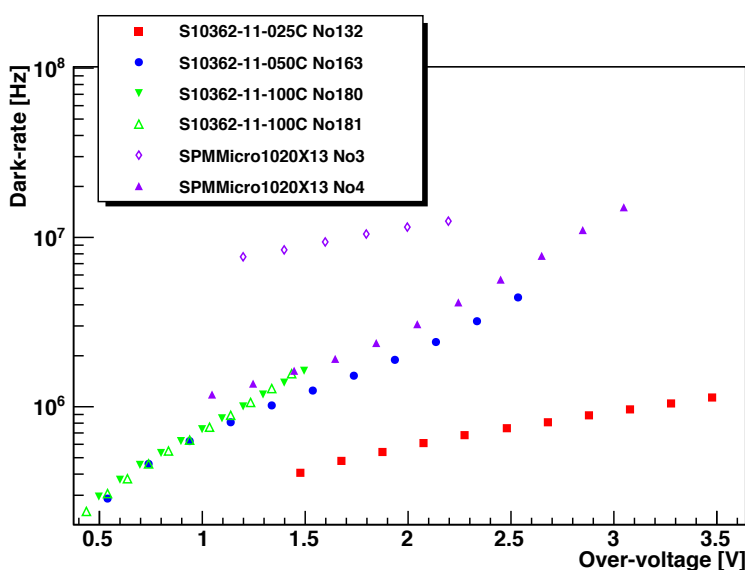


Figure 4.7: Measured dark-rate of the different sensors as a function of the over-voltage.

The dark-rate is generated by thermal and tunneling excitation of electrons in the active layer of the SiPM (see chapter 2.2). Figure 4.7 shows that the dark-rate increases with the over-voltage. This is due to the fact, that the probability for an electron to tunnel into the conduction band increases with the applied electrical field in the depletion region (see equation 2.10). Furthermore, the probability for a free charge carrier to trigger an avalanche breakdown increases with the bias voltage. The measurements show that the dark-rate of the HAMAMATSU MPPCs increases with the pixel size since the overall depletion region of the sensor increases. The SensL SiPMs have a much higher dark-rate than the MPPCs with respect to their pixel size. This can be explained by the different doping profile of the devices. The SensL SiPMs have a n-on-p doping structure which means that the depletion region consists of a thin n-layer on top of a thick p-layer. An avalanche breakdown can be triggered by an electron generated in the p-layer or a hole generated in the n-layer. The probability for an electron to trigger an avalanche breakdown is higher than for holes due to the larger impact ionization coefficient (see figure 2.6). For this reason, sensors with a n-on-p doping profile have in general a higher dark-rate compared to devices with p-on-n structure since latter have only a thin p-layer. The dark-rates of the two SensL SiPMs differ significantly, although the sensor are of the same type. This behavior cannot be explained at the moment and needs further investigation.

4.3 Crosstalk Measurements

Optical cross-talk is another source of noise which affects the precision of the photon-counting measurement. In section 4.1 a method is introduced to measure the number of photons without the effects of cross-talk. However, this method is based on a statistical analysis and cannot be applied to single measurements. Furthermore, the method can only be used for low photon fluxes since it requires to determine the number of events in the pedestal. In this section two methods are introduced to measure the cross-talk probability of a sensor.

Cross-talk Measurement using Threshold Scans

Considering a typical dark-rate of 500 kHz, the probability for two pixels to fire coincidentally (i.e. within the recovery time of typically 10 ns) due to thermal excitation is negligible small ($500 \text{ kHz} \cdot 10 \text{ ns} = 0.5\%$). The probability for an after-pulse to occur within the recovery time of the pixel is also small (see section 4.4). Furthermore, these after-pulses have a very small signal amplitude since the pixel is not fully recovered. For this reason, nearly all dark-rate events where at least two pixels fired must be caused by cross-talk. The cross-talk probability can therefore be defined as the ratio of the dark-rates corresponding to the 1.5 p.e. and 0.5 p.e. threshold:

$$P_{CT} = \frac{r_{1.5p.e.}}{r_{0.5p.e.}} \quad (4.10)$$

This ratio can be determined from the data of the dark-rate measurement described in chapter 4.2. The cross-talk probability defined in equation 4.10 represents the probability for one firing pixel to trigger at least one cross-talk event; i.e. it may even trigger two or more cross-talk events.

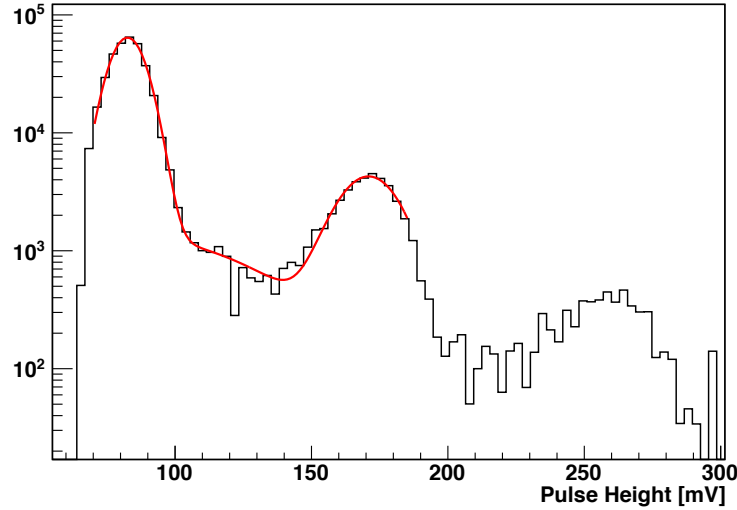


Figure 4.8: Pulse height spectrum (absolute value of the derivative of the threshold scan recorded with a S10362-11-050C) fitted with a function consisting out of three Gaussian functions (red curve).

A ROOT program was developed to automatically analyze the data from the threshold scans and calculate the cross-talk probability. The rate $r_{0.5p.e.}$ is determined by the first plateau in the threshold scan. The 1.5 p.e. threshold can be determined from the pulse height spectrum of the sensor (see figure 4.8) which is equivalent to the absolute value of the derivative of the threshold scan. The pulse height spectrum is calculated by deriving a spline function which is fitted to the threshold scan.

The 1.5 p.e. threshold can be defined in the middle of the 1 p.e. and 2 p.e. peak in the pulse height spectrum. However, for some sensors the peaks show an asymmetric tail to the right side. In this case this definition is not appropriate. For this reason, in this thesis the 1.5 p.e. threshold is defined at the minimum value between the 1 p.e. and 2 p.e. peak in the pulse height spectrum. This threshold corresponds to the rate with minimum gradient within the second plateau of the threshold scan. The next higher thresholds (2.5 p.e., 3.5 p.e., ...) are defined in

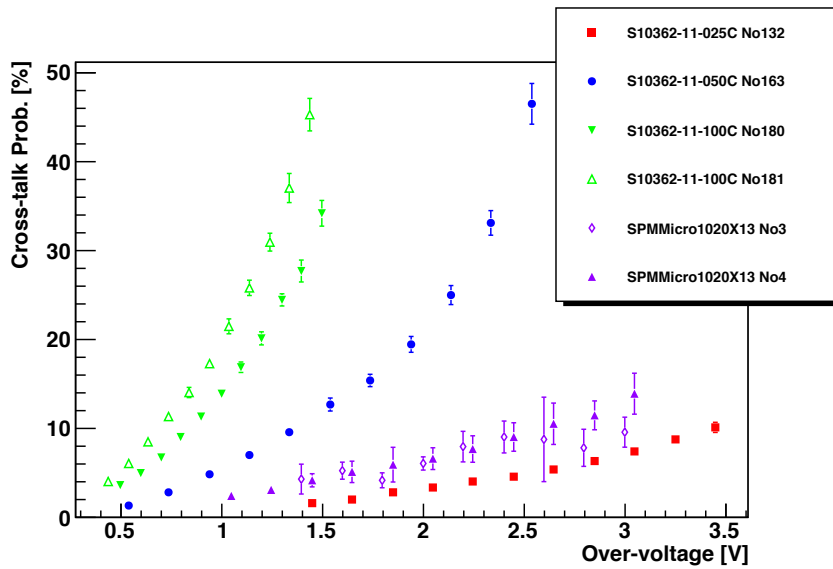


Figure 4.9: Measured cross-talk probability of the different sensor as a function of the over-voltage. Considering a fixed over-voltage, SiPMs with higher gain show a higher cross-talk probability.

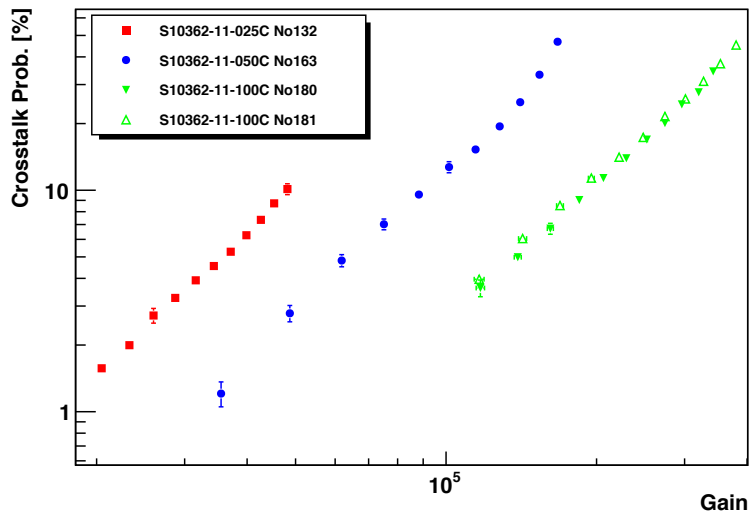


Figure 4.10: Measured cross-talk probability of the different sensor as a function of the gain. Considering a fixed gain SiPMs with smaller pixel size have a higher cross-talk probability.

the same way.

A method has been developed to automatically find the minima of the pulse height spectrum. Two adjoining peaks are fitted with a function consisting of three Gaussian functions - one for each peak and one for a possible asymmetric tail of the first peak. Figure 4.8 shows the result of such a fit. The fit quality in the region between the peaks is limited due to the simple fit function and therefore the minimum can only be determined with a limited precision. For this reason, the uncertainty of the fitted minimum was defined such, that the whole plateau region in the pulse height spectrum is covered. The minimum could be determined with higher precision by introducing a more sophisticated fit function. However, this is not necessary since the uncertainty in the position of the minimum only leads to a small uncertainty in the dark-rate for the corresponding discrimination threshold due to the approximately flat plateaus in the threshold scan. With the dark-rate corresponding to the 1.5 p.e. threshold obtained with this method the cross-talk probability can be determined according to equation 4.10.

Figure 4.9 shows the results of the cross-talk measurement for the different sensors as a function of the over-voltage at a temperature of $25 \pm 0.1^\circ\text{C}$. The gain of a sensor increases with the over-voltage (see figure 4.5) which also causes the cross-talk probability to increase since there are more electrons involved in the avalanche breakdown which can produce cross-talk photons. For this reason, sensors with higher gain (i.e. larger pixel size) have a higher cross-talk probability. Another effect which influences the cross-talk probability is the probability for a cross-talk photon to trigger an avalanche breakdown which also increases with the over-voltage. Figure 4.10 shows the cross-talk probability as a function of the gain. Considering a fixed gain, devices with smaller pixel size have a higher cross-talk probability since the mean distance from the avalanche to the neighboring pixels is smaller and therefore the probability for a cross-talk photon to reach an adjacent pixel is higher.

Cross-talk Measurement with a Focused Light Spot

The setup described in chapter 3.6 provides an alternative method to measure the cross-talk probability. In this setup, a focused light spot is used to illuminate a single pixel and charge spectra are recorded as a function of the bias voltage. The duration of the light pulses must be shorter than the recovery time of the pixel which is typically in the order of a few nanoseconds, in order to avoid that several photons are detected successively. For this purpose, a fast VSCL laser diode with a rise time of ≈ 1 ns was driven by a pulse generator generating voltage pulses with a width of ≈ 2 ns. With this setup only events with an integrated charge corresponding to 1 p.e. are expected since only one pixel is illuminated. All events with more than one pixel firing must therefore have a contribution from dark counts, cross-talk or after-pulses. The gate for the charge integration was set below the recovery time of a pixel. In this way the influence of after-pulse events is minimized and only cross-talk and dark-rate contribute to pulses with a charge value larger than the 1 p.e. events.

Figure 4.11 shows a typical charge spectrum obtained by single pixel illumination. The cross-talk probability is determined by the ratio of the number of events with a charge value larger than the 1 p.e. events and the total number of events with a charge larger than the pedestal value. However, these numbers have to be corrected for the dark-rate events first which can be done using a method similar to the one discussed in section 4.1. For this purpose, a dark-rate spectrum has to be recorded from which the correction factor α (see equation 4.1) can be

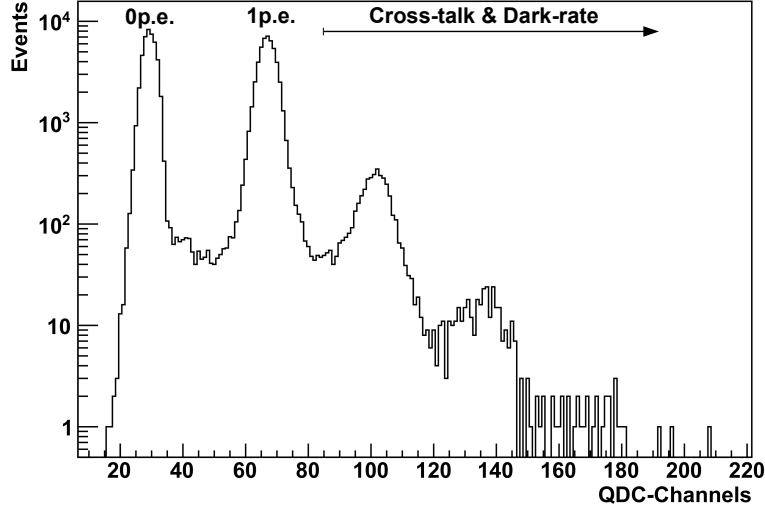


Figure 4.11: Charge spectrum recorded with a S10362-11-100C. Only a single pixel is illuminated. All events with a charge value larger than the 1 p.e. events have a contribution from cross-talk or dark-rate.

determined:

$$\alpha = \frac{N^{dr}}{N_{0pe}^{dr}}$$

where $\alpha - 1$ represents the probability for a dark-rate event to occur within the integration time. The number of events in the 1 p.e. peak ($N_{1p.e.}$) and the number of events with more than one pixel firing ($N_{>1p.e.}$) can be corrected for the dark-rate events according to the following formula:

$$\begin{aligned} N_{1p.e.,c} &= \alpha \cdot N_{1p.e.} \\ N_{>1p.e.,c} &= N_{>1p.e.} - (N_{1p.e.,c} - N_{1p.e.}) \\ &= N_{>1p.e.} - N_{1p.e.}(\alpha - 1) \end{aligned}$$

where $N_{1p.e.,c}$ represents the corrected number of 1 p.e. pulses (including all dark-rate events) and $N_{>1p.e.,c}$ represents the number of pulses with a charge larger than the 1 p.e. value without dark-rate events. The cross-talk probability therefore is defined as:

$$P_{CT}^{1pixel} = \frac{N_{>1p.e.,c}}{N_{1p.e.,c} + N_{>1p.e.,c}} \quad (4.11)$$

Figure 4.12 shows the results of this cross-talk measurement together with the results from the threshold scan measurements described in the previous section. The light spot was focused on the center of a pixel in the middle of the sensor.

The results of the two different methods agree quite well. However, there seem to be systematic deviation due to the completely different measurement concepts. One major difference between the two measurements is that the method described in this section is used to determine the cross-talk probability of a single pixel whereas the threshold scans only allow to determine the mean cross-talk probability considering all pixels. In section 4.7 it is shown that the cross-talk probability of the individual pixels is not uniform but depends significantly on the location of

the pixel. Another difference between the two methods is that in the measurement described in this section the pixel is illuminated, in contrast to the threshold scans, which may cause a deviation in the cross-talk probability. Despite this fundamental differences, the results of the two methods are comparable which validates the measurement concepts.

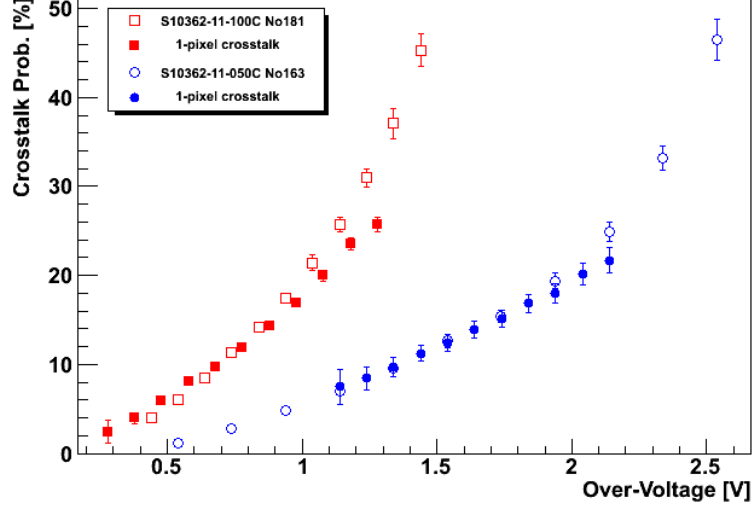


Figure 4.12: Cross-talk probability of a single pixel measured with a focused light spot. The cross-talk probability determined from the threshold scan measurement is also shown in order to compare the two methods.

4.4 After-pulse Measurement

The setup described in chapter 3.3 can be used to measure the time intervals between dark-rate pulses. The resulting histogram of the time intervals represents the time spectrum of the dark-rate which contains information about the after-pulse probability and the corresponding time constants. Figure 4.13 shows a typical results of such a measurement. The probability density $p(\Delta t)$ for a pulse to occur at a time Δt after the preceding pulse is described by equation 2.12. The time spectrum is equivalent to the probability density scaled with the total number of dark-rate events occurred during the measurement time.

$$N(\Delta t) = N^{tot} \cdot p(\Delta t)$$

Assuming only one type of trapping centers, the time spectrum can be described by the sum of two exponential functions (see chapter 2.2): one describing the contribution from thermal pulses (tp) and one describing the after-pulse component (ap):

$$N_{tp}(\Delta t) = \frac{N_{tp}^{tot}}{\tau_{tp}} \cdot e^{-\frac{\Delta t}{\tau_{tp}}} \quad (4.12)$$

$$N_{ap}(\Delta t) = \frac{N_{ap}^{tot}}{\tau_{ap_i}} \cdot e^{-\frac{\Delta t}{\tau_{ap_i}}} \quad (4.13)$$

$$N(\Delta t) = N_{tp}(\Delta t) + N_{ap}(\Delta t) \quad (4.14)$$

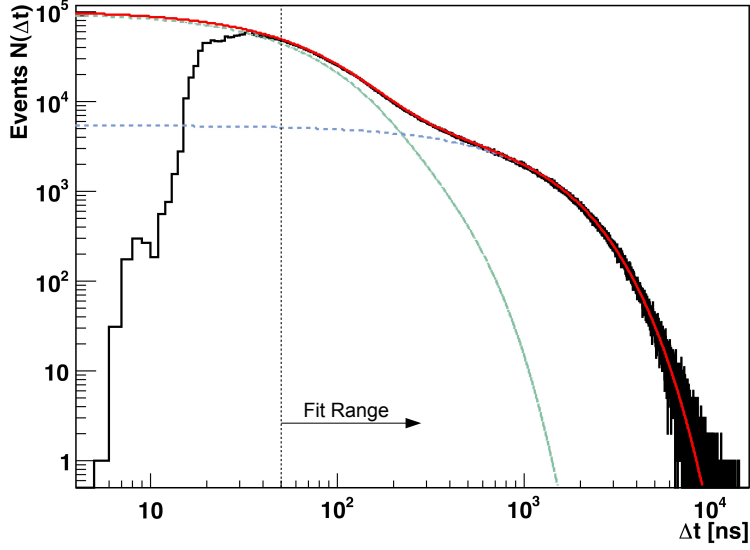


Figure 4.13: Histogram of the measured time intervals between two dark-noise pulses representing the time spectrum of dark-rate events. The spectrum was fitted using function 4.14 with two after-pulse components (red curve). The contributions from after-pulses (green curve) and thermal pulses (blue curve) can clearly be separated.

where $N_{ap,tp}^{tot}$ represents the total number of thermal- and after-pulse events and $\tau_{ap,tp}$ the corresponding time constants. The after-pulse probability can be defined as the ratio of the number of after-pulse events and the total number of dark-rate events:

$$P_{AP} = \frac{N_{ap}^{tot}}{N_{tp}^{tot} + N_{ap}^{tot}} \quad (4.15)$$

In general, there can be more than one after-pulse component corresponding to different types of trapping centers each with a characteristic trapping time. In this case equation 4.13 has to be replaced by the sum of all after-pulse components (see equation 2.12):

$$N(\Delta t) = N_{tp}(\Delta t) + \sum_i N_{ap_i}(\Delta t) \quad (4.16)$$

Time Spectrum Fit

The number of thermal- and after-pulse events $N_{ap,tp}^{tot}$ and the corresponding time constants $\tau_{ap,tp}$ can be determined by fitting the recorded time spectrum with the function 4.14. In figure 4.13 the result of such a fit and the individual contributions from thermal- and after-pulses are shown. Figure 4.14 shows the residuals of the fit using a fitting function with one and two after-pulse components, respectively. When applying a fit with only one after-pulse component a significant systematic deviation from the measured spectrum is observed for time intervals $< 10^3$ ns. The fit quality improves significantly by introducing a second after-pulse contribution, dividing the after-pulses in a slow and a fast component. This observation was also made in [25]. For this reason, in the following analysis a fitting function containing two

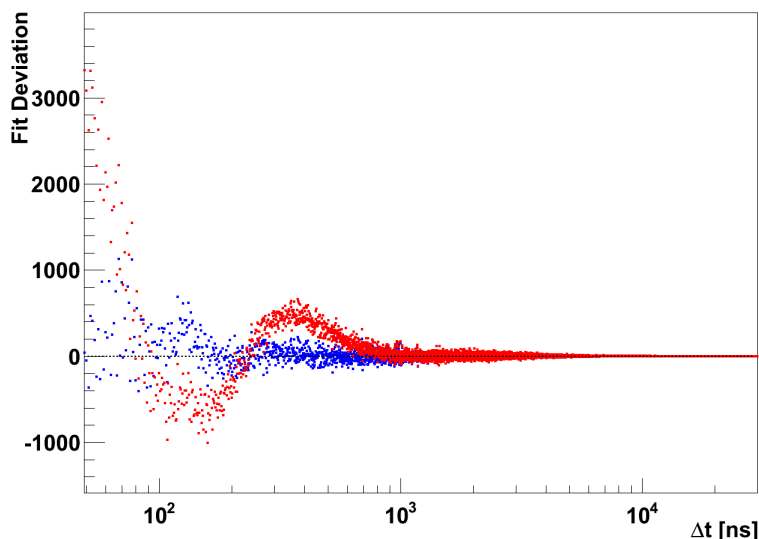


Figure 4.14: Residuals of the fit of the time spectrum 4.13 using a fitting function with one (red) and two (blue) after-pulse components, respectively. The fit is significantly improved introducing a second after-pulse component.

after-pulse components was used. The two different components could correspond to different trapping centers for electrons and holes.

Figure 4.13 shows that for short time intervals ($\Delta t < 50$ ns) the measured time spectrum is not described by the function 4.14. One reason for this is the dead time of the discriminator module and the TDC of 5 ns which limits the minimum time interval measurable. Furthermore, the minimum time between two detected pulses is limited by the width of the SiPM pulses. This effect is illustrated in figure 4.15. After-pulses can only be detected if the amplitude of the primary pulse has fallen below the discrimination threshold. In this case the leading edge of the after-pulse can cross the discrimination threshold and trigger an output pulse at the discriminator. If an after-pulse occurs before the amplitude of the primary pulse is below the

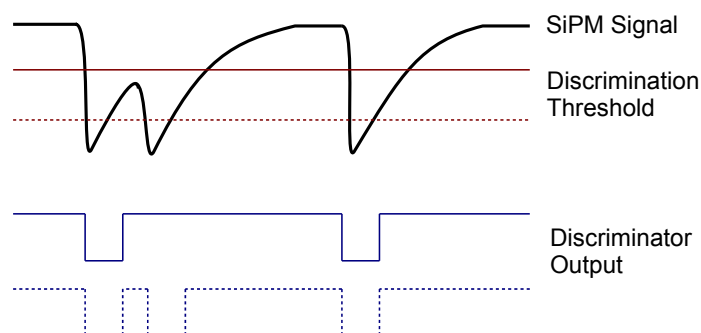


Figure 4.15: The minimum time interval measurable is determined by the time the SiPM pulse exceeds the discrimination threshold. Fast after-pulses can only be detected by applying a high discrimination threshold (dotted line).

discrimination threshold it is not detected. The minimum time interval measurable is therefore given by the time the SiPM pulse exceeds the threshold. Considering a typical pulse width of several tens of nanoseconds this effect explains the developing of the time spectrum for short time intervals. The minimum time interval measurable depends on the applied discrimination threshold and on the pulse width which depends on the sensor type and applied bias voltage. For this reason the fit range has to be adjusted for every recorded time spectrum in order to exclude the region in the spectrum where the measured time intervals are smaller than the pulse width.

The after-pulse probability can be determined according to equation 4.15 with the values for the total number of thermal- and after-pulses $N_{ap,tp}^{tot}$ determined by the fit. In this definition of the after-pulse probability the amount of charge contributed by the after-pulses is not considered. However, fast after-pulses which occur within the recovery time of the pixel have a smaller signal amplitude since the pixel is not fully recharged. In the following, an "effective" after-pulse probability is defined considering the amount of charge contributed by the after-pulse. The integrated charge of the pulse which occurs at a time Δt after the preceding pulse is described by the following formula [25] (see equation 2.6):

$$Q(\Delta t) = Q_0 \cdot (1 - e^{-\Delta t / \tau_{recovery}}) \quad (4.17)$$

where Q_0 is the charge delivered by a fully recharged pixel and $\tau_{recovery}$ is the recovery time. Table 4.3 shows the values for the recovery time of the HAMAMATSU MPPCs [31].

S10362-11	Recovery Time [ns]
-025C	≈ 4
-050C	≈ 9
-100C	≈ 33

Table 4.3: Recovery time of the HAMAMATSU MPPCs [31].

The total amount of charge from all thermal pulses and after-pulses, respectively, which are recorded in the time spectrum can be calculated according to the following formula:

$$Q_{tp,ap}^{tot} = \int_0^{\infty} N_{tp,ap}(\Delta t) \cdot Q(\Delta t) \cdot d\Delta t = Q_0 N_{tp,ap}^{tot} \cdot \frac{\tau_{tp,ap}}{\tau_{tp,ap} + \tau_r} \quad (4.18)$$

The "effective" after-pulse probability can be defined as the ratio of the total charge contributed by after-pulses and the total charge from all dark-rate pulses:

$$P_{AP}^{eff} = \frac{Q_{ap}^{tot}}{Q_{ap}^{tot} + Q_{tp}^{tot}} \quad (4.19)$$

Discrimination Threshold

The after-pulse measurements were done for a defined range of the bias voltage. Although the signal amplitude changes with the over-voltage, the discrimination threshold was kept constant for all measurements in order to reduce the complexity of the measurement. This is possible since the measured time constants and after-pulse probability should in principle not depend on the discrimination threshold. Only the minimum time measurable, which corresponds to

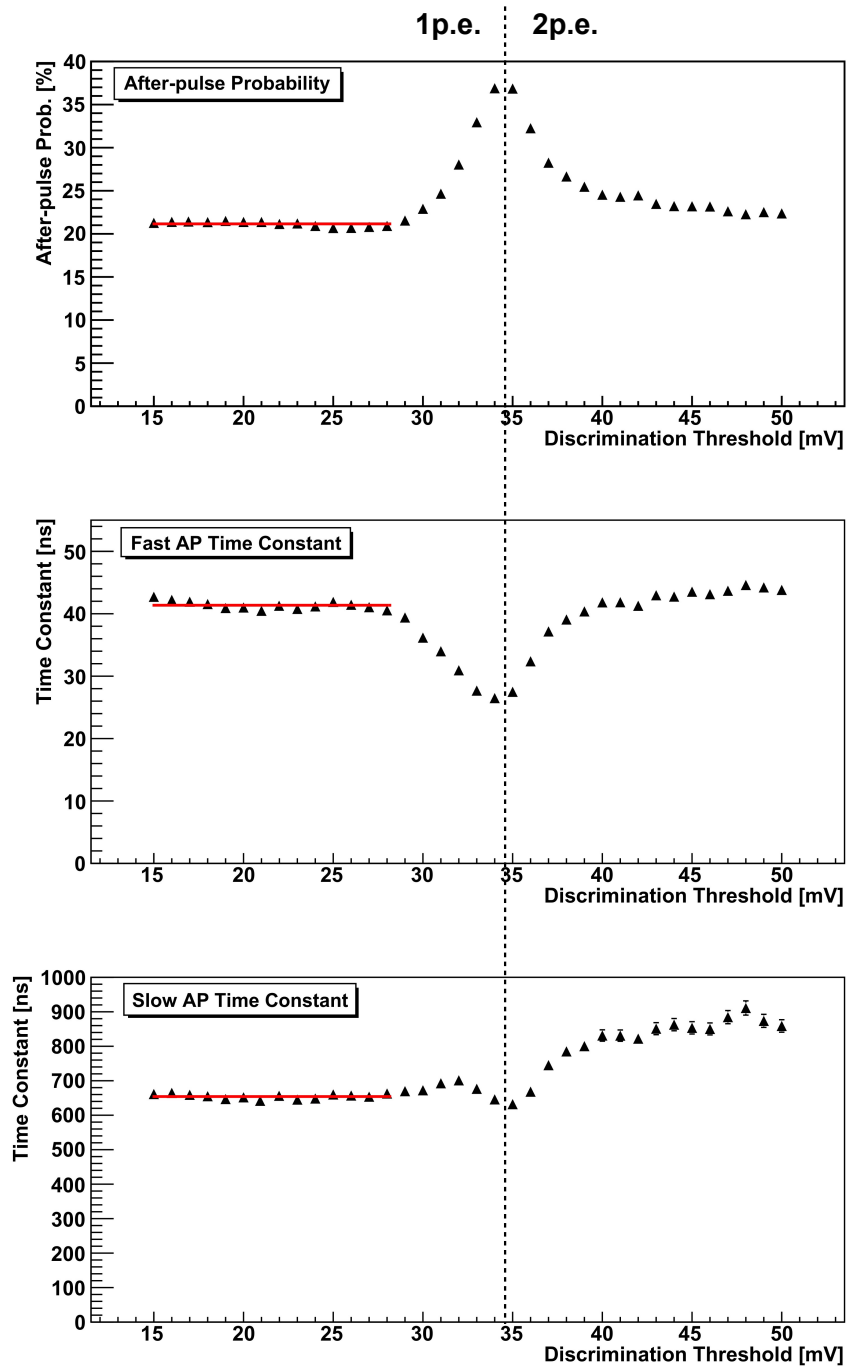


Figure 4.16: After-pulse probability and time constants as a function of the discrimination threshold measured with a S10362-11-050C MPPC. For thresholds well below the peak amplitude of the 1p.e. signal the parameters are constant (red fit). All measurements are done in this range.

the time the SiPM pulse exceeds the threshold, is affected (see figure 4.15). This was validated experimentally by recording time spectra at different discrimination thresholds for a fixed bias voltage in order to determine the time constants and after-pulse probability as a function of the applied discrimination threshold. The results shown in figure 4.16 confirm the assumption; i.e. the measured quantities are constant up to a threshold of ≈ 30 mV. For thresholds near the peak amplitude of the 1 p.e. signal (≈ 35 mV) the measured parameters change significantly. This behavior could possibly be explained by a third very fast after-pulse component which can only be accessed at thresholds near the peak amplitude of the 1 p.e. signal. This additional component would cause an increase in the after-pulse probability and reduce the time constant of the pulses. The slow component would not be affected by this effect. However, this hypothesis was not further investigated. For a sequence of after-pulse measurements, the discrimination threshold was consequently set to a value well below the peak amplitude of the 1 p.e. signals for all applied bias voltages.

Results of the After-pulse Measurement

The time spectra were automatically recorded for a certain range of the bias voltage specified in the LabVIEW program which controls the measurements and analyzed by a ROOT program which fits the spectra with the function 4.16 in order to determine the effective after-pulse probability according to equation 4.19 and the corresponding time constants. A fitting function with two after-pulse components was used (see above). The results of the measurements are shown in figure 4.17 and 4.18. The sensors show a strong increase in the after-pulse probability with increasing bias voltage and pixel size (see figure 4.17). This can be explained by the increasing gain and the increasing probability for a trapped charge carrier to trigger an avalanche breakdown. Since both effects depend approximately linearly on the over-voltage (see chapter 4.1 and 4.6) the after-pulse probability is expected to be proportional to V_{over}^2 [32]. This behavior is confirmed by a quadratic fit to the data which is also shown in figure 4.17.

Figure 4.18 shows the characteristic trapping time of the two after-pulses components which can be separated into a fast and slow component. The measured values for the time constants increase with the applied bias voltage which was also observed in [26]. However, in [25] the measured time constants seem to be independent of the bias voltage. This effect cannot be explained at the moment and needs further investigation.

The characteristic trapping times of the S10362-11-025C is below 100 ns. Considering a bunch crossing time at the ILC of ≈ 300 ns, the probability for an after-pulse to occur in a subsequent bunch crossing interval is small ($\approx 5\%$). In this respect the MPPC (especially the S10362-11-025C) is well suited for this application.

The time spectra measured for the SensL SiPMs can be described by the thermal pulse only and therefore no after-pulse probability could be determined. This is due to the fact that the signal of these SiPMs has a very long decay time and hence the measurement cannot access short time intervals where possible after-pulses could occur. The effective after-pulse probability of these devices can be assumed to be negligible small due to the long recovery time of the sensors which is connected to the signal decay time [31].

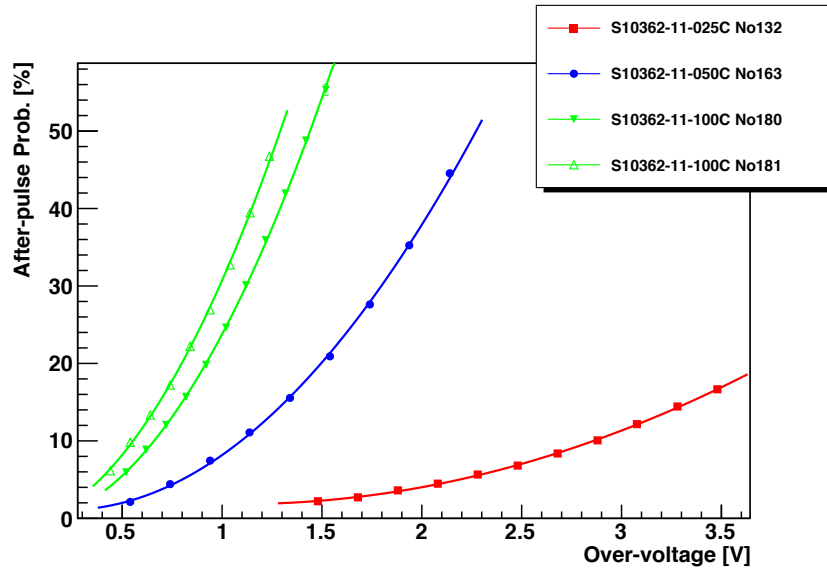


Figure 4.17: "Effective" after-pulses probability measured at a temperature of $25.0 \pm 0.1^\circ\text{C}$. The measured points are fitted by a function proportional to V_{over}^2 .

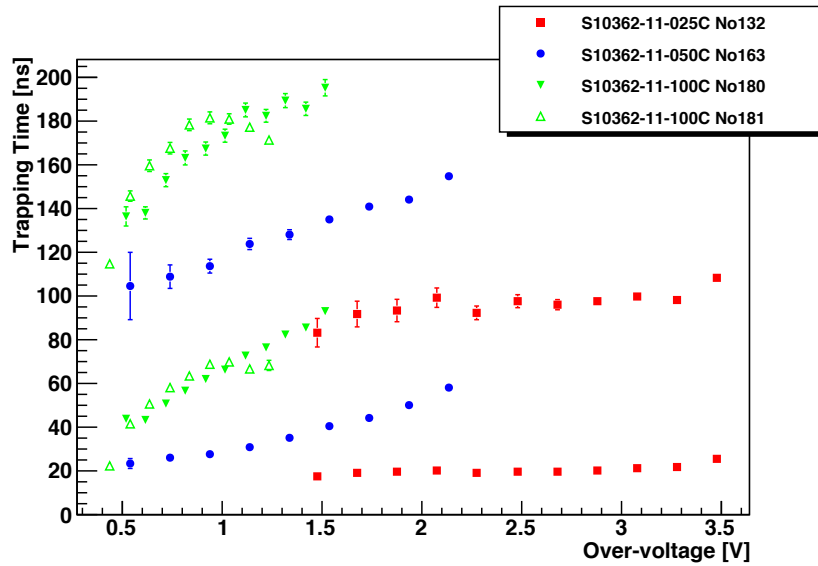


Figure 4.18: Measured time constants of the fast and slow after-pulse component.

4.5 Measurement of the Temperature Dependence

In most applications like particle detectors or PET, temperature fluctuation cannot be avoided. For this reason the test stand was equipped with a temperature chamber which allows to study the temperature dependence of the different parameters. The detailed setup is discussed in chapter 3.4.

A fundamental measurement is the temperature dependence of the breakdown voltage and the gain. The gain was measured with the setup described in chapter 3.2 in a temperature range from -10°C to 30°C with 4°C step size and the breakdown voltage was extrapolated from the gain-voltage curve. The measurement results shown in figure 4.19 show that the breakdown voltage increases linearly with rising temperature as expected [33, 29]. The temperature dependence of the breakdown voltage dV_{break}/dT was extracted from a linear fit. The results are shown in table 4.4. The measurement of this parameter is essential for the dark-rate, cross-talk and after-pulse measurement since the bias voltage has to be adjusted due to the changing temperature in order to keep the over-voltage constant.

Figure 4.20 shows the temperature dependence of the gain at a fixed bias voltage (69.00 V). The gain of a sensor with large pixel capacitance shows in general a stronger dependence on the over-voltage (see equation 2.5) and therefore on the temperature. A linear fit was applied to the measured curves in order to determine the temperature dependence of the gain dG/dT . The values for the two sensors (see table 4.4) differ significantly due to the different pixel capacitance of the devices. The gain of the MPPC with 1600 pixels can be assumed to have even a smaller temperature dependence.

The measurements of the temperature dependency of the dark-rate, cross-talk and after-pulses are similar to measurements described in chapter 4.2 to 4.4, however, the parameters are now measured as a function of the temperature at a fixed over-voltage. The bias voltage has to be adjusted for every measurement in order to keep the over-voltage constant since the break-down voltage changes with temperature:

$$V_{bias}(T) = V_{break}(T) + V_{over} \quad (4.20)$$

This is automatically done by the LabVIEW program which controls the measurements after entering $V_{break}(T)$ which has to be determined from the gain measurement. Figures 4.21 and 4.22 show the results of the dark-rate and cross-talk measurement for an over-voltage of 1 V. The strong temperature dependence of the dark-rate can be explained by the thermal energy of the electrons in the silicon. As shown in [34], the dark-rate decreases approximately exponentially with the temperature. The temperature dependence $1/D \cdot dD/dT$ (D represents the dark-rate) was extracted from an exponential fit. The resulting values for the two sensors are shown in table 4.4.

The cross-talk probability does not depend significantly on the temperature which is in agreement with [29]. The after-pulse probability shown in figure 4.23 shows a slight decrease with the temperature whereas the corresponding characteristic trapping times shown in figure 4.24 seem to be constant. However, temperature dependent trapping times are expected; i.e at low temperatures the trapping times should be longer because of the increasing trapping center de-excitation time [33, 35, 34]. For the tested devices, this temperature dependence can possibly be observed at very low temperatures due to the expected exponential behavior [34]. This could be tested by measurements at temperatures $< -10^\circ\text{C}$.

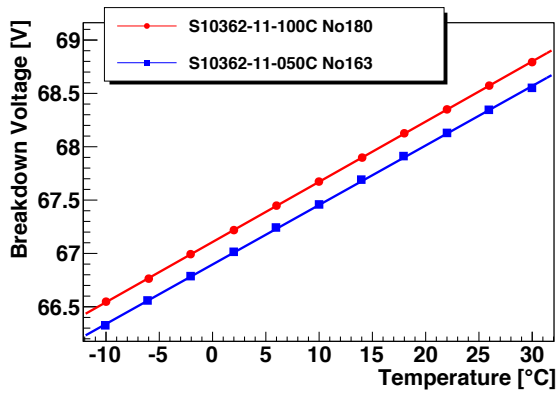


Figure 4.19: Breakdown voltage as a function of the temperature.

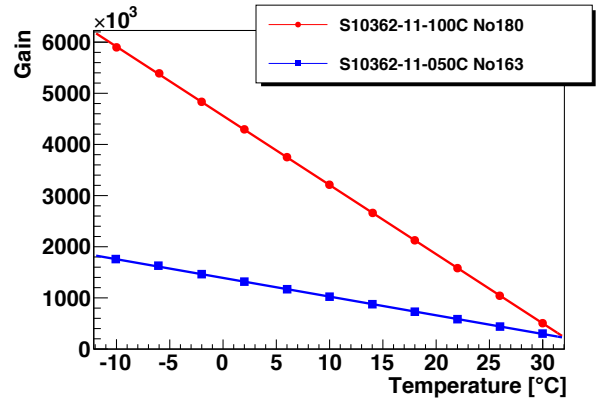


Figure 4.20: Gain as a function of the temperature.

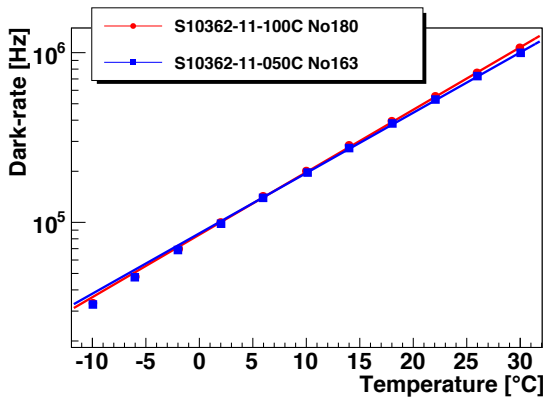


Figure 4.21: Dark-rate as a function of the temperature (1 V over-voltage).

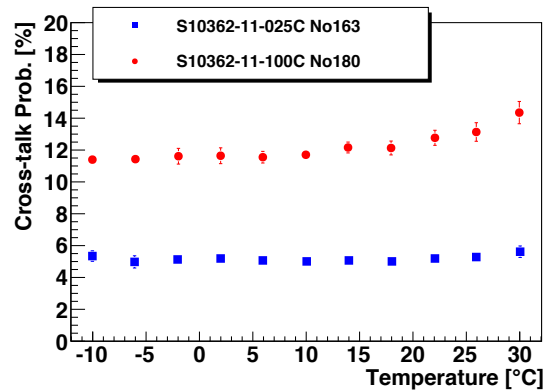


Figure 4.22: Cross-talk as a function of the temperature (1 V over-voltage).

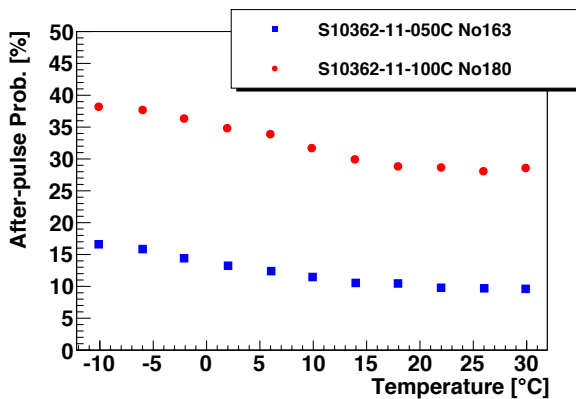


Figure 4.23: After-pulse probability as a function of the temperature (1 V over-voltage).

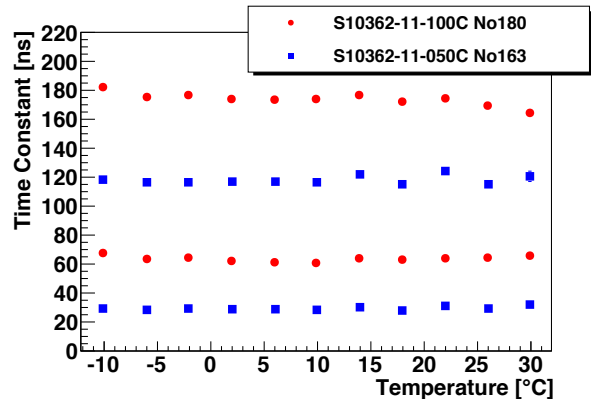


Figure 4.24: After-pulse trapping time constants as a function of the temperature (1 V over-voltage).

S10362-11	-050C No163	-100C No180	
dV_{break}/dT	55.7 ± 0.7	56.4 ± 0.5	mV/K
$-dG/dT$	36.5 ± 0.5	135.2 ± 1.1	$10^3/K$
$1/D \cdot dD/dT$	8.30 ± 0.10	8.53 ± 0.07	%/K

Table 4.4: Measured temperature dependence of the breakdown voltage, gain and dark-rate.

4.6 PDE Measurement

The photon detection efficiency is one of the most important parameters of SiPMs since it is the limiting factor for the photon-counting resolution (see section 4.8) and influences the sensitivity to small photon fluxes. The PDE measurement consists of two parts: a measurement of the relative spectral sensitivity in a wide spectral range from 350 nm to 1000 nm which, however, is influenced by dark-rate, cross-talk and after-pulses, and a measurement with a pulsed light source at a fixed wavelength which allows to determine the PDE without the effects of dark-rate, cross-talk and after-pulses. The relative sensitivity can be scaled with the PDE at the corresponding wavelength in order to determine the PDE in the whole spectral range of the relative measurement. The setups used for the two measurements are discussed in detail in chapter 3.5.

SiPM Positioning

The SiPM is located behind an aperture which is mounted on the front port of the integrating sphere in order to only illuminate the active area of the sensor. For the pulsed measurement an aperture with a diameter of $\varnothing 0.6$ mm is used, whereas for the relative measurement a $\varnothing 0.8$ mm aperture has to be used since the light intensity after the wavelength selection with the monochromator is too low to be measured with the calibrated photodiode using the $\varnothing 0.6$ mm aperture. For the PDE measurement it is essential that the aperture is fully covered by the sensor in order to only illuminate the active area of the SiPM. For this reason the SiPM is mounted on a positioning stage (see figure 3.10) which is used to adjust the sensor position in the x-y plane. The optimal position is found when the measured photocurrent of the SiPM is maximal. Figure 4.25 shows the photocurrent as a function of the sensor position in the x direction. In case of the $\varnothing 0.6$ mm aperture a plateau in the photocurrent of ≈ 0.35 mm can be observed. In this region the light spot is fully covered by the SiPM. For the PDE measurement the SiPM has to be located in this plateau region. Considering the dimensions of the active area of the sensor (1×1 mm²) the light spot has consequently a diameter of ≈ 0.65 mm. This is slightly larger than the diameter of the aperture due to a small opening angle of the light. For the $\varnothing 0.8$ mm aperture there is no clear plateau region in the photocurrent. For this reason the light spot must have a diameter of ≈ 1 mm or larger. There might consequently be a small intensity loss since the light spot is larger than the active area of the SiPM. However, this is not relevant since the $\varnothing 0.8$ mm aperture is only used for the relative sensitivity measurement.

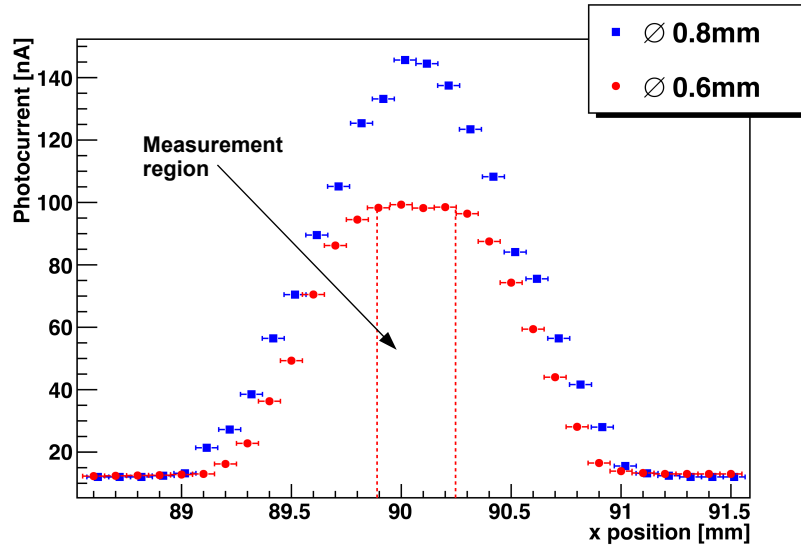


Figure 4.25: Photocurrent measured as a function of the sensor position. For the $\varnothing 0.6$ mm aperture (red) the diameter of the light spot is smaller than the active area of the SiPM which results in a plateau in the photocurrent. For the $\varnothing 0.8$ mm aperture (blue) no clear plateau region is observed.

Power Ratio of the Two Ports

The basic principle of the PDE measurement is to determine the response of the sensor to a referenced photon flux. The calibrated photodiode which is used to reference the light intensity is mounted directly on the top port of the integrating sphere. The amount of light reaching the photodiode is consequently much larger than the amount of light reaching the SiPM located behind the aperture. For this reason the power ratio $R = P_{ref}/P_{aperture}$ between the two ports has to be measured in order to determine the number of photons reaching the SiPM from the light power P_{ref} measured with the calibrated sensor. This ratio was measured by covering both ports with a calibrated sensor.

For the $\varnothing 0.8$ mm aperture which is used for the measurement of the relative sensitivity this was done for the whole spectral range from 350 nm to 1000 nm with a step size of 10 nm using the Xenon lamp as a light source. The bandwidth of the light selected by the monochromator was measured to be ≈ 2 nm. The measured power ratio $R_{0.8}$ which is shown in figure 4.26 depends on the wavelength with a maximum deviation of $\approx 10\%$ from the mean value. This might be explained by a wavelength dependent reflection and absorption inside the brass aperture. The precision of the measurement is limited by the uncertainty of the calibrated PIN-diode ($\approx 5\%$) which was used to measure the light power behind the aperture.

The power ratio for the $\varnothing 0.6$ mm aperture was determined for the laser diodes and LEDs used for the PDE measurement. The measured ratio $R_{0.6}$ shown in table 4.5 is much larger than the ratio shown in figure 4.26 due to the smaller diameter of the aperture. The emission spectra of the laser diodes and LEDs were measured by placing the light sources in front of the monochromator and measuring the output power as a function of the wavelength in order to determine the center wavelength (see table 4.5). The FWHM of the emission spectra was found to be less than 5 nm for the laser diodes and 10 – 20 nm for the LEDs.

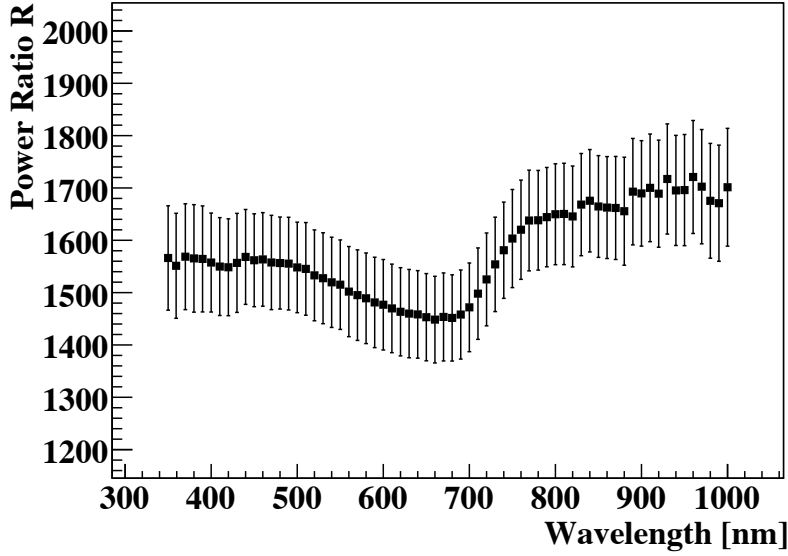


Figure 4.26: Power ratio $R_{0.8}$ between the two ports of the integration sphere measured for the $\varnothing 0.8$ mm aperture.

Type	λ_{center} [nm]	$R_{0.6}$
LED	465	4200 ± 20
Laser Diode	633	3852 ± 18
Laser Diode	775	4328 ± 7
LED	870	4625 ± 55

Table 4.5: Power ration $R_{0.6}$ between the two ports of the integration sphere measured for the $\varnothing 0.6$ mm.

Relative Spectral Sensitivity

The relative sensitivity was measured for a fixed bias voltage in a spectral range from 350 nm to 1000 nm with a step size of 10 nm using a Xenon lamp as a light source. For this setup it is not possible to read out the SiPM with a QDC which would require a pulsed light source (see chapter 3.2). For this reason the SiPM is read out with a picoamperemeter measuring the photocurrent. Figures 4.27 and 4.28 show the spectrum of the Xenon lamp measured with the SiPM placed behind the aperture and the calibrated sensor mounted on the top port of the integrating sphere. Considering the power ratio $R_{0.8}$ between the two ports the relative sensitivity S can be determined from the measured photocurrent I_{SiPM} of the SiPM according to the following formula:

$$S(\lambda) = \frac{I_{SiPM} \cdot R_{0.8} / (q_e \cdot G)}{P_{opt} / (h \cdot \frac{c}{\lambda})} \quad (4.21)$$

where P_{opt} is the optical power measured with the calibrated sensor, h is the Planck constant and G is the gain of the SiPM. Since the photocurrent is influenced by the effects of dark-rate, cross-talk and after-pulses the values for the relative sensitivity S are larger than the actual PDE. The measurement results are shown in on the right side of figures 4.29 to 4.31. (The

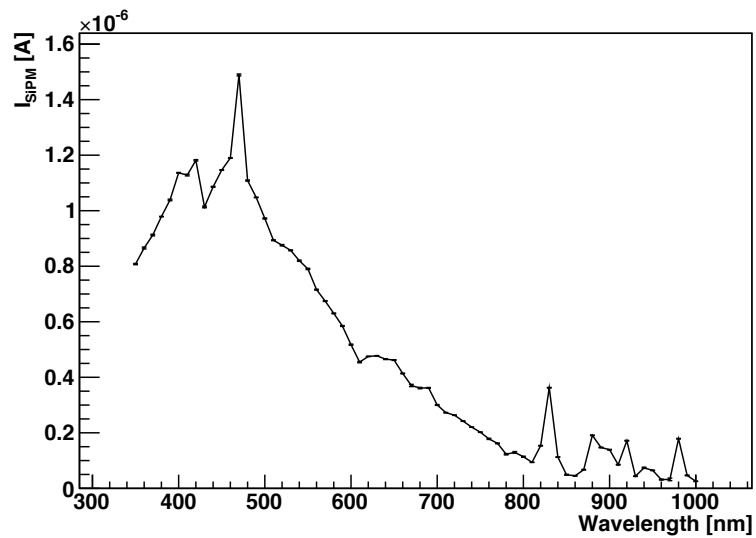


Figure 4.27: Spectrum of the Xenon lamp measured with the S10362-11-050C No163 in front of the $\varnothing 0.8$ mm aperture.

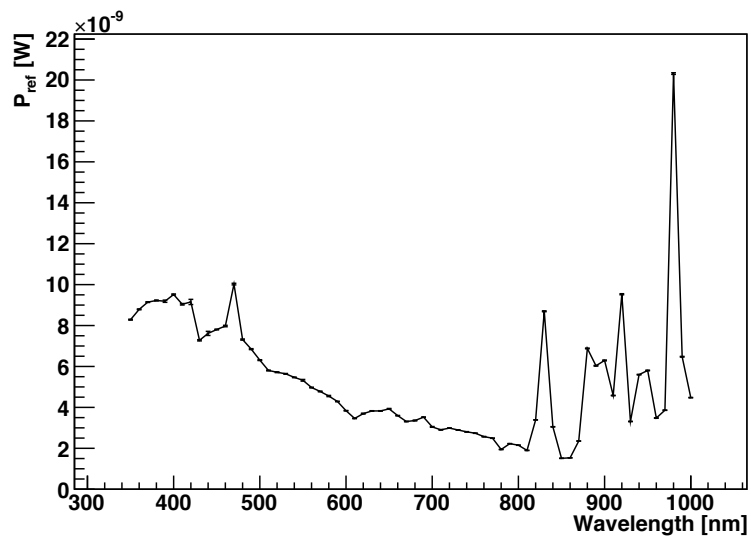


Figure 4.28: Spectrum of the Xenon lamp measured with the calibrated photodiode at the upper port of the integrating sphere.

curves are already scaled to the measured PDE at 633 nm (see below)).

PDE Measurement

In this section the measurement of the PDE without the effects of dark-rate cross-talk and after-pulses is discussed. For this measurement different laser diodes and LEDs with center wavelengths of 465 nm, 633 nm, 775 nm and 870 nm can be used as light sources. The used laser diode or LED is driven by a pulse generator in order to measure the charge spectrum of the SiPM using a QDC (see chapter 3.2). This allows to determine the number of detected photons $\langle N_{p.e.} \rangle$ (see equation 4.2) without dark-noise, cross-talk and after-pulses by applying the statistical analysis discussed in chapter 4.1. Considering the optical power P_{opt} measured with the calibrated sensor, the power ratio $R_{0.6}$ and the period $T = 30 \mu s$ of the light pulses the PDE can be calculated according to the following formula:

$$PDE = \frac{\langle N_{p.e.} \rangle \cdot R_{0.6} / T}{P_{opt} / (h \cdot \frac{c}{\lambda})} \quad (4.22)$$

where h is the Planck constant, λ is the center wavelength of the laser diode or LED and c is the speed of light.

Figures 4.29 to 4.31 (left) show the results of the PDE measurements for a certain range of the bias voltage. The PDE increases with the over-voltage due to the increasing probability $\epsilon_{avalanche}$ for a charge carrier to initiate an avalanche breakdown (see equation 2.8). The PDE saturates if $\epsilon_{avalanche}$ reaches its maximum. A similar behavior has been observed in [32]. Another important parameter influencing the PDE is the geometrical fill factor. It explains the much larger PDE of the MPPC with 400 pixels (S10362-11-050C) compared to the 1600 pixel device (S10362-11-025C). In the measured range for the over-voltage the PDE of the SensL SiPM is lower than for the S10362-11-025C although the fill factor is larger.

The measurements were carried out at a temperature of $25.0 \pm 1.5^\circ \text{C}$. The temperature fluctuations cause small shifts in the over-voltage between the measurement series at different wavelengths. The minimum over-voltage which can be applied for the PDE measurement is limited due to the fact that the statistical analysis (see chapter 4.1) which is used to determine the PDE requires the photon peaks in the charge spectrum to be well separated. The maximum over-voltage is limited due to unstable operation of the device (e.g. pedestal shifts and broadening of the single photon peaks due to increased noise) at high over-voltage.

The measurement technique used to determine the PDE can only be applied for the specific wavelength of the available LEDs and laser diodes. However, the PDE can be determined for the full spectral range from 350 nm to 1000 nm by scaling the curve for the relative sensitivity so that it matches the values for the PDE at the corresponding wavelength. This is shown on the right of figures 4.29 to 4.31. The relative spectral sensitivity was scaled to the PDE value at 633 nm at the maximum over-voltage measured. The PDE values measured at 465 nm, 775 nm and 870 nm at the same bias voltage are also shown in the graph in order to cross-check the results. Within the uncertainty of the measurement the values are consistent with the PDE curve which validates the measurement results.

The HAMAMATSU MPPCs show a high PDE in the blue spectral region peaking at $\approx 450 \text{ nm}$. This would allow to read out the blue scintillation light from the tiles of the CALICE HCAL prototype without the need for wavelength shifting fibers. The reason for the high sensitivity in the blue spectral range is the p-on-n doping profile of the devices. Blue light cannot penetrate deeply into the silicon due to its high optical absorption coefficient (see figure 2.4). As a

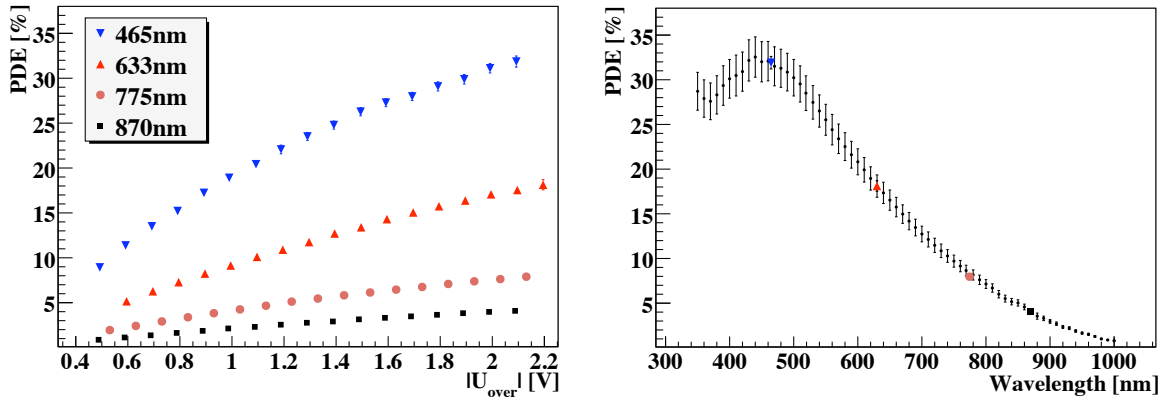


Figure 4.29: Left: Photon detection efficiency of the HAMAMATSU S10362-11-050C No163 as a function of the over-voltage for different wavelength. **Right:** PDE as a function of the wavelength at an over-voltage of $V_{over} = 2.15 \pm 0.05$ C at room temperature ($25.0 \pm 1.5^\circ$ C).

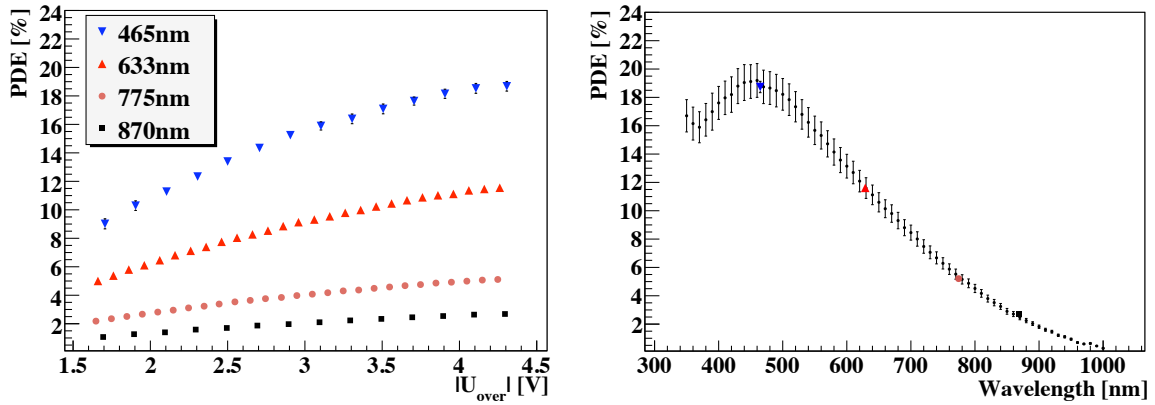


Figure 4.30: Left: Photon detection efficiency of the HAMAMATSU S10362-11-025C No132 as a function of the over-voltage for different wavelength. **Right:** PDE as a function of the wavelength at an over-voltage of $V_{over} = 4.30 \pm 0.05$ C at room temperature ($25.0 \pm 1.5^\circ$ C).

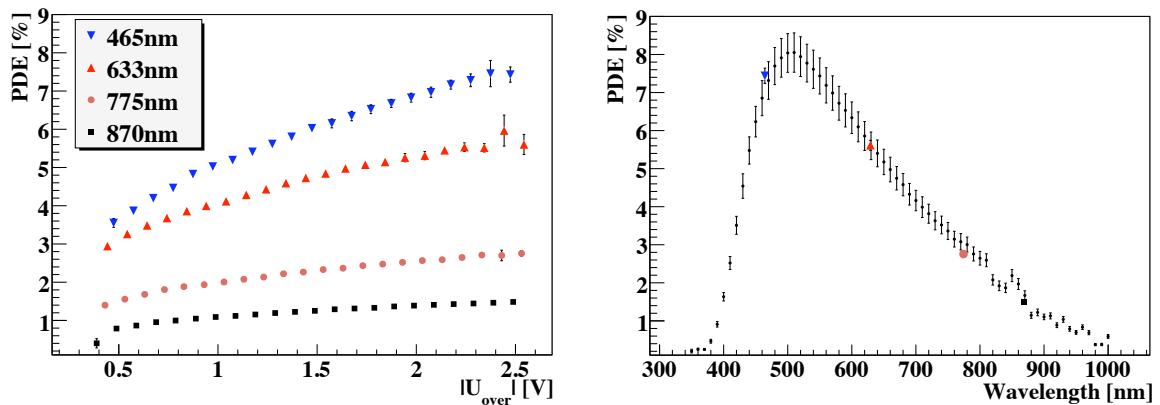


Figure 4.31: Left: Photon detection efficiency of the SensL SPMMicro1020X13 No4 as a function of the over-voltage for different wavelength. **Right:** PDE as a function of the wavelength at an over-voltage of $V_{over} = 2.50 \pm 0.05$ C at room temperature ($25.0 \pm 1.5^\circ$ C).

consequence, the majority of electron-hole pairs are produced in the p-layer close to the surface of the sensor. The probability for the electron in the p-layer to initiate an avalanche breakdown is higher than for the holes in the n-layer due to the different impact ionization coefficients (see figure 2.6). For this reason, the PDE decreases for photons with longer wavelength which are mostly absorbed in the n-layer. Furthermore the probability for a hole to recombine before reaching the multiplication region is higher if the hole is produced in the drift region far away from the multiplication region. The PDE curve of the SensL SiPM is shifted to longer wavelength with respect to the HAMAMATSU sensors because of the n-on-p doping profile. For this device the peak sensitivity is in the green spectral region (≈ 520 nm) whereas the sensitivity in the blue region is significantly reduced due to the low impact ionization coefficient of the holes in the n-layer close to the surface of the sensor.

4.7 Uniformity Measurements

A high uniformity in the response of the individual pixels is essential for a good separation of the single photon signals. The setup discussed in chapter 3.6 can be used to scan a sensor with a focused light spot in order to study the spatial uniformity in the sensitivity, gain and cross-talk probability of the device. A charge spectrum with 10,000 events is acquired for every position of the light spot using a QDC to read out the SiPM. The light spot used to scan the SiPM has a diameter of a few micron which is significantly smaller than the typical size of a pixel. For this reason the charge spectrum of an ideal sensor would only contain pedestal and 1 p.e. events since only one pixel is illuminated at a time. However, for a real sensor also events where more than one pixel have fired can be observed due to the effects of dark-rate, cross-talk and after-pulses.

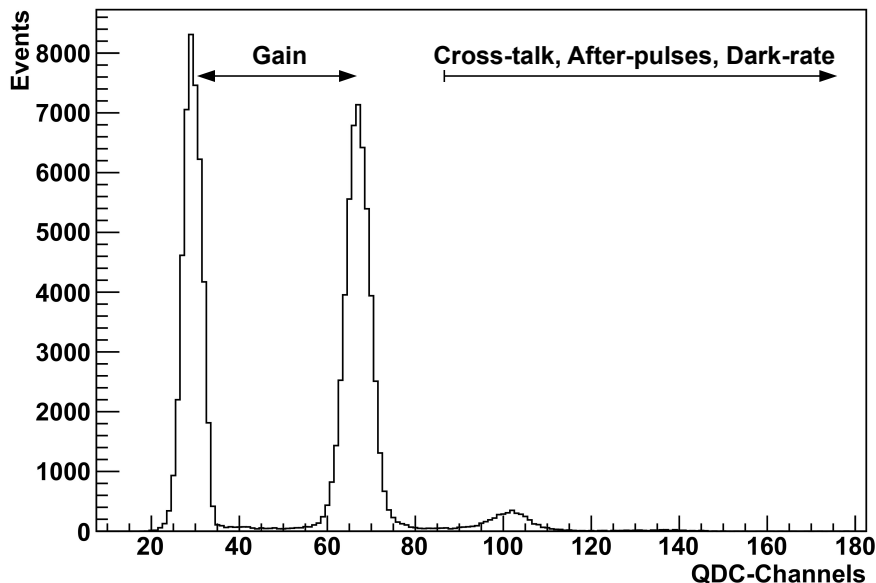


Figure 4.32: Single pixel charge spectrum. For an ideal sensor only 1 p.e. and 2 p.e. events are expected (first two peaks). All events with a higher charge value are caused by dark-rate, cross-talk or after-pulses.

Figure 4.32 shows a typical charge spectrum of a single pixel. Applying the statistical analysis discussed in chapter 4.1, the number of detected photons without dark-rate, cross-talk and after-pulses can be determined from the number of events in the pedestal peak according to equation 4.2. The cross-talk probability can be determined from the number of events where two or more pixel have fired (see equation 4.11). This analysis is discussed in detail in chapter 4.3. Considering a step size of $5\ \mu\text{m}$, a scan of the full sensitive area of a SiPM consists out of ≈ 50000 measurement points. Because of this large amount of data a ROOT program was designed to automate the analysis of the recorded charge spectra. The sensitivity, gain and cross-talk probability is determined for every position of the light spot and a 2D map of the particular parameters is created by combining all measurement points. In the following sections the results of the scan for the HAMAMATSU S10362-11-100C and S10362-11-050C are presented.

Results of the Uniformity Measurements

Figure 4.33 shows a map of the number of detected photons corrected for the effects of dark-rate, cross-talk and after-pulses. The values are normalized to the maximum number of photons observed and scaled to the light intensity measured with the monitoring photodiode in order to correct for changes in the intensity of the laser diode. Both tested devices show a high uniformity in the sensitivity with variations around the mean value of $< 10\%$. The gain of the two tested devices is shown in figure 4.34. In between two pixels the gain is not well defined since the number of events generated by photon absorption is small compared to thermally generated events. For this reason the gain is only calculated for measurement points with a sensitivity higher than 50% of the maximum value. It can be seen that the gain is also quite uniform with fluctuations of $\approx 10\%$, however, there seem to be systematic variances. The gain for the 100 pixel device is slightly lower for the bottom pixels. This could be explained by the changing temperature during the measurement time. At the beginning of the measurement (lower part of the sensor) the temperature was $\approx 0.7\ ^\circ\text{C}$ higher than at the end of the measurement (upper part of the sensor) which results in a lower gain for the pixels at the bottom. The 400 pixel device shows a lower gain for the pixels at the edge of the sensor. These variations cannot be explained by the temperature fluctuations during the measurement ($\approx 0.2\ ^\circ\text{C}$) since the temperature dependence of the gain of this device is by a factor 4 smaller than for the 100 pixel sensor (see table 4.4). The observed behavior could possibly be caused by a drop in the bias voltage towards the border of the sensor due to the resistance of the electrical connections between the pixels. However, further investigations are necessary to fully understand the observed gain variations.

Figure 4.35 shows a map of the cross-talk probability of the tested devices which is determined by the fraction of events where more than one pixel fired (see equation 4.11). In contrast to the measurements discussed in chapter 4.3 the charge integration time for the sensor scans has to be long enough to contain at least one full pulse in order to determine the gain. For this reason, after-pulses cannot be excluded completely and only an effective probability containing both cross-talk and after-pulses can be determined. However, the contribution from after-pulses can be assumed to be small since the integration time was set to the minimum value such that it still contains one full pulse. Similar to the gain, the cross-talk is not well defined in between two pixels and therefore a cut on 50% sensitivity is applied. It can be seen that the cross-talk probability in the center of the sensor is higher than at the borders. This phenomena is expected since the pixels at the border of the device have less neighboring pixels than pixels in the center. Photons that are generated in an avalanche breakdown in the outer region of

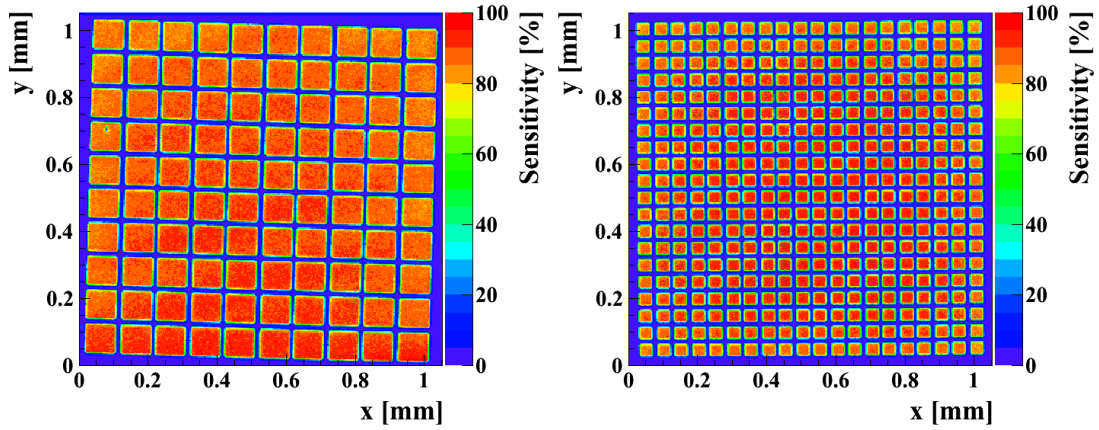


Figure 4.33: Map of the relative sensitivity of the HAMAMATSU S10362-11-100C No181 (left) and S10362-11-050C No163 (right).

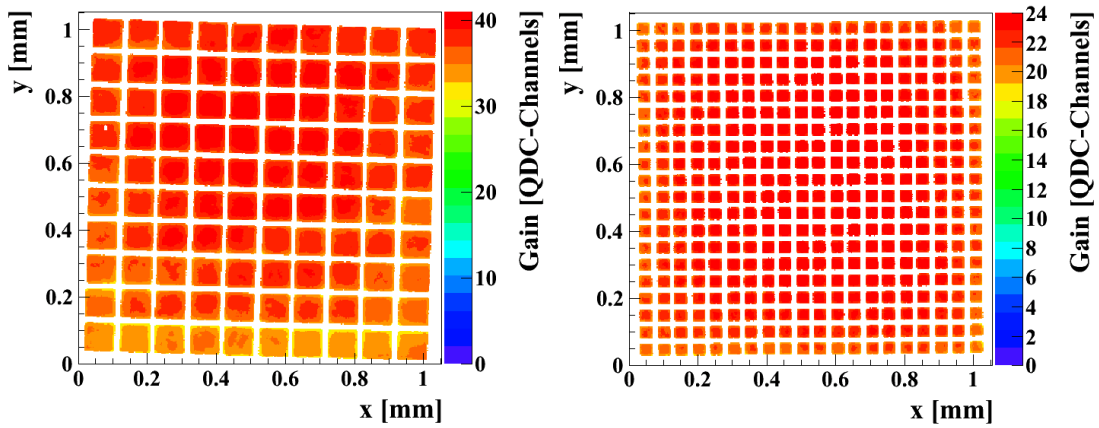


Figure 4.34: Gain map of the HAMAMATSU S10362-11-100C No181 (left) and S10362-11-050C No163 (right). The measurement points with a sensitivity smaller than 50% were set to zero.

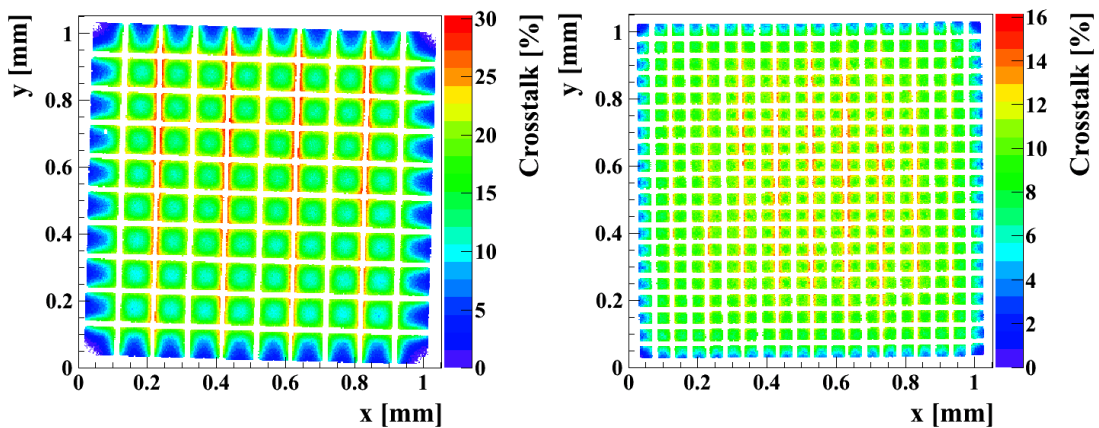


Figure 4.35: Cross-talk map of the HAMAMATSU S10362-11-100C No181 (left) and S10362-11-050C No163 (right). The measurement points with a sensitivity smaller than 50% were set to zero.

the sensor therefore have a reduced probability to be absorbed in a nearby pixel. It can be observed (in particular for the 100 μm device) that the cross-talk probability varies within a single pixel, i.e. the cross-talk probability is increased if the incident photon is absorbed near the border of a pixel. This could mean that the avalanche does not spread uniformly over the hole device because otherwise a uniform cross-talk behavior would be expected. If the avalanche is more pronounced at the position where the photon was absorbed the observed behavior can be explained.

4.8 Photon-counting Resolution

The photon-counting resolution is one of the most important properties of a SiPM. If the SiPM is used for the detection of scintillation light like in calorimetric applications or PET, it is one of the limiting factors for the energy resolution of the detector. The photon-counting resolution is determined by the photon detection efficiency and noise generated by cross-talk, after-pulses, and dark-noise. In the following, the contributions of the different effects to the photon-counting resolution will be determined for the linear range of the sensor ($N_\gamma \ll N_{\text{pixels}}$).

Assuming an ideal sensor with no cross-talk, after-pulses and dark-rate, the photon-counting resolution is limited by the fluctuations in the number of detected photons. Considering a fixed number of incident photons N_γ , the probability to detect a certain number of photons N_{PDE} is described by a binomial distribution:

$$B_{PDE}(N_{PDE}) = \binom{N_\gamma}{N_{PDE}} PDE^{N_{PDE}} \cdot (1 - PDE)^{N_\gamma - N_{PDE}} \quad (4.23)$$

The photon-counting resolution is then given by the standard deviation of the binomial distribution:

$$\sigma_{N_{PDE}} = \sqrt{N_\gamma \cdot PDE(1 - PDE)} \quad (4.24)$$

The mean number of detected photons is given by:

$$\langle N_{PDE} \rangle = N_\gamma \cdot PDE$$

For a real sensor, another limiting factor for the resolution is the dark-rate. The probability to have a certain number of dark-rate events N_{DR} within a certain charge integration time Δt is given by a Poisson distribution with the expectation value $\langle N_{DR} \rangle = DR \cdot \Delta t$ where DR is the dark-rate in Hz. The fluctuations in the number of dark-rate events is given by the standard deviation:

$$\sigma_{N_{DR}} = \sqrt{DR \cdot \Delta t}$$

Furthermore, the fluctuations in the number of cross-talk and after-pulse events have to be taken into account. Each detected photon or dark-rate event can trigger an additional avalanche breakdown due to cross-talk or after-pulsing. In the following calculations it is assumed that one firing pixel may only trigger one cross-talk or one after-pulse event. All higher order events are neglected since $P_{CT}^2, P_{AP}^2, P_{CT} \cdot P_{AP}$ are small. If $\langle N_{PDE} \rangle + \langle N_{DR} \rangle$ pixels fired, the probability for a certain number of cross-talk events N_{CT} and after-pulse events N_{AP} is again described by a binomial distribution:

$$B_{CT}(N_{CT}) = \binom{\langle N_{PDE} \rangle + \langle N_{DR} \rangle}{N_{CT}} P_{CT}^{N_{CT}} \cdot (1 - P_{CT})^{\langle N_{PDE} \rangle + \langle N_{DR} \rangle - N_{CT}} \quad (4.25)$$

$$B_{AP}(N_{AP}) = \binom{\langle N_{PDE} \rangle + \langle N_{DR} \rangle}{N_{AP}} P_{AP}^{N_{AP}} \cdot (1 - P_{AP})^{\langle N_{PDE} \rangle + \langle N_{DR} \rangle - N_{AP}} \quad (4.26)$$

where P_{CT} and P_{AP} represent the cross-talk and after-pulse probability. The fluctuations in the number of cross-talk and after-pulse events is given by:

$$\sigma_{N_{CT}} = \sqrt{(\langle N_{PDE} \rangle + \langle N_{DR} \rangle) \cdot P_{CT}(1 - P_{CT})} \quad (4.27)$$

$$\sigma_{N_{AP}} = \sqrt{(\langle N_{PDE} \rangle + \langle N_{DR} \rangle) \cdot P_{AP}(1 - P_{AP})} \quad (4.28)$$

Considering all effects described above, the standard deviation of the measured SiPM signal is given by:

$$\sigma_{Signal} = \sqrt{\sigma_{N_{PDE}}^2 + \sigma_{N_{CT}}^2 + \sigma_{N_{AP}}^2 + \sigma_{N_{DR}}^2} \quad (4.29)$$

The electronic and excess noise of the sensor also contribute to the standard deviation of the signal. However, the excellent separation of the single photon peaks in the charge spectrum shows that both effects are small compared to the signal of a firing pixel (gain) and can therefore be neglected in the following calculations. Having individually determined the PDE, dark-rate, cross-talk and after-pulse probability, the incident number of photons can be reconstructed from the measured SiPM signal with the following formula:

$$N_{\gamma} = \frac{N_{Signal} - \langle N_{CT} \rangle - \langle N_{AP} \rangle - \langle N_{DR} \rangle}{PDE} \quad (4.30)$$

The standard deviation of the reconstructed number of photons is:

$$\sigma_{N_{\gamma}} = \frac{\sigma_{N_{Signal}}}{PDE} \quad (4.31)$$

which leads to a relative photon-counting resolution of:

$$\frac{\sigma_{N_{\gamma}}}{N_{\gamma}} = \frac{\sigma_{N_{Signal}}}{N_{\gamma} \cdot PDE} = \frac{\sqrt{\sigma_{N_{PDE}}^2 + \sigma_{N_{CT}}^2 + \sigma_{N_{AP}}^2 + \sigma_{N_{DR}}^2}}{N_{\gamma} \cdot PDE} \quad (4.32)$$

$$= \frac{A}{N_{\gamma}} \oplus \frac{B}{\sqrt{N_{\gamma}}} \quad (4.33)$$

where

$$A = \sqrt{DR \cdot \Delta t (1 + P_{CT}(1 - P_{CT}) + P_{AP}(1 - P_{AP}))} / PDE$$

describes the component resulting from dark-rate pulses and

$$B = \sqrt{(1 - PDE) + P_{CT}(1 - P_{CT}) + P_{AP}(1 - P_{AP})} / \sqrt{PDE}$$

corresponds to the fluctuations originating from events triggered by photon absorption. Both contributions are effected by after-pulses and cross-talk.

The photon-counting resolution can be determined using the results (i.e. PDE, dark-rate, cross-talk and after-pulse probability) of the measurements described in the previous sections. In the following monochromatic photons with a wavelength of 645 nm and an integration time of $\Delta t = 300$ ns matching the approximate bunch crossing time at the ILC were assumed for the calculations. In principle this requires the after-pulse probability to be calculated for this specific time interval. However, the after-pulse probability for $\Delta t > 300$ ns is negligible small due to the characteristic trapping time of < 150 ns (see figure 4.13). For this reason the after-pulse probability for an infinite integration time (as calculated in section 4.4) was used. For

the SensL sensors the after-pulse probability was measured to be negligible small due to the long signal decay time (see chapter 4.4) and hence was set to zero.

Figures 4.36 to 4.38 show the squared value of the relative photon-counting resolution of the HAMAMATSU MPPCs with 400 and 1600 pixels and the SensL SPM with 848 pixels for $N_\gamma = 1$ and $N_\gamma = 10$. Besides the total resolution, the contributions $\sigma_{N_i}/(N_\gamma \cdot PDE)$ considering only cross-talk, after-pulsing, dark-rate and PDE, respectively, are shown.

It can be seen that the limiting factors for the photon-counting resolution for single photon detection ($N_\gamma = 1$) is the PDE and the dark-rate. In case of the MPPCs, the resolution improves with the over-voltage due to the increasing PDE. Although the dark-rate increases exponentially with the over-voltage, its contribution to the resolution is approximately constant since the fraction of dark-rate events to photon events decreases with the over-voltage due to the rising PDE. For the SensL sensor the resolution for $N_\gamma = 1$ is significantly limited by the high dark-rate and the low PDE. The influences from cross-talk and after-pulses are small for all tested SiPMs.

For ten incident photons (right side of figures 4.36 to 4.38) the resolution of the MPPCs is dominated by the PDE. The contribution from the dark-rate can be neglected since the fraction of dark-rate events to photon events is small. For the SensL SPM the contribution from the dark-rate is still large. However, for a larger number of incident photons the resolution of the SPM will also be dominated by the PDE since the contribution from the dark-rate decreases with $\sigma_{N_{DR}} \propto 1/N_\gamma$ whereas all other contributions drop with $\propto 1/\sqrt{N_\gamma}$ (see equation 4.33). Figure 4.39 illustrates this dependence of the photon-counting resolution on the number of incident photons N_γ for the S10362-11-050C at an over-voltage of 1.9 V (highest over-voltage the resolution was calculated for). For this device the contribution from dark-rate can be neglected for $N_\gamma \gtrsim 10$. The photon-counting resolution for moderate photon fluxes therefore cannot be significantly improved by cooling the device which would reduce the dark-rate. The AHCAL prototype is calibrated to detect ≈ 15 photons for a minimal ionizing particle (MIP). Considering a typical PDE of $\approx 30\%$ for the S10362-11-050C, this corresponds to ≈ 50 incident photons. At this photon flux the resolution is about $\sqrt{0.08} \approx 30\%$.

It can be seen in figures 4.36 to 4.38 that the over-voltage corresponding to the best resolution depends on the incident photon flux. Although the PDE increases with the bias voltage, a moderate over-voltage is preferred in case of single photon detection due to the exponentially increasing dark-rate. If the number of incident photons is large enough that the dark-rate can be neglected, the best resolution is achieved when the SiPM is operated at high over-voltage. If the over-voltage is too large the PDE saturates and the resolution will be limited by the increasing cross-talk and after-pulse probability. However, this effect is not observed within the range of the over-voltage for which the photon-counting resolution was determined. The resolution of the tested SiPM for the highest over-voltage within the measured range is shown in table 4.6.

The resolution of the MPPC with 1600 pixels is a factor ≈ 1.3 worse than the resolution of the 400 pixel device. However, for calorimetric applications a large dynamic range is important. The relative resolution described in equation 4.33 is only valid in the linear range of the SiPM. If the SiPM response saturates for high photon fluxes this will degrade the resolution of the sensor. For this reason, the MPPC with 1600 pixels is expected to have a better photon-counting resolution for high photon fluxes compared to the 400 pixel device and therefore is better suited for the HCAL application. The resolution of the SensL SPM is significantly limited due to the high dark-rate and low PDE compared to the HAMAMATSU MPPCs. The study of the photon-counting resolution could be complemented by a direct measurement of

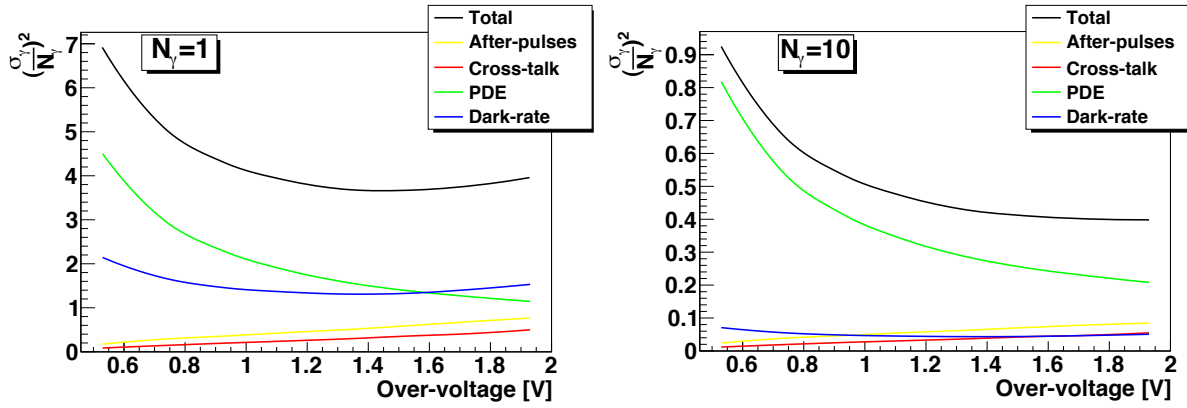


Figure 4.36: Squared relative photon-counting resolution of the HAMAMATSU S10362-11-050C No163 for one (left) and ten incident photons (right).

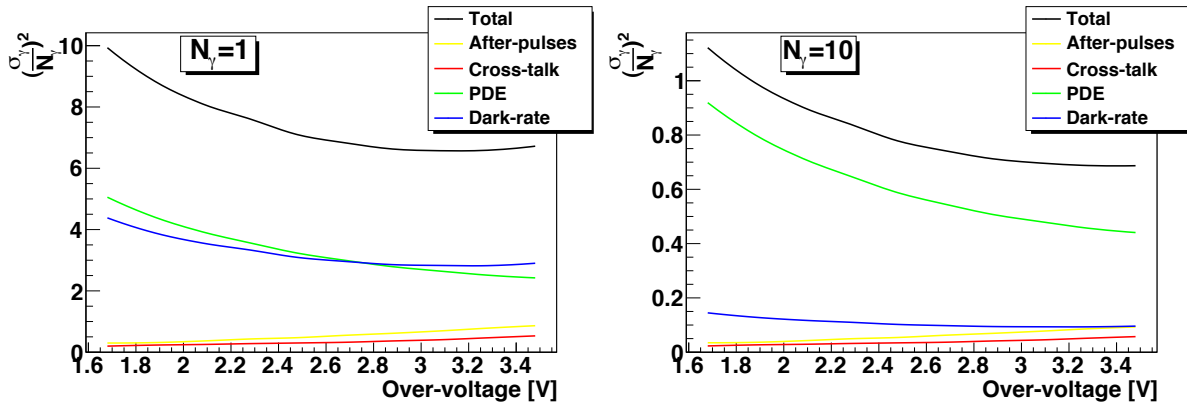


Figure 4.37: Squared relative photon-counting resolution of the HAMAMATSU S10362-11-025C No132 for one (left) and ten incident photons (right).

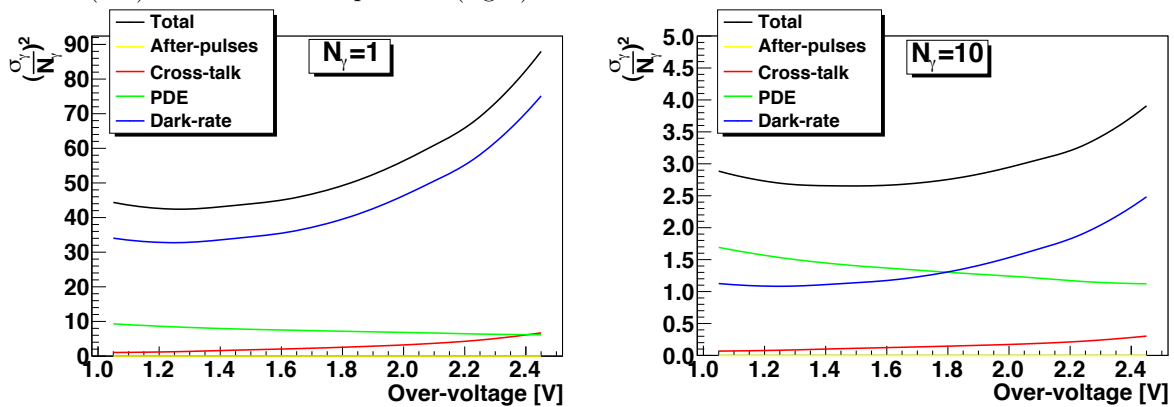


Figure 4.38: Squared relative photon-counting resolution of the SensL SPMMicro1020X13 No4 for one (left) and ten incident photons (right).

the resolution in order to validate the results presented above and to determine the resolution in the non-linear range.

Sensor	$\sigma_{N_\gamma}/N_\gamma$	Over-voltage
S10362-11-050C No163	$2.93/N_\gamma \oplus 1.90/\sqrt{N_\gamma}$	1.9 V
S10362-11-025C No132	$3.79/N_\gamma \oplus 2.50/\sqrt{N_\gamma}$	3.5 V
SPMMicro1020X13 No4	$18.03/N_\gamma \oplus 3.66/\sqrt{N_\gamma}$	2.5 V

Table 4.6: Photon-counting resolution of the tested SiPMs.

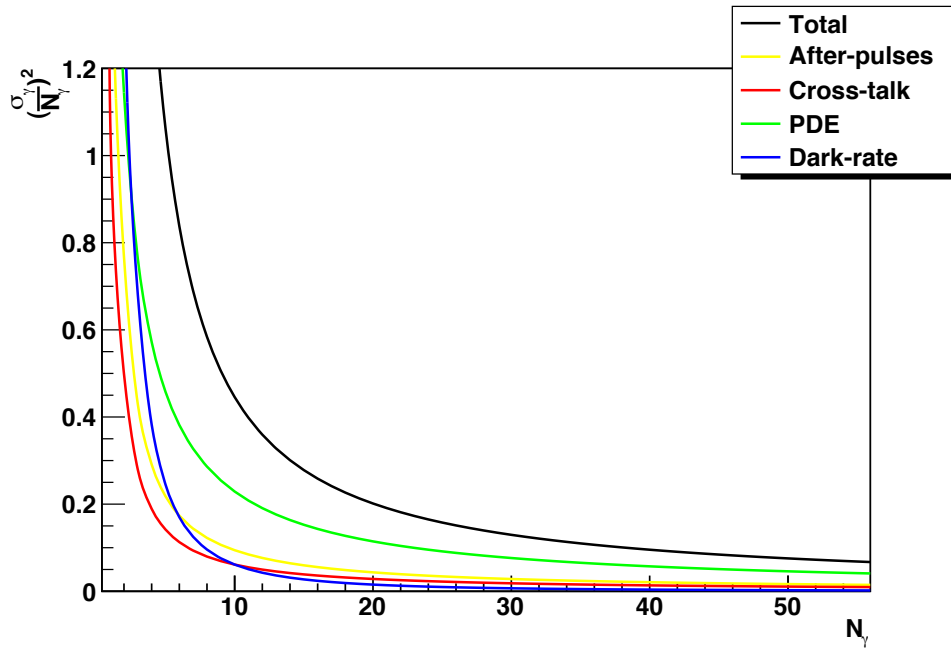


Figure 4.39: Squared relative photon-counting resolution of the HAMAMATSU S10362-11-050C No163 as a function of the number of incident photons for an over-voltage of 1.9 V. The contribution from the dark-rate is proportional to $\propto 1/N_\gamma$ whereas the other contributions decrease with $\propto 1/\sqrt{N_\gamma}$.

Chapter 5

Summary and Outlook

This thesis is devoted to the characterization of *Silicon Photomultipliers* (SiPMs), a novel type of solid state photodetectors suitable for low intensity light detection. The basic properties of these devices are: high gain and sensitivity, small size, robustness, low operation voltage, insensitivity to magnetic fields and low excess noise. These characteristics make the SiPM a promising device for the application in high energy physics calorimetry or medical imaging.

The *International Linear Collider* (ILC) experiment demands the development of a new generation of calorimeters with unprecedented jet-energy resolution to satisfy the requirements set by the physics goal. Such an excellent resolution can be achieved with a highly granular sampling calorimeter utilizing the *Particle Flow Approach*. A prototype of such a calorimeter using SiPMs for the readout of the scintillation light has been built at DESY in order to study the concept and physics performance of such a calorimeter.

Another application of the SiPM is the medical imaging technique of *Positron Emission Tomography* (PET). The small size of the SiPM allows for a design with a high granularity which improves the spatial resolution of the PET detector. Since the SiPM is insensitive to magnetic fields, a combination of a PET and *Magnetic Resonance Imaging* (MRI) is possible. Furthermore, the good timing resolution of the SiPM allows to improve the precision of *Time-of-Flight* PET. For this reasons a PET prototype utilizing SiPMs was build in the workshop of the institute in order to study the performance and demonstrate the applicability of this concept.

A test stand was developed to measure and compare the characteristic properties of different SiPMs in order to find the device best suited for a specific application. In the context of this thesis the test stand was largely extended in order to allow a faster and more complete characterization of SiPMs. Besides the measurement of the gain, breakdown voltage, sensitivity and dark-rate, the new setup now allows to determine the PDE (without the effects of dark-rate, cross-talk and after-pulses) in a spectral range from 350 nm to 1000 nm, the cross-talk and after-pulse probability and the temperature dependence of different parameters. In addition, the pixel uniformity in terms of the spatial variations of sensitivity, gain and cross-talk can be studied. The measurement process and data analysis were automatized in order to allow the fast characterization of a large number of sensors.

In this thesis several commercially available SiPM types (four HAMAMATSU MPPCs with 100, 400 and 1600 pixels and two SensL SPMs with 848 pixels) were characterized and compared. Depending on the sensor type and the applied bias voltage, a PDE of 7 to 30%, a gain of $\approx 10^6$ and a typical dark-rate of 0.5 to 2 MHz was measured. The cross-talk and after-pulse probability is in the range of 1 to 50%. The results of the PDE, dark-rate, cross-talk and after-pulse measurement were combined to determine the photon-counting resolution for the linear range of the sensors. For the MPPC with 400 pixels a resolution of $\sigma_{N_\gamma}/N_\gamma = 2.93/N_\gamma \oplus 1.90/\sqrt{N_\gamma}$ was determined for an over-voltage of 1.9 V. It was shown that the limiting factor for the photon-counting resolution is the PDE.

The measurement results presented in this thesis show that the test stand allows a precise and complete analysis of the SiPM characteristics. In the future the characterization of a series of devices identical in construction is planned in order to study the “device to device”-uniformity (e.g. variations of the break-down voltage) which is important for the PET and ILC application since a huge number of SiPMs are required. The next step concerning the HCAL application is to study the response of the combined SiPM - tile system. Regarding the PET prototype, the combined system of the SiPM attached to the scintillating crystal will be studied.

Bibliography

- [1] N. Phenomena et al. Combined CDF and DZero Upper Limits on Standard Model Higgs-Boson Production with up to 4.2 fb⁻¹ of Data, 2009.
- [2] <http://www.hep.phy.cam.ac.uk/~drw1/particleandnuclear/>.
- [3] Ilc reference design report, August 2007.
- [4] M. Thomson. Progress with Particle Flow Calorimetry. In *proceedings of 2007 International Linear Collider Workshop (LCWS07 and ILC07)*, Hamburg, Germany, May-June, 2007.
- [5] V. Andreev, J. Cvach, M. Danilov, E. Devitsin, V. Dodonov, G. Eigen, E. Garutti, Y. Gilitzky, M. Groll, R.D. Heuer, et al. A high-granularity plastic scintillator tile hadronic calorimeter with APD readout for a linear collider detector. *Nuclear Inst. and Methods in Physics Research, A*, 564(1):144–154, 2006.
- [6] The ILD concept group. Detector outline document for the fourth concept detector (“4th”) at the international linear collider, March 2009.
- [7] The SiD concept group. Sid letter of intent, March 2009.
- [8] The 4th concept group. Letter of intent from the fourth detector (“4th”) collaboration at the international linear collider, March 2009.
- [9] JC Brient and H. Videau. The calorimetry at the future e+ e-linear collider. *Arxiv preprint hep-ex/0202004*, 2002.
- [10] J.C. Brient. Improving the Jet Reconstruction with the Particle Flow Method; an Introduction. *Arxiv preprint physics/0412149*, 2004.
- [11] JC Brient, P. Dauncey, E. Garutti, I. Laktineh, R. Poeschl, J. Repond, F. Sefkow, T. Take-shita, D. Ward, and J. Yu. CALICE Report to the Calorimeter R&D Review Panel. *Arxiv preprint arXiv:0707.1245*, 2007.
- [12] N. D’Ascenzo^a, A. Eggemann^b, and E. Garutti^b. Study of Micro Pixel Photon Counters for a high granularity scintillator-based hadron calorimeter. *arXiv:0711.1287*, 2007.
- [13] Alexander Tadday. Characterization of silicon photomultipliers. Diploma thesis, Kirchhoff Institute for Physics Heidelberg, 2008.
- [14] W.W. Moses. Advantages of improved timing accuracy in PET cameras using LSOscintillator. *Name: IEEE Transactions on Nuclear Science*, 3, 2002.
- [15] Gerhard Lutz. *Semiconductor Radiation Detectors*. Springer, 1999.
- [16] HAMAMATSU. *Technical Information: Characteristics and use of Si APD (Avalanche Photodiodes)*, May 2004.

- [17] HAMAMATSU. *Photodiode Technical Information*.
- [18] Christiana Honsberg and Stuart Bowden. Optical properties of silicon. <http://www.udel.edu/igert/pvcdrom/index.html>.
- [19] Kwok K. Ng. *Complete Guide to Semiconductor Devices*. Wiley, 2002.
- [20] Brian F. Aull, Andrew H. Loomis, Douglas J. Young, Bradley M. Heinrichs, Richard J. Felton, Peter J. Daniels, and Deborah J. Landers. Geiger-mode avalanche photodiodes for three-dimensional imaging. *LINCOLN LABORATORY JOURNAL*, 13(2):335–350, 2002.
- [21] V. Golovin. Patent no. ru, 2142175, 1998.
- [22] Z. Sadygov. Patent no. ru, 2102820, 1998.
- [23] Nanda Wattimena. The calice tile hadron calorimeter prototype with silicon photomultiplier readout. In *10th ICATPP Conference on Astroparticle, Particle, Space Physics, Detectors and Medical Physics Applications*, 2007.
- [24] P. Buzhan, B. Dolgoshein, A. Ilyin, V. Kantserov, V. Kaplin, A. Karakash, A. Pleshko, E. Popova, S. Smirnov, Y. Volkov, et al. An advanced study of silicon photomultiplier. *ICFA Instrum. Bull*, 23:28–41, 2001.
- [25] Y Du and F Retière. After-pulsing and cross-talk in multi-pixel photon counters. *Nuclear Instruments and Methods in Physics Research Section A: Accelerators, Spectrometers, Detectors and Associated Equipment*, 596(3):396–401, 2008.
- [26] Kolja Prothmann. Comparative measurements of silicon photomultipliers for the readout of a highly granular hadronic calorimeter. Diploma thesis, Max-Planck-Institut for Physics Munich, 2008.
- [27] A. Lacaita, S. Cova, A. Spinelli, and F. Zappa. Photon-assisted avalanche spreading in reach-through photodiodes. *Applied Physics Letters*, 62(6):606, 1993.
- [28] Gregorio Roper Yearwood. Development of a high resolution tracking detector with sipm readout. Diploma thesis, I. Physikalisches Institut B, RWTH Aachen, 2007.
- [29] HAMAMATSU. Mppc multi-pixel photon counter. <http://www.hamamatsu.com>, January 2008.
- [30] SensL. Spmmicro series high gain apd. <http://sensl.com>, January 2009.
- [31] H. Oide, H. Otono, S. Yamashita, T. Yoshioka, and H. Hano and T. Suehiro. Study of afterpulsing of mppc with waveform analysis. In *International Workshop on new Photon-Detectors*, 2007.
- [32] H. Oide, T. Murase, H. Otono, and S. Yamashita. Studies on multiplication effect of noises of PPDs, and a proposal of a new structure to improve the performance. *Arxiv preprint arXiv:0811.1402*, 2008.
- [33] H. Otono, S. Yamashitab, T. Yoshiokab, H. Oidea, T. Suehiroa, and H. Hanob. Study of MPPC at liquid nitrogen temperature. In *International Workshop on new Photon-Detectors*, 2007.

- [34] Willem Johannes Kindt. *Geiger Mode Avalanche Photodiode Arrays*. PhD thesis, Technical University Delft, 1999.
- [35] WJ Kindt and HW Van Zeijl. Modelling and fabrication of Geiger mode avalanche photodiodes. *IEEE Transactions on Nuclear Science*, 45(3):715–719, 1998.

Danksagungen

Ich möchte mich bei allen Personen bedanken die mich bei dieser Arbeit unterstützt haben. An erster Stelle möchte ich mich bei Herrn Prof. Dr. Hans-Christian Schultz-Coulon für das Ermöglichen dieser Diplomarbeit und die gute Betreuung bedanken. Herrn Prof. Dr. Norbert Herrmann danke ich für die Bereitschaft diese Arbeit als Zweitgutachter zu lesen.

Weiterhin gilt mein Dank Alexander Tadday für die gute Betreuung, Hilfe, Zusammenarbeit und Unterstützung während der Diplomarbeit. Rainer Stamen möchte ich für die guten Ratschläge und das geduldige Korrekturlesen dieser Arbeit danken. Des Weiteren möchte ich bei den restlichen Mitgliedern der ILC Forschungsgruppe: Tobias Harion, Alexander Kaplan und Wei Shen für die gute Zusammenarbeit bedanken. Der gesamten ATLAS und H1 Gruppe am KIP: Gabriel Anders, Victor Andrei, Thorsten Dietzsch, Michael Henke (danke fürs Korrekturlesen), Geertje Heuermann, Dr. Ulrich Husemann, Valerie Lang, Dr. Victor Lendermann, Felix Müller, Sahill Poddar, Dr. Felix Rühr (danke fürs Korrekturlesen), Veit Scharf, Paul Seidler, Dr. Pavel Weber, Eva Hennekemper, Michael Herbst, Dr. Andreas Jung und Klaus Urban danke ich für die gute Stimmung und tolle Zeit.

Ein besonderer Dank geht an meine Familie die mir das Studium erst ermöglicht haben und meine Freunde die mich während der Zeit begleitet haben.

Erklärung:

Ich versichere, dass ich diese Arbeit selbständig verfasst und keine anderen als die angegebenen Quellen und Hilfsmittel benutzt habe.

Heidelberg, den 15.01.2010

.....

(Unterschrift)